

TUNNELING DYNAMICS OF A BOSE-EINSTEIN CONDENSATE

by

Shreyas Potnis

A thesis submitted in conformity with the requirements
for the degree of Doctor of Philosophy
Graduate Department of Physics
University of Toronto

Abstract

Tunneling Dynamics of a Bose-Einstein Condensate

Shreyas Potnis

Doctor of Philosophy

Graduate Department of Physics

University of Toronto

2016

The simplicity and versatility of ultra-cold atoms make it an ideal system for studying Quantum Mechanical phenomenon like tunneling. This thesis describes progress towards experimentally measuring the time spent by a tunneling particle in the classically forbidden region. A detailed analysis of the experimental requirements to measure the tunneling time is presented along with the experimental tools developed to meet these requirements. These include a thin $1.3\text{ }\mu\text{m}$ optical tunnel barrier, a smooth atomic waveguide, and a Larmor clock to measure the tunneling time. Delta-kick cooling is used to achieve the extremely low temperatures required for the tunneling time experiments. A $2.4\times$ reduction in the atomic velocity spread is demonstrated, reducing the rms velocity spread to $0.46(5)\text{ mm/s}$. This corresponds to cooling to an effective temperature of $2.0(4)\text{ nK}$.

The thin optical barrier opens up the possibility to study the decay of quasi-bound condensates via tunneling. We develop a novel trapping configuration for this purpose, in which the barrier acts as one of the walls of the trap. Inter-atomic interactions strongly dictate the escape dynamics of the condensate out of this trap, giving rise to three distinct regimes— classical over the barrier spilling, quantum tunneling driven by interactions, and decay dominated by background losses. We show that in the tunneling regime, the decay rate depends exponentially with the chemical potential of the condensate. Experimental results show good agreement with numerical solutions of the 3D Gross-Pitaevskii equation.

Acknowledgements

“Science is really, really hard,” claims the tongue-in-cheek article from the Onion that is posted on the door of the BEC lab. This statement is perhaps a weak form of the more general theorem: *Science is really, really hard when surrounded by brilliant people. Otherwise, it is impossible.* During my graduate years, I have been fortunate to work with very talented and dedicated colleagues, from whom I have learnt a great deal.

I am forever indebted to my thesis supervisor Aephraim Steinberg for his constant support, tutelage, and for showing me how quantum mechanics can simultaneously be extremely simple and mindbendingly confusing (whether it is in a superposition or a mixture of the two, I don’t know).

A huge thanks to the current and past *locos* of the BEC gang: Rockson Chang, Ramon Ramos, David Spierings, Julian Schmidt, Anthony Ardizzi and Sepehr Ebadi. Building, breaking and debugging things together with you guys has been a lot of fun. Rockson patiently taught me everything about the experiment, from fiber coupling to optimizing the BEC ramp. His strong work ethic is something I have always admired and strived to emulate. Ramon has been an amazing lab partner and a friend, always pushing me to overcome my laziness. Without his help on the data runs and tedious alignment procedures, and his constant companionship, this thesis would not have happened. Matin Hallaji, in addition to being a great person to discuss physics, puzzles, and life with, has cheered me up even on the most frustrating days with his endless humour. *Isn’t it? Isn’t it though? Random.* The rest of the group: Xingxing, Amir, Dylan, Lee, Greg, Hugo, Edwin, Josiah. Thank you for all the help, good times, long lunches, and discussions about physics, technology, video games and everything else.

Alan Stummer, with his intimate knowledge of electronics, has saved the day countless number of times. I owe much of my electronics knowledge to him, but I still do not know how to add that one capacitor that makes it all work.

My flatmates Gokul, Vijay, and Luis, thank you for taking good care of me, feeding me great food, and patiently listening to my rants. Gala, Tanuj, Mayank, and all the Andas, thank you for the exciting road trips and the *mini* and *mahasammelans*.

I would like to thank my parents, Kalpana and Mohan Potnis, and my sister Megha, for their love and support. I spent most of my middle school and high school making music visualizations, which is the the coolest possible way to learn math. If not for my parents encouragement to pursue this obscure hobby, I would not be doing science today. Finally, I would like to thank Gandhari for being so awesome, for her love, patience, and for always being there when I needed her.

Preface

This thesis describes experimental and theoretical work done in the BEC lab in Prof. Aephraim Steinberg's research group. A number of people were involved in the projects described in this thesis and I would like to acknowledge their contributions. A large part of the setup was built by my predecessors Ana Jofre, Mirco Siercke, Chris Ellenor and Rockson Chang. The hybrid trap, which is the starting point of all BEC experiments, was built by Rockson. Ramon Ramos has been my lab partner for four out of the five years that I have worked on the experiment and shares credit for most of the work done in the lab. He is responsible for characterizing the new imaging system and building the modular optics for the upper MOT. David Spierings built and characterized the SLD waveguide. Anthony Ardizzi built the coils for the upper MOT. Sepehr Ebadi is responsible for building the electronics and optics for the Raman beams. The parallel MPI code to numerically solve the 3D GPE equation is based on initial code written by Jamie Woodbury. The work described in Ch. 5 was done in collaboration with Kenji Maeda and Prof. Lincoln D. Carr.

The work described in Ch. 5 will lead to the publication:

- Shreyas Potnis, Ramon Ramos, Kenji Maeda, Lincoln D. Carr, Aephraim M. Steinberg. *Interaction assisted tunneling of a Bose-Einstein condensate out of a quasi-bound trap.* (manuscript under preparation)

In addition, I have also contributed to projects that are not described in this thesis. They resulted in the following publications:

- Rockson Chang, Shreyas Potnis, Christopher W Ellenor, Mirco Siercke, Alex Hayat, and Aephraim M Steinberg. “[Observation of transient momentum-space interference during scattering of a condensate from an optical barrier](#)”. *Phys. Rev. A* 88.5 (Nov. 2013), p. 53634
- Rockson Chang, Shreyas Potnis, Ramon Ramos, Chao Zhuang, Matin Hallaji, Alex Hayat, Federico Duque-Gomez, J.E. Sipe, and Aephraim M Steinberg. “[Observing the Onset of Effective Mass](#)”. *Phys. Rev. Lett.* 112.17 (May 2014), p. 170404
- Alex Hayat et al. “[Enhanced coherence between condensates formed resonantly at different times](#).” *Optics express* 22.25 (Dec. 2014), pp. 30559–70

Contents

1	Introduction	1
2	Theory of Bose-Einstein condensates	4
2.1	Gross-Pitaevskii equation	4
2.1.1	Thomas-Fermi Approximation	5
2.1.2	Healing length	6
3	The BEC Machine	7
3.1	Overview	8
3.2	Vacuum system	8
3.2.1	Gate Valve	9
3.2.2	Rubidium ampoule	10
3.3	Magnetic fields	10
3.3.1	Upper MOT	10
3.3.2	Bias fields	11
3.3.3	Quadrupole Trap	12
3.3.4	Push coil	13
3.3.5	RF fields	13
3.3.6	TOP coils	14
3.4	Near-resonant light	14
3.4.1	Trapping Light	16
3.4.2	Repump Light	16
3.4.3	Polarization Spectroscopy	17
3.4.4	Injection Locking	18
3.4.5	Tapered Amplifier	18
3.4.6	Fiber coupling	19
3.4.7	MOT beam modules	20
3.4.8	Push Beam	20
3.4.9	Optical Pumping	21
3.4.10	Absorption imaging	21
3.5	Optical potentials	27

3.5.1	Hybrid trap and crossed dipole trap beams	27
3.5.2	Superluminescent diode beam	29
3.5.3	Barrier Beam	32
3.6	Raman beams	39
3.7	Control and Data Acquisition	41
3.7.1	Hardware and Timing	41
3.7.2	Migration to python	42
3.7.3	Rampage	43
3.7.4	IP-BEC	45
3.7.5	Photo Diode and Temperature monitors	45
3.8	Ramp to BEC	45
3.8.1	Stage 1: MOT loading	46
3.8.2	Stage 2: Molasses and Optical pumping	46
3.8.3	Stage 3: Quadrupole Magnetic Trap	47
3.8.4	Stage 4: Hybrid Trap	47
3.8.5	Stage 4: Crossed Dipole Trap	50
3.8.6	Stage 4: SLD Trap	50
3.8.7	Stage 4: ReST Trap	50
3.9	Outlook	50
4	Progress Towards Measuring the Tunneling Time	52
4.1	Introduction and Motivation	52
4.2	Experimental considerations	56
4.2.1	Barrier width	57
4.2.2	Longitudinal velocity spread	58
4.2.3	Transverse size	60
4.2.4	Number of atoms	60
4.2.5	Width of the Raman beams	61
4.2.6	Precision of the Larmor clock	61
4.3	Delta-kick cooling	63
4.4	First generation Larmor clock	67
4.4.1	Magnetic Field Noise	68
4.4.2	Quadratic Zeeman shift	72
4.4.3	Larmor clock calibration	73
4.5	Summary	79
5	Interaction Assisted Tunneling of a BEC Out of a Quasi Bound State	80
5.1	Introduction	80
5.2	Repulsive Sheet Trap (ReST)	82
5.2.1	Trapping Potential	82

5.2.2	Ground state properties	84
5.2.3	Trap depth and effective barrier width	92
5.2.4	Tunneling rate	95
5.3	Experimental procedure	96
5.4	Results	98
5.4.1	Chemical Potential	99
5.4.2	Background decay rate	99
5.4.3	Classical spill	100
5.4.4	Tunneling	101
5.4.5	3D GPE Simulations	104
5.5	Summary and Future Directions	105
6	Summary and Future Directions	106
Appendices		108
A	Replacing the Rubidium ampoule	109
B	Quadratic Zeeman Shift	112
C	Two component BEC	115
Bibliography		117

List of Figures

3.1	Upper MOT coils screwed onto plates which are clamped around the CF flanges viewports.	11
3.2	Quadrupole coil driver schematic and current response	13
3.3	Layout of the optical table for near-resonant light generation.	15
3.4	Polarization spectroscopy signals.	17
3.5	Schematic for the absorption probe beam shaping and the imaging system.	22
3.6	Imaging pixel size calibration.	23
3.7	Focusing the imaging system	24
3.8	Probe polarization and intensity calibration.	26
3.9	Schematic of the optical layout for generating the hybrid trap and the crossed dipole trap beams.	28
3.10	Super Luminescent Diode beam layout.	30
3.11	Demonstrating the dimple effect.	33
3.12	SLD Beam and trap characterization.	34
3.13	Design of the barrier objective in OSLO.	35
3.14	Schematic of the setup for generating the barrier sheet.	36
3.15	Characterizing the focused beam using knife edge scans.	37
3.16	Schematic for generating Raman light.	38
3.17	Schematic of the setup to focus the Raman beams on the atoms.	39
3.18	Raman beam powers.	40
3.19	Synchronizing the clock to the line voltage.	41
3.20	Screen-shot of the GUI used to edit ramps.	44
3.21	Lower MOT imaged on the side camera	46
3.22	Crossing the critical temperature by heating a pure condensate.	48
3.23	Thomas-Fermi radius of a condensate after time of flight as a function of atom number. Solid line is a prediction using the scaling solution.	49
4.1	The Larmor clock thought experiment. A spin 1/2 particle precesses under the influence of a magnetic field confined in the barrier region. The spin of the incident and the tunneled particles is depicted on the Bloch sphere.	53

4.2	Conditional probabilities for ^{87}Rb atoms tunneling through a $2\mu\text{m}$ square barrier. The barrier height is 50 nK and the particles are incident from the left with an energy of 40 nK.	54
4.3	Experimental scheme for measuring the tunneling time.	56
4.4	Transmission probability through a Gaussian barrier.	59
4.5	Longitudinal velocity spread Δv and transverse radius r_t as a function of number of atoms N	60
4.6	Conditional dwell times for ^{87}Rb atoms tunneling through a Gaussian barrier	62
4.7	Illustration of the delta-kick cooling technique	64
4.8	Collimating the wavepacket by adjusting the kick strength	65
4.9	Delta-kick cooling in the magnetic waveguide.	66
4.10	Role of interactions and aberrations in delta-kick cooling.	67
4.11	Slow drifts in the vertical B -field	69
4.12	Slow drifts in the horizontal B -field	70
4.13	Measuring the Zeeman shift using a 1 ms RF pulse.	71
4.14	Long term B field drifts measured by doing RF spectroscopy	72
4.15	Quadratic correction to the Zeeman shift	73
4.16	Observing the quadratic Zeeman shift for low magnetic fields.	74
4.17	Push coil calibration	75
4.18	Measuring spin rotation due to the Raman beams	76
4.19	Intentional modulation of the magnetic field. The population in the $m_F = 1$ state when the magnetic field is intentionally modulated. Vertical stripes are seen whenever the Zeeman splitting matches the two photon resonance.	77
4.20	Rotation angle θ vs. incident velocity v . Dotted line is a fit to the function $\theta = k/v$, with $k = 2.80 \pm 0.05 \text{ rad}/(\text{mm/s})$	78
5.1	Trap geometry for studying tunneling out of a quasi-bound state.	83
5.2	Measurement of trap parameters of the ReST trap	84
5.3	Potential energy as a function of the vertical position y in the ReST trap at $x = z = 0$	85
5.4	TOF images of atoms released from the ReST trap.	90
5.5	Corrections to the simple hard-wall model.	91
5.6	Estimating the chemical potential in the ReST trap.	93
5.7	Trap depth V_{saddle} and effective barrier width w_{saddle} as a function of the barrier height V_0	94
5.8	Barrier height ramp used to study tunneling out of a quasi bound state.	96
5.9	Chemical potential μ of the condensate as a function of the number of atoms N	99
5.10	Natural logarithm of the number of atoms left in the trap as a function of the hold time in the trap for a high barrier height of 460 nK. A fit to a straight line gives a background decay rate of $\Gamma_{\text{bg}} = 0.31(2)\text{s}^{-1}$	100
5.11	Transition from spill to tunneling indicated by the kink at $\sim 30\text{ ms}$	100

5.12 Escape dynamics in the weak trapping configuration	102
5.13 Decay rate Γ as a function of the chemical potential μ in the weak trapping configu- ration.	102
5.14 Escape dynamics in the tight trapping configuration	103
5.15 Decay rate Γ as a function of the chemical potential μ in the tight trapping configuration.	103
A.1 Schematic of the Rubidium arm of the vacuum chamber and the nitrogen tank setup used while replacing the Rubidium ampoule.	110

Chapter 1

Introduction

The theory of quantum mechanics was developed over a fairly short period in time in the 1920s. Since then, a number of striking and counterintuitive phenomenon arising due to quantum mechanics have been predicted and observed. The physical systems where such phenomenon occurred, were, for the most part, available naturally in our universe. The observation of Bose-Einstein condensation in dilute gases in 1995[4, 5] has ushered in an era where a quantum system can instead be artificially assembled from simple ingredients, and then studied.

Such a system can simply be a coherent matter wave. A wealth of single particle phenomenon arising due to wave mechanics, for example Bloch oscillations[6], Landau-Zener tunneling[7] and Anderson localization[8], have been observed in ultra-cold gases. Interactions between particles adds an extra dimension of complexity and richness, and the ability to experimentally control the interactions makes ultra-cold atoms and molecules a very flexible system to study many-body physics and phase transitions[9]. The observation of the superfluid to Mott insulator transition for bosons[10], the fermionic Mott insulator[11] and the BEC-BCS crossover in fermions[12] are some examples where interactions play a key role in the physics. Advances in the field of dipolar BECs[13] and polar molecules[14] show promise for exciting new physics arising due to strong long range interactions between particles, for example the recent observation of crystallization in a superfluid[15]. Apart from interactions, experimental tricks, like dressing the atom with Raman light fields, can cause neutral atoms to mimic the motion of charged particles in an electric or magnetic field[16, 17]. The development of such a wide variety of tools makes ultra-cold atoms one of the most versatile systems to study quantum phenomenon. The high degree of controllability and flexibility can be used to emulate other quantum systems, realizing Feynman's idea of using Quantum Mechanical computers to simulate physics[18].

The versatility of ultra-cold atoms is partly due to the simplicity of the system, and partly due the favorable length and time scales, made possible due to the cooling and trapping techniques developed in the past three decades. A room temperature gas of atoms in a vacuum chamber can be trapped and laser cooled to μK temperatures within milli-seconds. In a few seconds, about a few billion laser-cooled atoms can be collected and cooled further using evaporative cooling techniques. By selectively picking the hottest atoms and throwing them out of the trap, the entire sample can

be cooled and made denser, at the cost of reducing the number of atoms. This process takes 15-20s, and at the end we are left with 100k-500k atoms, at a temperature of tens of nK and a density of 10^{14}cm^{-3} . At such low temperatures, thermal effects are negligible and Quantum Mechanics dictates the properties of the gas. A gas of bosons undergoes a quantum phase transition at a critical temperature T_c , below which a large fraction of the atoms occupy the ground state of the system. This state of matter is called a Bose-Einstein Condensate (BEC). Such a quantum gas is very fragile, and any disturbance to the system heats it up and decoheres it. Hence, ultra-cold gases are trapped in a vacuum with a lifetime usually greater than one minute, in which they interact only with intended probes (and blackbody radiation). An atomic BEC typically has a size of tens of μm and is trapped in a potential with trapping frequencies ranging from a few Hz to hundreds of Hz. This means that the dynamics of a BEC can be observed using a standard microscope and a CCD camera. The motion of a BEC can be manipulated using focused light beams which are a few microns in size (limited by the wavelength of light used), allowing for almost arbitrary potentials[19]. Such favorable properties of ultra-cold systems, namely, extremely low temperatures, micron size length scales and the ability to create flexible trap geometries, make it an ideal system to study quantum tunneling of particles.

In this thesis I will describe two experiments that explore tunneling properties of a BEC. The first experiment aims to measure the time a particle spends in the forbidden region as it tunnels through a barrier. Tunneling times have been controversial since the early days of Quantum Mechanics[20]. A host of definitions for the tunneling time exist, predicting a time that is independent of the barrier thickness, to superluminal times, to no time at all. While there have been attempts to reconcile these definitions, such attempts have led to more surprising predictions. For example, thought experiments that measure where inside the tunneling region a particle spends time in, find that the tunneled particles spend negligible time in the center of the barrier, essentially hopping from the entrance of the barrier to the exit[21]. The micron size de Broglie wavelength of BECs make it an ideal system to test out some of these predictions. However, there are several challenging experimental requirements that need to be met before the tunneling time can be measured. A detailed analysis of these requirements, along with experimental efforts to meet these requirements are presented in this thesis.

The second experiment explores the role of inter-atomic interactions in the tunneling of a BEC out of a quasi bound trap. A novel trap geometry with the tunnel barrier as one of the trap walls was developed to study this. We find the ground state properties of a condensate in this trap to be in excellent agreement with theory. The tunneling rate of the condensate is strongly dependent on interaction energy, and we find that it goes exponentially with the chemical potential of the condensate. The tunneling results show good agreement with 3D GPE simulations.

Outline

- Chapter 2 introduces some of the basic theory of Bose-Einstein condensates in harmonic traps.

- Chapter 3 describes the Bose-Einstein condensation apparatus, with an emphasis on new additions to the setup. These include a thin $1.3 \mu\text{m}$ optical tunnel barrier, a Larmor clock based on off-resonant Raman beams, and a smooth one dimensional waveguide generated using broadband light. On the software side, a new ramp generation software was developed in python, which greatly simplified programming voltage ramps.
- Chapter 4 describes in detail the experimental requirements for the tunneling time experiments. Efforts to reduce the velocity spread of the incident wavepacket using Delta-kick cooling are described. Finally, a proof-of-principle experiment to measure the dwell time using the Larmor clock is presented.
- Chapter 5 describes the results of the interaction assisted tunneling experiment. A novel Repulsive Sheet Trap is described, and the dynamics of a condensate escaping out of this trap is presented.
- Chapter 6 provides a summary and presents possible future research directions.

Chapter 2

Theory of Bose-Einstein condensates

This chapter reviews the basics of the theory of zero temperature Bose-Einstein condensates, covering only aspects that are directly relevant to the experiment. A detailed review may be found in Refs.[22, 23].

2.1 Gross-Pitaevskii equation

The ground state of a system of N bosons can be found out by assuming that the many body wavefunction Ψ can be written as a direct product of the same single particle (normalized to 1) state ϕ ,

$$\Psi(\mathbf{r}_1, \mathbf{r}_2, \dots, \mathbf{r}_n) = \prod_{i=1}^n \phi(\mathbf{r}_i). \quad (2.1)$$

For non-interacting atoms, ϕ would simply be the ground state of the potential in which the atoms are trapped (Gaussian for a harmonic potential). However, interactions between atoms play an important role in the ground state properties of alkali condensates. For alkali atoms at very low temperatures, the interactions between atoms is characterized by a single quantity: the s-wave scattering length a_s . The complex van der Waals potential can be reduced to an effective contact potential of the form $g\delta^{(3)}(\mathbf{r}_1 - \mathbf{r}_2)$, where $g = 4\pi\hbar^2 a_s / m$. Introducing the order parameter $\psi = \sqrt{N}\phi$, so that $|\psi|^2 = n$ is the density of the condensate and $\int dV |\psi|^2 = N$ is the total atom number, the total energy of the N -particle state is given by the energy functional E ,

$$E[\psi] = \int dV \left\{ \frac{\hbar^2}{2m} |\nabla\psi|^2 + V(\mathbf{r}) |\psi|^2 + \frac{g}{2} |\psi|^4 \right\}. \quad (2.2)$$

Here, V is the external trapping potential. The Gross-Pitaevskii Equation (GPE), which is the dynamical equation for ψ , can be obtained using a variational procedure, $i\hbar \frac{\partial \psi}{\partial t} = \frac{\delta E}{\delta \psi^*}$, giving us,

$$i\hbar \frac{\partial \psi}{\partial t} = \left(-\frac{\hbar^2 \nabla^2}{2m} + V(\mathbf{r}) + g |\psi|^2 \right) \psi. \quad (2.3)$$

The GPE equation is very similar to the Schrödinger equation, but includes the effect of interactions as a mean-field potential $g |\psi|^2$.

2.1.1 Thomas-Fermi Approximation

Eq. 2.3 is non-linear in ψ and very few analytic solutions to this equation exist. However, for trapped alkali gases, often an excellent approximation is to ignore the kinetic energy term to find the ground state. Consider the ground state to have a characteristic size l . The kinetic energy term in Eq. 2.3 will be of the order of $\hbar^2/2ml^2$, whereas the mean field term, which is proportional to the density $n = N/l^3$, is of the order gN/l^3 . Hence, the ratio of the mean-field energy to the kinetic energy is $(gN/l^3) / (\hbar^2/2ml^2) = 8\pi(Na_s/l)$. Here, l is the characteristic length scale of the system, which in the case of a harmonic oscillator is the harmonic oscillator length $l_{h.o} = \sqrt{\hbar/m\omega}$. Thus, the kinetic energy term can be ignored as long as $Na_s \gg l_{h.o}$. Except for very weak traps, highly anisotropic traps, or very low atom numbers, this approximation holds. In Ch. 5, we will explore situations where this approximation is not valid.

Since the ground state is an eigenstate of Eq. 2.3, the only time dependence would be a global phase evolution. Plugging in $\psi(\mathbf{r}, t) = \psi(\mathbf{r}) e^{-i\mu t/\hbar}$ in Eq. 2.3 and ignoring the kinetic energy term, we get

$$\mu\psi(\mathbf{r}) = (V(\mathbf{r}) + g|\psi(\mathbf{r})|^2)\psi(\mathbf{r}). \quad (2.4)$$

Since $|\psi|^2$ cannot be negative, the solution of Eq. 2.4 is

$$|\psi_{TF}|^2 = \begin{cases} (\mu - V)/g & \text{for } \mu - V > 0 \\ 0 & \text{otherwise} \end{cases}, \quad (2.5)$$

Using the normalization condition $\int dV |\psi|^2 = N$, we can find the relationship between N and the chemical potential μ . The fact that μ is the chemical potential can be verified by taking the derivative of E with respect to N in Eq. 5.8. For a harmonic trap with trapping frequencies $\omega_x, \omega_y, \omega_z$, μ is given by [24, 25]

$$\mu = \frac{1}{2}\hbar\bar{\omega} \left(15Na \sqrt{\frac{m\bar{\omega}}{\hbar}} \right)^{2/5}, \quad (2.6)$$

where $\bar{\omega} = (\omega_x \omega_y \omega_z)^{1/3}$. The Thomas-Fermi radii $r_{x,y,z}$ are given by given by

$$r_i = \sqrt{\frac{2\mu}{m\omega_i^2}}. \quad (2.7)$$

An important experimental quantity is the interaction energy per particle. As the condensate is released from the trap, this energy is converted into kinetic energy, as interactions drive the expansion

of the condensate. It is given by

$$\epsilon_{\text{int}}/N = \frac{1}{2} \int \frac{g}{N} |\psi|^4 dV = \frac{2}{7} \mu. \quad (2.8)$$

This is valid for a 3D harmonic trap. In Ch. 5, we will see how the trap shape changes this relation.

Eq. 2.5 shows that in the Thomas-Fermi limit, the condensed cloud takes the shape of the trapping potential. In the case of a harmonic trap, it is an inverted parabola. Conveniently, it can be shown that when the cloud is released from the trap and undergoes free expansion, the shape of the cloud is preserved, and the expanded cloud is just a scaled version of the original cloud: $r_i(t) = \lambda_i(t) r_i(0)$ [25]. The scaling coefficients $\lambda(t)$ satisfy the coupled second order differential equation

$$\ddot{\lambda}_j = \frac{\omega_j(0)^2}{\lambda_j \lambda_1 \lambda_2 \lambda_3} - \omega_j^2(t) \lambda_j. \quad (2.9)$$

In the general case, these equations do not have an analytical solution and one has to resort to numerically solving the differential equation. Approximate solutions exist for cases where the trap is highly anisotropic ($\omega_z \ll \omega_x, \omega_y$). In Sec. 3.8.4, we will compare the size of the condensate after time of flight with solutions of Eq. 2.9. The trap from which the BEC is released has a different trapping frequency in all three directions. Hence, $\lambda(t)$ is calculated numerically.

2.1.2 Healing length

In the previous section we saw that the mean-field energy term is much larger than the kinetic energy term. While this is true for the entire condensate, within the condensate this approximation breaks down near the walls of the trap. Consider a condensate trapped in a trap with a sharp wall. At the boundary, the density of the wavefunction ψ has to vanish. Near this point, the energy of the condensate is purely kinetic, since $g |\psi|^2 \sim 0$. As we move away from boundary towards the bulk, the condensate density builds up to its bulk value over a length scale ξ , called the healing length. The healing length can be calculated by equating the kinetic energy cost $\hbar^2/2m\xi^2$ of changing the wavefunction from its bulk value to 0 over a length ξ to the mean-field energy at the bulk $g |\psi|^2 = gn$. This gives us

$$\xi = \sqrt{\frac{\hbar^2}{2mgn}} = (8\pi a_s n)^{-1/2} \quad (2.10)$$

Note that the density n here is not the peak density, but rather the local density near the wall of the trap.

Chapter 3

The BEC Machine

In this chapter I will describe the Bose-Einstein condensation apparatus and its evolution over the course of my graduate career. To avoid repetition, only the aspects of the setup which are new or have been significantly modified are presented in detail. References to previous students' theses are provided for the rest.

A Bose-Einstein condensation machine is constantly evolving to suit the needs of the experiment being performed. Even as I write this thesis, some of the electronics are being moved to a separate rack to reduce magnetic field noise. Hence, the description of the setup given in this chapter is bound to become outdated soon. Nevertheless, I hope that some aspects of this chapter will be useful to future students for debugging the experiment.

As a fifth generation graduate student, I was fortunate to inherit a reliable BEC apparatus, built and improved upon by my predecessors. Ana Jofre started the project and constructed the vacuum chamber and the initial laser systems[26]. Micro Siercke, along with Chris Ellenor achieved Bose-Einstein condensation in the Time Orbiting Potential (TOP) trap in 2005[27]. Subsequently, Chris Ellenor and Rockson Chang have made many improvements to increase the reliability and stability of the apparatus[28, 29]. For example, the MOT light was fiber coupled and delivered to the vacuum chamber via beam shaping modules which were mounted very close to the chamber. This dramatically increased the alignment stability of the MOT beams. In 2012, we switched to the hybrid trap, which is simpler, more robust and produces bigger condensates as compared to the TOP trap[29]. The new ramp virtually guaranteed a BEC as long as the MOT loaded to a large atom number.

Nevertheless, day to day drifts in fiber coupling were still an issue, especially for the optical pumping beam which had a long optical path. This was especially frustrating during the Fall and Spring seasons, when the lab temperature fluctuated by more than 5 °C. To remedy this, in early 2014 we decided to rebuild the light generation side of the optical table with the aim of minimizing the path traveled by the laser beams before fiber coupling. The entire setup was compacted to two-thirds of its original size, making room for the Raman beam setup which was added later on. Slow drifts in beam alignment were reduced by minimizing the number of mirrors, and by using good quality mirror mounts at critical points.

The output of the tapered amplifier was carefully mode matched to the optical fiber to get a fiber coupling efficiency of 55-60%. This increased the power available to the upper MOT from 100 mW to 230 mW. When it comes to MOT loading, laser power is king. The higher power dramatically increased the available atom flux to the lower chamber and the experiment is now a lot more forgiving to drifts in alignment. The increased atom flux also means that the lower MOT can be loaded in a shorter time. On a good day, 2 s of MOT loading is enough to get a BEC. We typically load the lower MOT for 6 s.

Another cause of frustration was the day to day alignment tweaks needed for the push beam that produces an atom flux to load the lower MOT. This was fixed by modularizing the upper MOT beams, similar to the lower MOT setup. In addition, a new coil mount was constructed for the upper MOT, which fits securely around the CF flanges. This increased the stability of the upper MOT and the push beam had to be aligned only once in a couple of months instead of daily.

On the software side, we switched from using LabView to Python for experimental control, data acquisition and analysis. The motivation for the switch and the new software setup is described in Sec. 3.7.

3.1 Overview

The entire BEC apparatus, including all the optics and the vacuum chamber is built on one $4' \times 10'$ optical table. The right half of the table, termed the “optics side”, has all the optics for generating near-resonant light (Sec. 3.4), Raman light (Sec. 3.6) and the far-off resonant 405 nm barrier light (Sec. 3.5.3). Light from the optics side of the setup is fiber coupled and sent to the left side, termed the “vacuum side”, which has the vacuum chamber (Sec. 3.2). A black cardboard barrier divides the optical table and prevents stray near-resonant light from reaching the vacuum chamber. Apart from the chamber, the vacuum side has all the beam shaping optics for the various light beams aimed at the atoms and cameras for monitoring the atoms. It also has optics for the 1064 nm dipole trap beam (Sec. 3.8.4) and the Super-Luminescent Diode beam (Sec. 3.5.2). As of August 2015, all the associated electronics and power supplies were kept on racks above and below the optical table. In an effort to reduce the magnetic field noise experienced by the atoms, some of the components are currently being moved to a separate rack away from the main table.

3.2 Vacuum system

A Bose-Einstein condensate is produced by a process known as forced evaporative cooling. The hottest atoms from the sample are thrown out, thereby cooling down the rest of the sample [30]. This is unlike a traditional refrigerator where the sample to be cooled is brought in thermal contact with a cold reservoir. We can evaporatively cool a gas to nano-Kelvin temperatures, even though the chamber in which it is held is at room temperature, as long as the gas is thermally isolated from its surroundings. This evaporative cooling process takes about 15-30 seconds. In this time, any

collision with a room temperature atom will knock the trapped atom out of the trap. This imposes stringent requirements on the pressure inside the chamber. A BEC cannot be produced when the lifetime of the atoms inside the trap is shorter than the time it takes to evaporatively cool them. This makes the vacuum chamber one of the most critical parts of an ultra-cold atoms apparatus, and the cause for many nights of lost sleep.

Our vacuum system consists of two chambers, creatively named the upper chamber and the lower chamber. Briefly, the upper chamber is a stainless steel chamber with 6 windows for the MOT beam, 1 top window for the push beam and 1 side window for viewing the MOT. It is connected to the Rubidium arm via a UHV block valve, which houses a 1g ampoule of Rubidium. The pressure in the upper MOT is $\sim 10^{-8}$ Torr. Atoms from the background vapor are trapped in a magneto-optical trap (MOT). A push beam is used to eject these atoms from the upper MOT and create a cold atomic beam. The atomic beam is directed towards a glass cell in the lower chamber, where they are re-captured in a second MOT.

During my time on the setup, we have fortunately suffered only minor setbacks and never needed to break vacuum. The vacuum system is essentially the same as when I started out. Hence, I will skip further discussions about of vacuum chamber and refer to previous grad students' theses. The schematic for the vacuum system, along with the part numbers of the pumps, vacuum gauges and valves can be found in Rockson Chang's thesis, Sec 3.1 [29]. Details about the installation and baking procedure can be found in Refs. [26]. The modifications done in 2006 are described in Ref.[28]. Below, I will primarily document the mishaps that have occurred since 2010.

3.2.1 Gate Valve

The lower chamber is connected to the upper chamber by a 5" long and 0.5" wide feed-through. The small conductance of the feed-through helps maintain a pressure of $< 10^{-11}$ Torr in the lower chamber. A Kurt J. Lesker SG0063-PCCF pneumatic gate valve seals the lower chamber from the upper chamber and maintains UHV. While the thin feed-through should, in principle, maintain UHV in the lower chamber, it was found that the lifetime of the atoms in the trap is reduced when the gate valve is kept open. We suspect this is due to a direct line of sight between the upper chamber and the atoms. The reduced lifetime was detrimental to the efficiency of evaporation and we had to close the gate valve after loading the lower MOT. This meant that the gate valve had to be cycled once every minute. The repeated cycling eventually led to the failure of the gate valve in 2006 and the UHV had to be broken to replace the gate valve. After 9 years of operation, the "new" gate valve has exceeded its lifetime.

The good news, however, is that since 2014, we have been able to successfully create condensates with the gate valve open. This is likely due to the following two reasons: firstly, the Rubidium arm is currently kept at a lower temperature of 33 °C as opposed to 40 °C previously. This could have lowered the vapor pressure in the upper chamber and reduced the effect of the line of sight. Secondly, our new ramp to condensation is shorter and more robust since we start with a higher number of atoms. Hopefully, not having to cycle the gate valve as frequently will increase its life

and delay the inevitable breakdown. Currently, we open the gate valve a few times a day.

3.2.2 Rubidium ampoule

The Rubidium ampoule, once installed, is expected to get depleted over the course of a few years. However, since I started working in the lab in Sept 2010, we had to replace the ampoule on three occasions: in Feb. 2011, Feb. 2013 and May 2014. From Feb. 2011 to Feb. 2013, the half-nipple containing the Rubidium ampoule was maintained at a temperature of 38-40°C. We suspect that we ran out of Rubidium faster than usual since the temperature was at around or slightly greater than the melting point of Rb, which is 39 °C. Hence, we kept the temperature at around 33 °C after we replaced the ampoule in Feb. 2013. During the 2013 replacement, it was found that the block valve for the nitrogen inlet (see Fig. A.1) was damaged and did not maintain UHV pressure in the main chamber. This is possibly due to over-tightening the block valve when it was closed in 2011. The issue was resolved when the block valve was replaced with a spare we had in the lab.

In April 2014, the controller for the Varian Turbo pump which was pumping the upper chamber shut itself down due to an over-temperature fault. This brought the pressure in the upper chamber to mTorr levels for a period of two days. Once the pump was turned on, it took about 2 weeks for the pressure inside the chamber to reach previous levels. However, there was not enough Rubidium in the chamber to get a MOT, presumably because the cell walls, which were coated with Rubidium previously, now had some other crud. We replaced the ampoule in May 2014 and got a MOT back within a week. The half-nipple is now maintained at 33 °C, so the Rubidium should last at least until May 2016. The procedure for replacing the ampoule is described in Appendix A.

3.3 Magnetic fields

A number of magnetic field coils are used in the experiment to trap and manipulate the atoms. Most of these coils were designed and built before I started working on the experiment. The designs and calibrations for these coils can be found in Refs.[[28](#), [29](#)]. In this section I will only describe the coils that were added and include recent calibration data.

3.3.1 Upper MOT

In May 2014, the upper anti-Helmholtz MOT coils were replaced, since the previous mount was unstable and caused the position of the upper MOT to drift. The design and construction of the new coils was carried out by Anthony Ardizzi. They consist of 192 turns of 10 AWG copper wire. The mounts, made of Delrin, are designed to have an inner diameter of 2.80”, so that it fits snugly around the 2.75” CF flange viewports. The coils are screwed onto plates which are clamped around the CF flanges, so that the coils are securely mounted(see Fig. 3.1). Since the switch to the new coils, the stability of the upper MOT has increased significantly and the upper MOT rarely needs realignment.

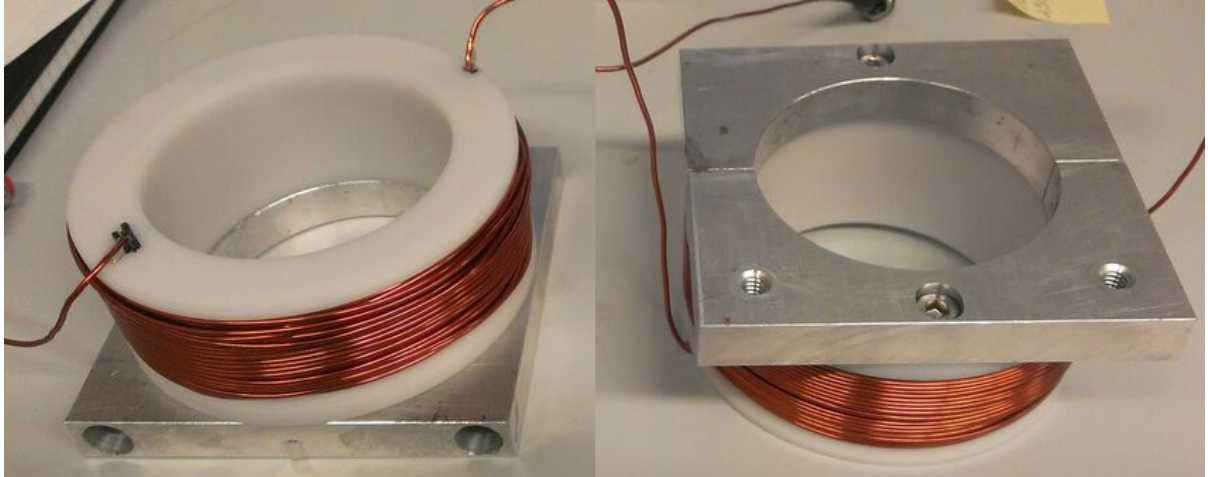


Figure 3.1: Upper MOT coils screwed onto plates which are clamped around the CF flanges viewports.

Coil	Measured Calibration (G/V)	Zero voltage (V)
x(imaging)	0.53	0.3
y(vertical)	4.3	0.16
z(bore)	0.21	-0.4*

Table 3.1: Bias field calibrations. Note that for the z-coil, to zero the magnetic field, one would need to send a negative current, which the current driver is not designed for.

3.3.2 Bias fields

Three orthogonal pairs of coils in Helmholtz configuration are used in the lower chamber to add a constant bias magnetic field. They are used to cancel background magnetic fields, to set the quantization axis during optical pumping and absorption imaging, to shift the center of the quadrupole trap and to apply a constant field for spin manipulation using RF and Raman fields. The coil designs, wire gauges and number of turns can be found in Sec. 3.4 in Ref.[29].

The vertical magnetic field coils (V-Bias) are driven by a Kepco BOP 36 12M current driver. The bipolar driver can switch the direction of the current flow. The two coils are connected in series and a mechanical relay can be switched to bypass the upper coil. This configuration is used to apply a vertical magnetic field gradient during time-of-flight for Stern-Gerlach measurements.

The horizontal x-bias and z-bias coils are driven by home built low power constant current sources capable of driving 4 A and 1 A respectively. These drivers are not bipolar, so the direction of the current cannot be switched by applying a negative voltage.

The magnetic field calibration data, along with the control voltage needed to cancel the background magnetic field can be found in Table 3.1. These calibrations are obtained by measuring the Zeeman splitting of the trapped atoms when a bias field is applied (see Sec. 4.4). The zeroing voltages for the x and y directions are found by applying a bias field along z and measuring the

resonance frequency of the atomic spin. The magnetic field strength is given by

$$|B| = \sqrt{B_z^2 + B_{\perp}^2}. \quad (3.1)$$

where B_{\perp} is the magnetic field perpendicular to z . The field along x and y is then scanned to minimize the resonance frequency and hence minimize B_{\perp} . This is repeated for a smaller bias field along z to increase the sensitivity. Once the field is nulled along x and y , the resonance frequency is measured while B_z is scanned. A fit to a straight line then gives both the calibration for the z coils and the control voltage needed to cancel the background field along z . Similar calibrations are then done for the x and y coils.

3.3.3 Quadrupole Trap

The anti-Helmholtz coils in the lower chamber provide a magnetic field gradient during the MOT stage, the quadrupole trap during the RF evaporation stage, and a vertical magnetic waveguide for the condensed atoms. The magnetic field due to an anti-Helmholtz pair of coils around the B -field zero can be approximated as

$$\mathbf{B} = B'_z \left(\frac{x}{2} \hat{x} + \frac{y}{2} \hat{y} - z \hat{z} \right). \quad (3.2)$$

B'_z is the magnetic field gradient along the z direction. The coils are formed by 64 turns of square cross section hollow core wires[29] and are driven by an Agilent 6682A 21V, 240 A constant current driver. A control voltage sent to the driver is used to modulate the current in the coils during the ramp. To increase the resolution of the output current, the control voltage is divided using a voltage divider with resistances 6.2 kΩ and 1.2 kΩ before sending to the driver. The measured current calibration is 6.0 A/V. The magnetic field gradient calibration is obtained by measuring the acceleration of the atoms in the vertical waveguide (see Fig. 5.2), which gives $B'_z = 23.2$ G/cm/V, or $B'_z = 3.75$ G/cm/A.

The current driver has a slow 100 ms response time, measured as the $1/e$ time of the response of the driver when the control voltage is abruptly changed. The frequency response of the driver is shown in Fig. 3.2(b). This is not suitable for rapidly switching off the trap before time-of-flight, where a response time of 1 ms is desired. To overcome this problem, 4 power FETs are added in parallel, which open the circuit, effectively cutting off the current to the coils[28]. Transient Voltage Suppressors(TVSs) are added in parallel to the coils to dissipate the inductive energy stored in the coils. The measured turn off time using the FETs is 0.5-1.0ms, depending on the initial current.

The direction of current in one of the two quadrupole coils can be switched using mechanical relays so that the coils are in Helmholtz configuration(see Fig. 3.2(a)). The Helmholtz configuration is used to apply moderately high magnetic fields (~ 20 G) when the condensate is optically trapped. At these fields the quadratic Zeeman shift (see Sec. 4.4.2) can be exploited to selectively address two Zeeman sublevels.

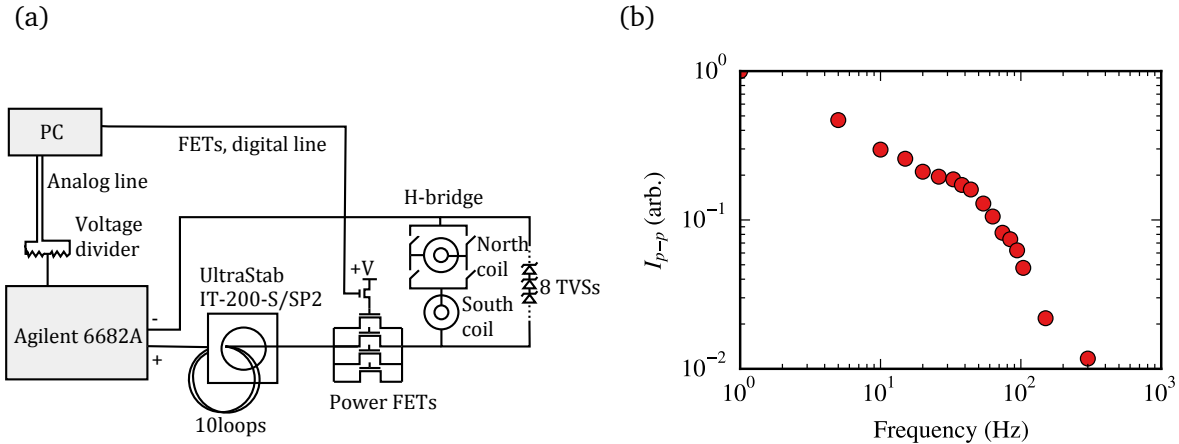


Figure 3.2: (a) Schematic of the setup to drive the quadrupole coils. The H-bridge is formed by four Tyco Electronics V23132-B2002-A100 high current mechanical relays. (b) Frequency response of the Agilent 6682A constant current driver measured by modulating the control voltage at a given frequency and measuring the current using the UltraStab IT-200-S/SP2 current sensor.

3.3.4 Push coil

A single, 45 turn, 27 mm diameter coil was added along the bore axis (z) to apply a strong magnetic field gradient to “push” the condensate. This coil is inserted in the bore of the quadrupole trap coils and is placed 15 mm from the center of the cuvette. It is driven by a home built constant current driver capable of generating up to 50A of current for a short 10 ms duration. The coil calibration, measured by accelerating the condensate in a field gradient, is 21 G/cm/V.

3.3.5 RF fields

RF radiation is used to address the magnetic sub-levels of the ground state which are split in the presence of an external magnetic field. This is used to eject atoms from the quadrupole trap during the evaporative cooling stage and to manipulate the spin of the condensate.

Two single loop antennas (27 AWG wire) are used to shine RF radiation on the atoms. The range of frequencies used is between 0.5-30MHz. The y-coil is wrapped around the cuvette and placed roughly 2 cm from the trap center. The z-coil is inserted in the bore of the quadrupole coil. It has a diameter of 27 mm and is placed 15 mm from the center. Only one of the two coils are used at a given time in the experiment. The RF couples Zeeman states when there is a component of the RF field perpendicular to the DC magnetic field. Thus, depending on the direction of the applied bias field, either the y-coil or the z-coil is chosen.

A Agilent 33250A 80 MHz function generator is used to generate the RF fields. A mini-circuits ZASWA-2-50DR+ switch is used to pulse the RF field and to generate arbitrary pulse sequences for spin manipulation. The RF signal is amplified by a mini circuits ZHL-1-2W(+) amplifier. The function generator is programmed via GPIB and typically runs in two modes. During the evaporation stage, it is operated in frequency modulation mode and an analog voltage controls the frequency of

	OP on, repump on	OP off, repump off	OP off repump on
TOP coil closed (shorted)	2.6B	170M	400M
TOP coil open	1.6B	60M	140M

Table 3.2: Number of atoms loaded in the quadrupole trap for different optical pumping and TOP coil configurations. Before turning on the quadrupole trap, the atoms are optically pumped to the $|F = 2, m_F = 2\rangle$ state. The three columns indicate whether the Optical Pumping (OP) beam and the repump beam were on or off. The two rows correspond to whether the TOP coils were closed (shorted) or open.

the signal. After the condensate is produced, the controller is switched to burst mode or frequency sweep mode to manipulate the condensate spin. This switch is done via GPIB and the function generator takes about 1 s to change the mode. In this time the output of the function generator is undefined and it gives out broadband noise. To prevent the noise from coupling to the atomic spin, the switch is turned off for that duration.

3.3.6 TOP coils

The TOP coils were used to generate fields for the Time Orbiting Potential (TOP)[27], which was the second stage of cooling. Ever since we have switched to the hybrid trap, these coils are no longer used. We have noticed that the presence of these coils affects the quadrupole capture efficiency depending on whether they are shorted or open (see Table 3.2). The loading increases significantly when the TOP trap coils are shorted. This is probably due to mutual inductance between the quadrupole coils and the TOP coils which affects the quadrupole field turn on. Why shorting the coils helps, however, is an unsolved mystery.

3.4 Near-resonant light

Narrow-band light close to the D2 resonance of ^{87}Rb at 780.24 nm is used in the experiment for the Magneto-Optical Trap (MOT), the push beam that generates a cold atomic beam, optical pumping of Rb atoms, and absorption imaging. All near-resonant light is derived from two External Cavity Diode Lasers (ECDLs), which provide narrow-band light. The ECDLs are locked to the Rubidium D2 transitions using Doppler-free polarization spectroscopy [31]. The power and frequency of these lasers beams is controlled using Acousto-Optic Modulators (AOMs). The ECDLs provide tens of mW of power, which is insufficient for the two MOTs. Hence, additional power is obtained by two stages of amplification. In the first stage, the laser light from the ECDLs is used as seed to injection lock two laser diodes. In the second stage, the light from the injection locked diodes is used to seed a Tapered Amplifier (TA).

A schematic of the setup for near-resonant light generation is shown in Fig. 3.3. A few positions along the beam path are labeled as (a), (b), (c) and so on in the figure. These are points where we frequently measure the power of the laser beams while optimizing the setup. Typical powers

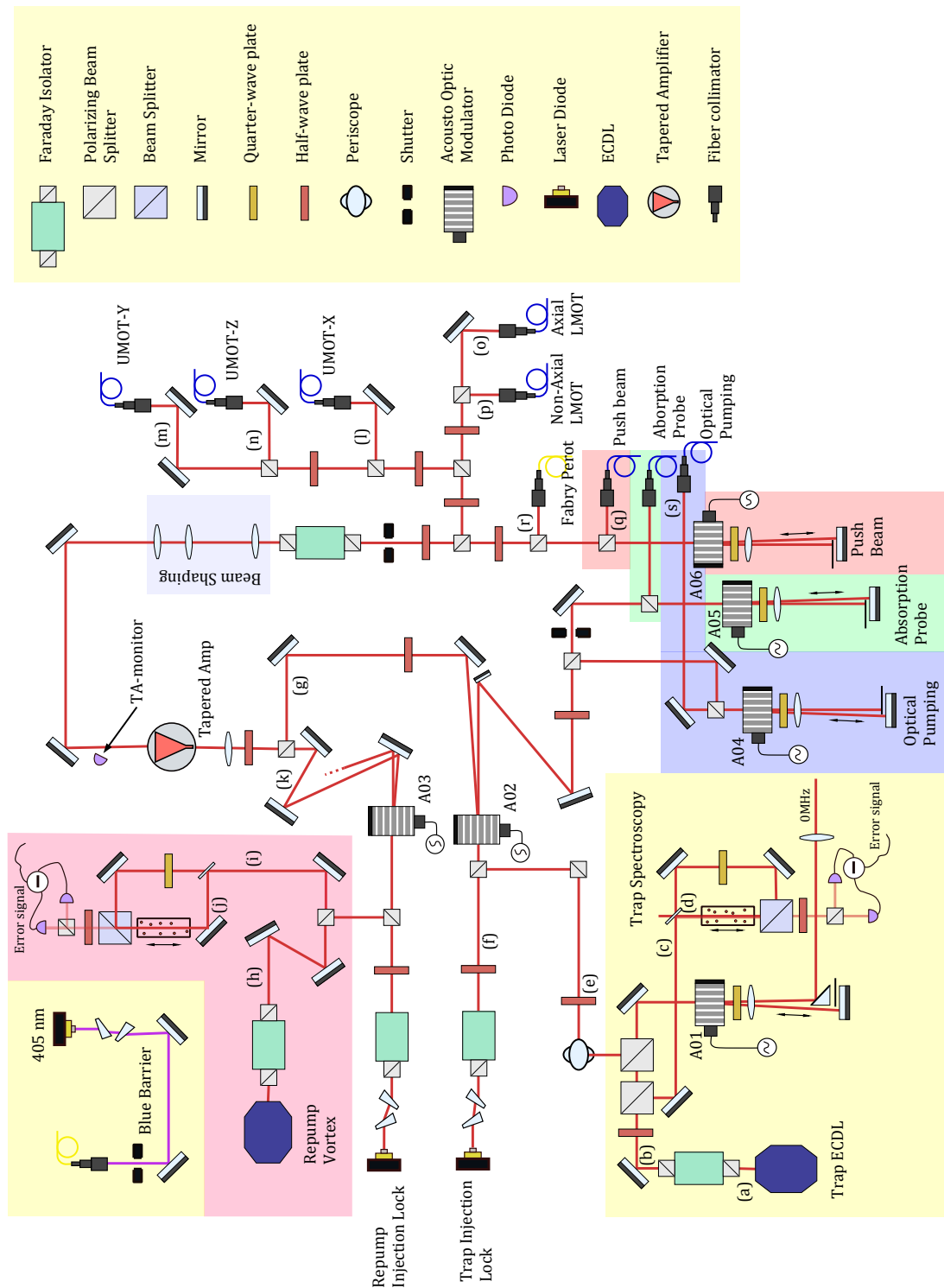


Figure 3.3: Layout of the optical table for near-resonant light generation.

measured at these points are listed in Table 3.4. The various AOMs used in the experiment are also labeled and their operating frequencies can be found in Table 3.3. Finally, the in fiber power in all the optical fibers along with the coupling efficiency is listed in Table 3.5.

3.4.1 Trapping Light

The trapping line begins with a Vortex II TLB-6913 grating stabilized ECDL, which typically gives 45 mW of power with a nominal line-width of less than 300 kHz FWHM. Our line-width measurements using a Fabry-Perot are limited by the 1.5 MHz line-width of the Fabry-Perot. The frequency of the laser is locked to the $F = 2 \rightarrow 3$ cyclic transition using polarization spectroscopy (see Sec. 3.4.3). The schematic for the optical layout is shown in Fig. 3.3.

The MOT and molasses stage require the trapping light to be red-detuned and tunable with a detuning range of $\Delta = -3\Gamma$ to -7Γ , where $\Gamma = 2\pi \times 6$ MHz is the natural line-width of the transition. This detuning range is accessed first by down shifting the light by 110-134 MHz and then up shifting it using a second AOM by 92 MHz. An AOM (AO1 in Fig. 3.3) in double-pass configuration[32] is used for the down shift. The double pass diffraction efficiency is around 30%. The down shifted light is used to injection lock a Sanyo DL-7140-201W free running diode (see Sec. 3.4.4) to get more power. Care is taken to ensure that the alignment of the output of the double-pass AOM does not change with the frequency of the RF driving the AOM. This ensures that the injection lock stays locked as the RF frequency is swept during the molasses stage. The 0th order of AO1 is picked off using a right angle prism mirror and is available to injection lock another diode. Currently, it is not being used for anything. In the past, however, it was used to generate near-resonant Raman coupling light.

AO2 is used to up shift the frequency of the injection locked diode so that it is 18 MHz red-detuned to the cyclic transition. The up-shifted first order of the AOM is sent to the tapered amplifier. The 0th order of AO2 is sent to the optical pumping and absorption probe lines.

3.4.2 Repump Light

Similar to the trapping light, the repump light is generated by locking a New Focus Vortex I 6013 ECDL to the $F = 1 \rightarrow F' = 1 - 2$ crossover. This ECDL is an older 2001 model, and the line-width of the laser when seen on the Fabry-Perot is 3-4 MHz. This could either be due to the age of the diode laser or due to the P-I gain of the locking box not being optimized. Since the line-width of the repump light is not critical to the experiment, this issue was not investigated thoroughly.

The repump light from the ECDL is used to injection lock a free running diode to get more power. AO3 is used to down shift the injection lock light so that it is close to the $F = 1 \rightarrow 1$ resonance. The down shifted light is sent to the tapered amplifier. The 0th order of AO3 is picked off and fiber coupled. It is available either for diagnostics or to injection lock another diode.

The AO3 frequency is adjusted to optimize MOT loading as well as capture in the quadrupole trap after optical pumping. It was found that just the MOT loading rate was not a good indicator

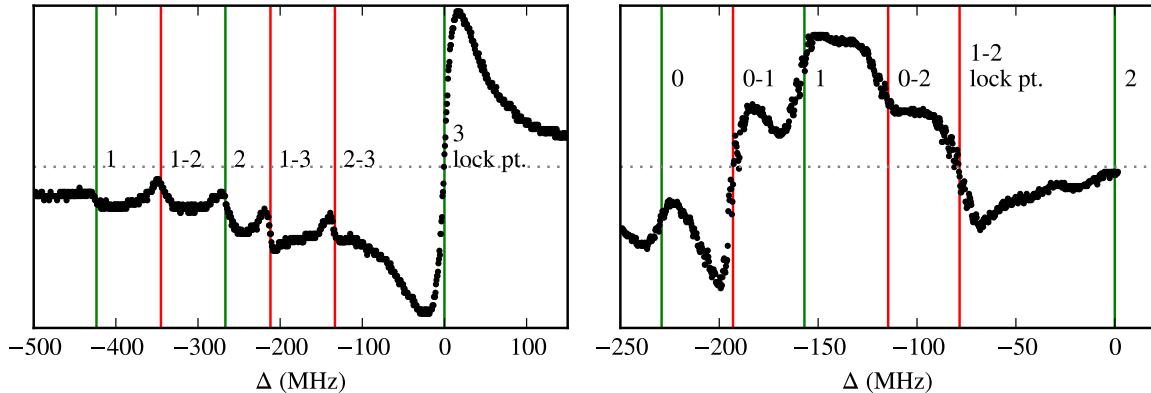


Figure 3.4: Polarization spectroscopy signal for the $F = 2 \rightarrow F'$ transition (left) and the $F = 1 \rightarrow F'$ transitions (right). The expected position of the hyperfine transitions between $F \rightarrow F'$ are marked in green vertical lines, whereas the expected positions of the cross-overs are marked in red.

of the optimum set-point of the repump frequency. During the optical pumping stage, the repump light is kept on and the frequency of the light affects the efficiency of optical pumping.

3.4.3 Polarization Spectroscopy

Polarization spectroscopy is a variant of the standard Doppler-free saturated absorption spectroscopy[31]. In polarization spectroscopy, a circularly polarized pump beam optically pumps the Rubidium atoms and creates a Faraday medium. The linearly polarized probe beam is sent counter-propagating to the pump. Due to the circular birefringence induced in the medium, the plane of polarization of the probe beam gets rotated. This effect is measured as a slight imbalance in the beam powers at the output when the probe beam is sent through a polarizing beam splitter. The angle of rotation is proportional to the real part of the refractive index, which gives the measured signal a dispersive shape , with a zero-crossing at resonance(see Fig. 3.4). The zero-crossing gives a convenient error signal to lock the probe laser to.

In practice, the zero-crossing often has a small offset which is dependent on the probe power. This is undesirable, since a drift in the probe power would result in shift of the zero-crossing, and hence the frequency set-point. This offset could be caused due to a number of reasons. However, we have found that the biggest culprit is magnetic field transverse to the pump and probe propagation direction, originating from nearby optical isolators. The transverse B -field causes an imperfect cancellation of the Doppler broadened Gaussian background, which results in the offset. To reduce the effect of magnetic fields, we place all optical isolators as far away from the Rubidium cell as possible and orient the axis of the cell to be parallel to the nearest optical isolator. Additionally, the Rubidium cell used for the repump spectroscopy is wrapped in two sheets of Mu-metal, which improved the spectroscopy signal slightly.

Fig. 3.4 shows the spectroscopy signals for the trapping and the repump light. The scaling on

the x-axis is obtained by comparing by the distance between two hyperfine levels with the known hyperfine structure of Rubidium[33]. After this calibration, the measured positions of the hyperfine levels is compared with the expected positions. We see that these do not match perfectly. This could be due to a non-linearity in the response of the piezo actuator of the ECDL.

3.4.4 Injection Locking

Injection locking is a technique where a free running laser diode can be forced to lase at a particular frequency if a small amount of seed light is coupled into the diode. The seed light is injected into the laser diode by means of a half optical isolator (see Fig. 3.3). The initial coarse alignment is done by overlapping the seed light with the output of the free running diode by eye. The photodiode built into the free running diode is monitored while alignment. When some of the seed light is coupled into the diode, a rise in the photodiode current is seen. The alignment is further optimized by maximizing the photocurrent. The free running diode locks to the seed light only in a narrow range of current $\Delta I \propto P_{\text{seed}}$, where P_{seed} is the coupled seed power. After the seed light is aligned, the current in the injection lock diode is scanned and the photodiode current is monitored. When the free running diode is locked to the seed, there is a jump in the photodiode current. The seed alignment is again optimized to maximize this jump.

It is desirable to operate the injection locked diodes close to their maximum recommended current, to get a high power output. Depending on the temperature of the diode, the current at which it locks may or may not lie in this required region. In this case it is necessary to change the set point of the temperature controller. A useful rule is that increasing the temperature and the current have the same effect. Thus, to increase the current point where the diode locks, one should decrease the temperature of the diode.

The seed light for the trapping injection lock comes from the output of a double pass AOM. Unless perfectly aligned, the angle of the output beam of the double pass has a small dependence on the AOM frequency. Hence, it is necessary to verify that the injection lock, which is seeded by the AOM output, remains locked as the frequency of the AOM is scanned.

3.4.5 Tapered Amplifier

An Eagleyard EYP-TPA-0780-01000 tapered amplifier, typically driven at 1.9 A is used to amplify the MOT light (see Sec 3.2.2 in Ref. [28] and Sec 3.2 in Ref. [29] for details on the diode mount and the current and temperature controller). Light from the trapping and repump injection diodes is combined at a PBS and is used to seed the tapered amplifier. The tapered amplifier amplifies only one input polarization. Thus, a half-wave plate placed before the tapered amplifier is used to control the ratio of seed power of the trapping and repump light. A photodiode placed close to the output of the tapered amplifier is hooked up to a LabJack and constantly monitored (see Sec. 3.7.5). It picks off some of output light scattered off by the mirrors. The reading on the photodiode is used to align the seed light. Typical values of the photodiode voltage are 1800mV when seeding only with

the trapping light and 1050mV when seeding only with the repump light. While the ratio of the output powers when seeding only with trapping or repump light is ~ 0.6 , the ratio is close to 1/10 when seeded simultaneously by both. This is due to saturation of the gain in the tapered amplifier. The ratio of the trapping and repump powers is measured by sending a portion of the output to a Fabry-Perot.

The output of the tapered amplifier is highly astigmatic, since the waveguide in the chip expands horizontally along the propagation direction. To correct the astigmatism, a 20 cm cylindrical lens is placed ~ 32 cm from the center of the tapered amplifier chip. The beam is then sent through a 1/3 magnification telescope to mode match it with the output of the fibers that it will eventually be coupled into. The telescope comprises of 15 cm and 5 cm doublets with a distance of 11.3 cm between them.

It was found that the far-field intensity pattern of the beam was elliptical with the major axis at a slight angle with the horizontal. To correct this tilt, the axis of the cylindrical lens had to be rotated slightly. The optimum angle is roughly determined by correcting the tilt in the far-field intensity pattern. Ultimately, the figure of merit that matters is the fiber coupling efficiency. It is found that an angle of around 6° maximizes the coupling efficiency. Similarly, the optimal distance between the two lenses is also found by optimizing the fiber coupling efficiency.

After beam shaping, the light is then split 8 ways: 3 paths go into three fibers for the upper MOT, 2 paths go to fibers for the axial and non-axial light for the lower MOT, 1 path is fiber coupled and sent to the Fabry-Perot for diagnostics and the final path goes to a double pass AOM (AO6) for the push beam.

The two mirrors immediately after the tapered amplifier are mounted on Newport ULTIMA mirror mounts, which have better long term stability as compared to the standard Thorlabs mounts used in the experiment. This reduces day to day drifts in the fiber coupling significantly.

3.4.6 Fiber coupling

A number of different solutions are implemented in the setup to mode-match and optimize the coupling efficiency into a single mode fiber. It was found that most of the time, fixed focus fiber collimators did not provide sufficient degrees of freedom to optimize the coupling efficiency. Hence the lower MOT and push beam fibers use Thorlabs variable focus fiber collimators. The distance between the collimating lens and the tip of the fiber can be adjusted by rotating the outer barrel of the collimating package. Optimizing the focus of these collimators is extremely frustrating, as a slight rotation of the barrel completely misaligns the fiber and the alignment process has to be started all over again.

The most convenient solution we have found is to mount the tip of the fiber on a Thorlabs SM1FCA fiber to free space adapter, which is attached to a cage plate. The collimating lens is mounted on a Thorlabs SM1Z translation stage and connected to the cage. This allows smooth adjustment of the distance between the fiber tip and the collimating lens. The upper MOT fibers were coupled this way to get 50-55% fiber coupling efficiency. This coupling efficiency is remarkable,

Label	AOM Name	Frequency(MHz)	Order used	Single or double pass
AO1	Trapping frequency modulation	55-70	-1	double
AO2	Trapping seed	92	+1	single
AO3	Repump seed	74.5	-1	single
AO4	Optical Pumping	63-67	-1	double
AO5	Absorption probe	45-65	+1	double
AO6	Push beam	76	-1	double

Table 3.3: Configuration of Acousto-Optic Modulators (AOMs) used to manipulate near-resonant light on the experiment. The frequency column either gives a fixed frequency that the AOM operates at, or a range of frequencies when the frequency is computer controlled. The positions of the AOMs can be found in the schematic in Fig. 3.3

Trapping line			Repump line		
Label	Location	Power (mW)	Label	Location	Power (mW)
(a)	vortex	46	(h)	after isolator	5.5
(b)	after isolator	33	(i)	spectroscopy total	0.2
(c)	spectroscopy total	0.6	(j)	spectroscopy probe	0.05
(d)	spectroscopy probe	0.1	(k)	into tapered amplifier	7.6
(e)	after double pass	6.6			
(f)	injection lock output	27			
(g)	into tapered amplifier	17			

Table 3.4: Typical optical beam powers in the trapping and repump lines on the experiment. Refer to Fig. 3.3 for positions where the powers are measured.

given that the output of the tapered amplifier is highly astigmatic.

3.4.7 MOT beam modules

MOT light coupled into fibers is sent to beam shaping modules close to the vacuum chamber, as described in Refs.[28, 29]. Similar to the lower MOT modules, three modules, one for each orthogonal pair of beams were added for the upper MOT in 2013. Unlike the lower MOT which has 6 independent beams, the upper MOT light is retro-reflected. The modules are screwed onto plates which are clamped around the CF flange windows of the upper MOT. A 15 cm achromatic lens is to collimate diverging light from a fiber and a polarizer and quarter waveplate is used to control the beam power and polarization. The waist of the collimated light would be ~ 15 mm, if it was not clipped by the 1" diameter optics.

3.4.8 Push Beam

A fraction of the light from the tapered amplifier is sent to a double pass AOM (AO6) and down shifted so that it is 170 MHz red-detuned from the $F = 2 \rightarrow 3$ transition. About 9 mW of push-beam power is available in fiber. The setup for focusing the push beam on the upper MOT is described in Ref. [29]. When the push beam is aligned well, we get a loading rate of roughly 5×10^8 atoms/s in

Label	Location	Power in (mW)	Power out (mW)	% coupled
(l)	Upper MOT-x	165	95	57
(m)	Upper MOT-y	135	68	50
(n)	Upper MOT-z	115	65	56
(o)	LMOT Axial	86	14.5×2	34
(p)	LMOT Non Axial	150	11.5×4	31
(q)	Push beam	17	8.8	51
(r)	Fabry Perot	6.5	N.A	N.A
(s)	Optical Pumping	7.5	5.2	70

Table 3.5: Fiber coupling efficiencies for the MOT, absorption probe, optical pumping and push beam fibers. Refer to Fig. 3.3 for positions where the powers are measured. The coupling efficiency for the LMOT Axial and Non Axial fibers includes a 50% hit taken at the fiber beam splitters.

the lower MOT.

3.4.9 Optical Pumping

σ^+ polarized light resonant on the $F = 2 \rightarrow 2$ transition is used to optically pump the atoms to the $|F = 2, m_F = 2\rangle$ ground state after the molasses stage. The $|F = 2, m_F = 2\rangle$ is a weak field seeking state and can be trapped magnetically. The optical pumping beam is derived from the 0th order of AO2 (see Fig. 3.3). Since the trapping light and the optical pumping light are not used at the same time, AO2 is switched off after the molasses stage, redirecting all the power to the optical pumping line. This light is down shifted by a double pass AOM (AO4) so that the frequency is close to the $F = 2 \rightarrow 2$ transition. The AOM output is fiber coupled into a PM fiber and sent to the vacuum side of the setup. A schematic for the cage module for beam shaping the optical pumping beam can be found in Sec 3.2 in Ref. [29].

3.4.10 Absorption imaging

Absorption imaging is the primary means of obtaining information about the cloud of atoms in our experiment. A resonant or slightly detuned Gaussian beam is flashed on for a short duration on the atoms. Depending on the size, shape and density of the cloud, parts of the beam are absorbed. The resulting absorption profile is imaged on a 12 bit DALSA CA-D1 CCD camera with a sensor with 256×256 pixels and a pixel size of $16\mu\text{m}$. A National Instruments PCI-1424 frame grabber is used to acquire the images on a PC.

The setup for the absorption probe and the imaging system are shown in Fig. 3.5. The probe beam propagates along the horizontal x direction. In the zoomed in configuration used to image the condensate, the field of view is $750 \times 750\mu\text{m}$. This poses a slight problem when imaging the cloud after a long time of flight, since the cloud goes out of the imaging window and the imaging system has to be realigned. To make re-aligning the imaging system easy and repeatable, the probe beam, the imaging system and the camera are mounted on translation stages. We typically operate in two configurations: in-situ and after 20 ms of time of flight. For the 20 ms configuration, the imaging

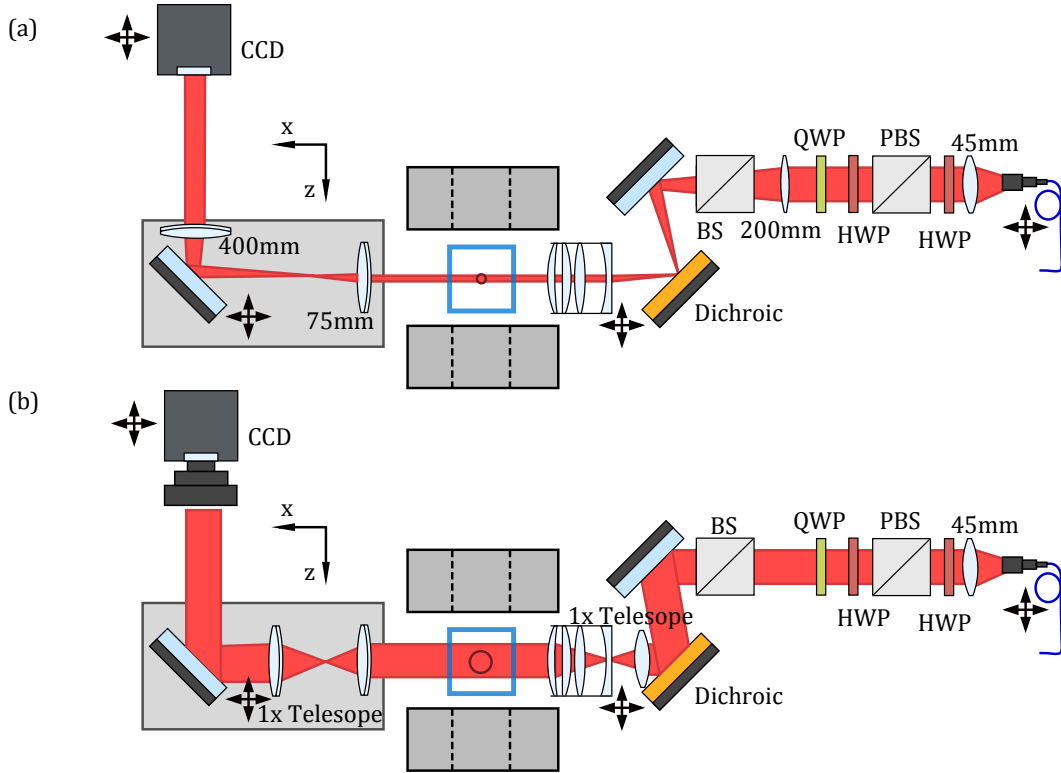


Figure 3.5: Schematic for the probe beam shaping and the imaging system. Light from a PM fiber is collimated using a 45 mm lens to get a 6 mm beam waist. A PBS is used to set the initial polarization to horizontal. A half-wave plate and a quarter wave plate are used to set the probe polarization to σ^+ . The half-wave plate is used to compensate any polarization dependent phase shifts introduced by the mirrors. (a) In the zoomed in configuration, the 200 mm lens and the 45 mm barrier objective together form a telescope which reduces the beam waist to 1.2 mm. The imaging system comprises of two achromats which provide a magnification of 5.3. They are mounted together on a cage system which is on a 3-axis translation stage, which allows for easy alignment. The CCD camera is also mounted on a 3-axis translation stage. (b) The zoomed out configuration is used to image large clouds. In this configuration, the 200 mm lens is removed and instead a 45 mm achromat is magnetically clipped on to the barrier objective. Similarly, the 400 mm imaging achromat is unscrewed from the cage mount and instead replaced with a 75 mm achromat which is magnetically clipped on to the cage. The two 75 mm lenses transport the image closer to the camera and a camera lens is used to image the cloud. The magnification in the zoomed-out configuration is 0.32.

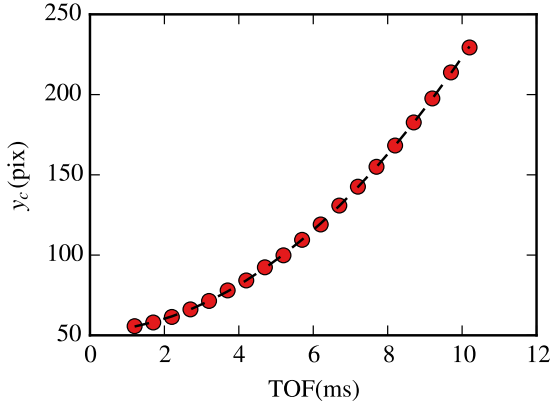


Figure 3.6: Pixel size calibration. The pixel size and hence the magnification of the system is found by tracking the center of a freely falling cloud. For the zoomed in configuration, the pixel size is $3.00(2)\text{ }\mu\text{m}$. The measured magnification of 5.33 is the same as the theoretical magnification of $400/75 = 5.33\dots$ within error bars. The data shown is for a condensate prepared in the $m_F = 2$ Zeeman sublevel. Systematic error due to residual magnetic field gradient is $0.004\text{ }\mu\text{m}$. This is determined by measuring the magnetic field gradient by dropping a condensates prepared in $m_F = 2$ and $m_F = -2$ and measuring their position differences after time of flight. The residual magnetic field gradient is $20 \pm 7\text{ mG/cm}$.

system and the camera have to be moved 2 mm down. The probe beam fiber has to be moved 9 mm upwards, since it goes through a telescope with a magnification of -4.4.

The pixel size and hence the magnification of the imaging system is determined by tracking the center of a freely falling cloud (see Fig. 3.6). The imaging system is focused by imaging a small cloud and scanning the position of the 75 mm achromat to minimize the width of the imaged cloud (see Fig. 3.7). For small clouds, lensing effects are seen when imaged using an off-resonance probe beam. The real part of the refractive index bends some of the incident light. If all of this light is not collected by the imaging system, or if the imaging system is off-focus, the image of the cloud develops either a halo around the cloud or a hole in the center (see Fig. 3.7). This depends both on the sign of the detuning and on the which side of the focal plane the cloud lies. Flipping both the detuning and the displacement from the focal plane ideally results in no change in the absorption image. This provides an additional method to locate the focal plane. As the focal plane is being scanned, the point where the image changes from having a hole in the center to a halo around it is the focal point.

Chromatic aberrations in the imaging system leads to a shift in the focal plane for different wavelengths. For absorption imaging, we work with monochromatic light and chromatic aberrations are not an issue. However, this shift has to be taken into account while aligning the 405 nm blue barrier (see Sec. 3.5.3). The shift in the focal plane, calculated using the ray tracing software OSLO, is tabulated in Table 3.6.

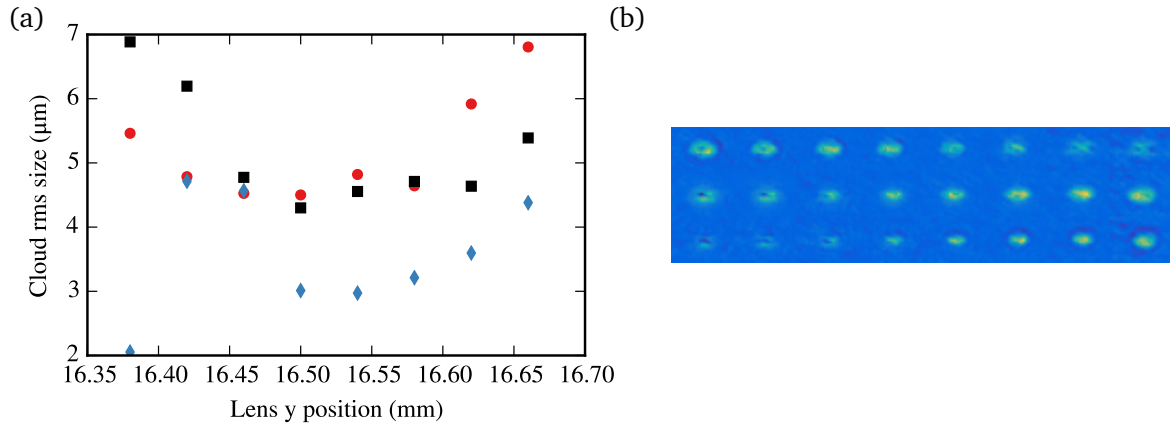


Figure 3.7: Focusing the imaging system. A small cloud is prepared in the ReST trap (see Sec. 5.2) and imaged in-situ for different lens positions. (a) The fitted width of the cloud as a function of the lens position. Red circles are for a 8 MHz red-detuned probe beam, blue diamonds are for a 8 MHz blue detuned beam and black squares are for an on-resonance probe. (b) The corresponding absorption images. The images in the top row are with a red detuned probe, middle row with an on-resonance probe and bottom row with a blue detuned probe. For a red detuned probe, a halo is seen around the cloud initially, which disappears. Eventually the cloud has a hole in it. The blue detuned probe shows the opposite trend.

Wavelength (nm)	Focus distance (mm)	shift (mm)	Magnification
780	69.64	0.0	5.34
405	71.26	1.62	5.30
1064	69.83	0.19	5.33

Table 3.6: Shift in the focal plane of the imaging system for the wavelengths used in the experiment.

Systematic effects in absorption imaging

An absorption image A , along with a reference image R without the atoms, and a dark image D is used to get the optical density profile OD_m of the cloud. The optical density is given by

$$\text{OD}_m = -\log\left(\frac{A-D}{R-D}\right). \quad (3.3)$$

The subscript in OD_m stands for the “measured” optical density. To obtain the actual column density and number of atoms from this measured optical density, various systematics have to be taken into account. Factors such as the detuning, intensity and polarization of the probe beam affect the absorption cross-section and hence the optical density.

Consider a beam with an intensity profile $I(x, y)$ propagating along the z direction, passing through a cloud of atoms with a density profile $n(x, y, z)$. A thin slice of thickness dz absorbs some of the light, resulting in a drop in the intensity, given by

$$dI = -\frac{n(x, y, z)\sigma_0 I}{1 + I/I_{\text{sat}} + (2\Delta/\Gamma)^2} dz. \quad (3.4)$$

Here σ_0 is the on resonance cross-section, Δ is the detuning of the probe beam, Γ is the natural linewidth and I_{sat} is the saturation intensity of the transition. This equation assumes a simple two level system without any optical pumping effects, which is true for the cyclic $F = 2, m_F = 2 \rightarrow F = 3, m_F = 3$ transition that we use for imaging. This is done by applying a magnetic field of 2 G along the probe propagation direction and setting the probe polarization to σ^+ (see Fig. 3.8a).

Integrating Eq. 3.4 over all z , we get

$$\int n(x, y, z)\sigma_0 dz = -\left[1 + (2\Delta/\Gamma)^2\right] \log\left(\frac{I_f}{I_0}\right) + \frac{I_0}{I_{\text{sat}}} \left(1 - \frac{I_f}{I_0}\right) \quad (3.5)$$

Here $I_0 \propto R-D$ and $I_f \propto A-D$ are probe intensities before and after hitting the atoms respectively. The optical density on resonance for low probe intensity is given by $\text{OD}_0 = \int n(x, y, z)\sigma_0 dz$. Using Eq. 3.3, we get

$$\text{OD}_0 = \left\{1 + (2\Delta/\Gamma)^2\right\} \text{OD}_m + \frac{R-D}{C_{\text{sat}}} \left\{1 - \exp(-\text{OD}_m)\right\}, \quad (3.6)$$

where C_{sat} is the number of counts on the camera corresponding to a probe beam with an intensity I_{sat} . From Eq. 3.6 we see that for a probe intensity comparable to I_{sat} , the relationship between OD_0 and OD_m is nonlinear and not just a simple rescaling. This has important consequences not only for the number of atoms in the cloud, but also the width and shape of the cloud[34]. We typically image with a probe intensity of $1I_{\text{sat}}$. If not corrected for, saturation of the transition leads to underestimating the atom number by about 70% and underestimating the width by 5%.

The camera counts C_{sat} for a $1I_{\text{sat}}$ probe beam is estimated by a method outlined in Ref. [35].

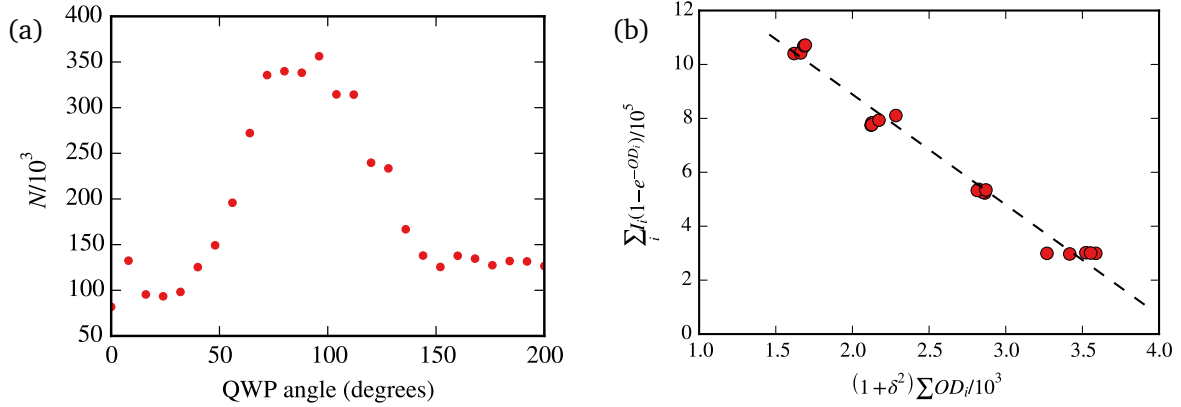


Figure 3.8: Probe polarization and intensity calibration. (a) A quarter wave plate is used to set the polarization to σ^+ . The optimal angle is found by scanning the quarter-waveplate and measuring the number of atoms in an absorption image. Ideally one would expect a 15x reduction in atom number when changing the probe polarization from σ^+ to σ^- based on the Clebsch-Gordon coefficients. However, the σ^- probe optically pumps the atoms to $m_F = -2$, which results in an increased absorption. (b) The slope of the fitted line gives C_{sat} , the camera counts corresponding to a $1I_{\text{sat}}$ probe beam (see text). $C_{\text{sat}} = 410 \pm 15$.

Summing Eq. 3.6 over a region of interest containing the cloud gives us

$$\sum \text{OD}_0 = P + \frac{1}{C_{\text{sat}}} Q, \quad (3.7)$$

where

$$P = (1 + (2\Delta/\Gamma)^2) \sum \text{OD}_m \quad (3.8)$$

and

$$Q = \sum (R - D) \{1 - \exp(-\text{OD}_m)\}. \quad (3.9)$$

The LHS of Eq. 3.7 is proportional to the number of atoms and does not depend on the probe intensity. We take a set of absorption images while scanning the probe intensity and calculate P and Q values for each image. The slope of the straight line when Q is plotted versus P gives the value of C_{sat} (see Fig. 3.8b). A consistency check is to measure the power broadened linewidth of the transition when scanning the frequency of the absorption probe.

Noise in absorption images

From Eq. 3.3, we see that the noise in the measured optical density ΔOD_m is given by

$$\Delta \text{OD}_m = \left\{ \left(\frac{\Delta A}{A} \right)^2 + \left(\frac{\Delta R}{R} \right)^2 \right\}^{1/2}. \quad (3.10)$$

If all technical sources of noise are eliminated, then ΔA and ΔR are limited by the photon shot noise in the probe beam. However in our experiment two major sources of noise dominate: camera noise and fringes in the absorption and reference beams. The camera noise is determined blocking all light to the camera and acquired a set of dark images. A histogram of the camera counts of the dark images fits well to a Gaussian centered at 30 counts with a width of a 3.8 counts. Assuming this camera noise is independent of the incident light, we find the noise ΔOD_m to be at least

$$\Delta OD_m \geq \frac{3.8}{R} \{ \exp(OD_m) + 1 \}^{1/2}. \quad (3.11)$$

For a typical absorption image with probe intensity of $1I_{\text{sat}}$ and an exposure time of $100\mu\text{s}$, we get 400 counts/pixel on the camera. Thus the noise in OD_m is at least 0.015/pixel.

The noise due to fringes in the probe beam is about 5-10 times higher than the camera noise. This is due to vibrations in the experiment causing the fringes to move from shot to shot. Fortunately, fringe removal algorithms can be used to find the ideal reference image for a particular absorption image [29, 36–38]. This technique successfully removes both noise due to moving fringes and due to power fluctuations and has been used to achieve shot noise limited imaging [39]. The fringe removal technique brings down the noise in OD_m to 0.018/pix, effectively limited by the camera noise. For an on resonance probe with $1I_{\text{sat}}$ intensity, this corresponds to a noise of $\sim 1\text{atom}/\text{pixel}$. For typical experiments, shot to shot variations in the atom number of the prepared sample is much higher and detection noise is not an issue. However, for the tunneling time experiments (see chapter 4) we need to detect extremely small changes in the rotation angle of the spin. In these experiments, camera noise will be a limiting factor.

3.5 Optical potentials

3.5.1 Hybrid trap and crossed dipole trap beams

The hybrid trap beam is generated by amplifying narrowband 1064 nm light from a NP Photonics Rock Fiber Laser with a Nufern fiber amplifier (model number PSFA-1064-50-15W-2-0). The schematic for generating the light is shown in Fig. 3.9. An AOM is used to control the power in the hybrid trap beam. The +1 order is used for the main beam, and the 0th order is sent to a second AOM, which controls the power in the crossed dipole trap beam. The hybrid trap beam is focused inside the cuvette at a small angle of $\sim 2^\circ$ with respect to the cuvette surface (the angle is slightly exaggerated in Fig. 3.9). This is to prevent the reflection from the cuvette from overlapping with the incident beam. Interference of the incident and reflected beam in the overlap region would otherwise create an optical lattice. Non-specular reflections from the cuvette still create a lattice with a small depth (< 1 recoil energy) and are a major obstacle towards one dimensional waveguide experiments[29]. The Superluminescent diode trap, described in Sec. 3.5.2, was developed to overcome this problem.

The beam power is measured using a Newport 818P-020-12 high power detector. The voltage

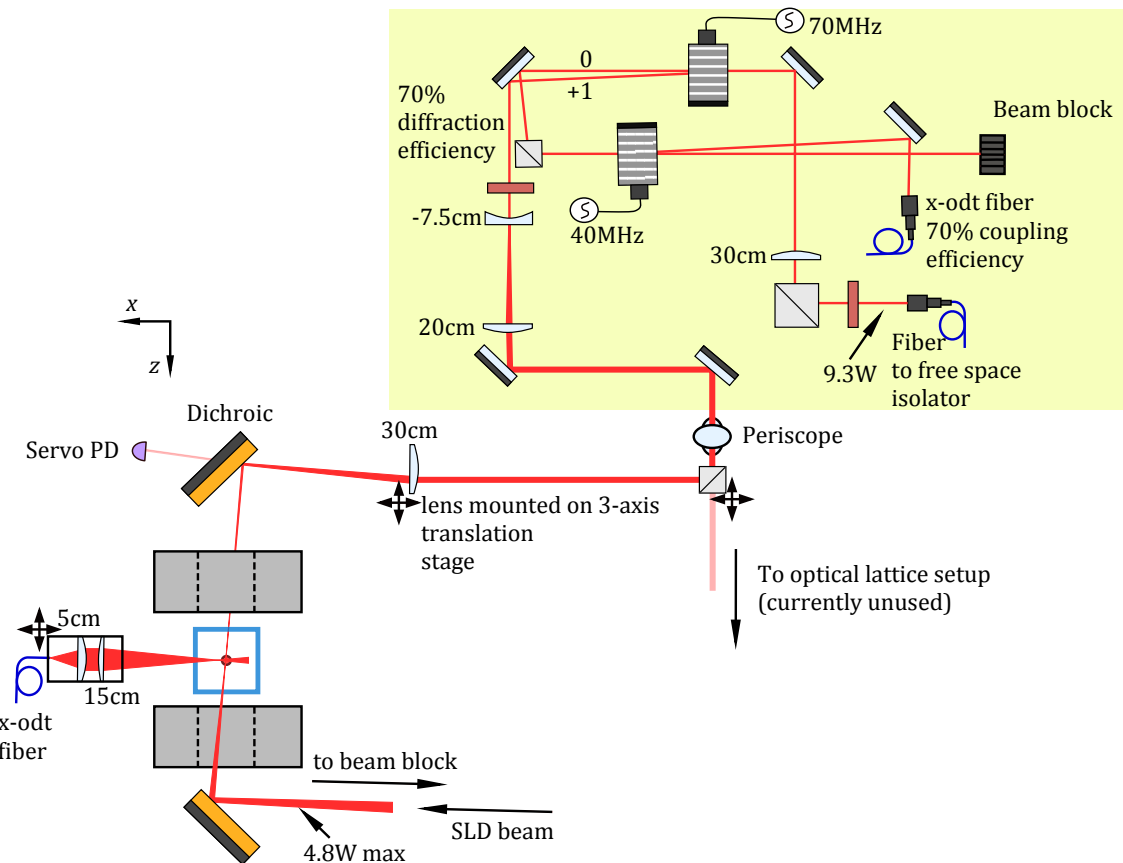


Figure 3.9: Schematic of the optical layout for generating the hybrid trap and the crossed dipole trap beams. Light from the fiber amplifier is coupled out using a fiber to free space isolator. The area indicated in yellow is boxed to contain stray light scattered from optics. The optics for focusing the cross dipole trap beam on the atoms are mounted in a 30 mm cage module. This module is at a 22° inclination with the optical table.

reading of the power meter is calibrated against a Thorlabs S121C sensor for powers less than 500 mW and extrapolated for higher powers. The calibration obtained is 0.12 V/W for 1064 nm light.

The Nufern amplifier has a maximum output power of 15 W. However, the power has decreased progressively with the age of the amplifier. It has dropped from 13 W at the time of installation to 9.3 W in March 2014. Since then, the power has stabilized. The decreasing power limits the maximum trap depth and hence the efficiency of the transfer from the quadrupole trap to the hybrid trap. In the future, if the power drops further, one solution is to focus the beam tighter to get a larger trap depth while trading off trap volume. BECs have been achieved with less than 1 W of power for smaller beam waists¹.

A maximum of 4.8 W is available at the atoms in the hybrid trap beam. For the crossed dipole beam, a maximum of 0.5 W is coupled in angle polished fiber to avoid damaging the front facet of the optical fiber.

The hybrid trap beam is focused to a waist of $80 \pm 5 \mu\text{m}$. The waist of the crossed dipole trap has not been measured for the 1064 nm light, since the module was already installed and used previously for 980 nm light. The expected waist, if chromatic aberrations do not significantly change the spot size, is $12 \pm 1 \mu\text{m}$. However, the crossed dipole trap beam is off-focus from the atoms and its size is larger than the minimum waist. This is to get a larger trap volume and a weak trapping frequency along the z direction.

3.5.2 Superluminescent diode beam

The discovery of the accidental lattice created by reflections of the hybrid trap beam off the cuvette (see Sec. 3.5.1 and Sec. 5.4 in Ref. [29]) posed a significant problem for the tunneling time experiments. A number of possible solutions were proposed and tried out before settling on using a second optical dipole trap beam created using light from a broadband Superluminescent Diode (SLD). These attempts are outlined below.

Working in a gravity compensated waveguide. One way to get rid of the lattice is to simply reduce the power in the laser beam until the lattice depth is too small to be noticeable. However, in the presence of gravity, there is no bound state below a critical power. By adding a vertical magnetic field gradient the tilt due to gravity can be reduced, or completely canceled, thus requiring less power to hold the atoms.

This approach works to some extent, however Bragg diffraction can still be seen for small accelerations of $\sim 2 \text{ m/s}^2$. Working with very low powers reduces the transverse trapping frequency. While this reduces the inter-particle interaction energy and the thus velocity spread when the wavepacket expands in the waveguide, it also increases the transverse size of the wavepacket. For all the tunneling experiments, we want to be in a regime where the transverse size is smaller than the Rayleigh range of the tightly focused barrier beam (see Sec. 4.2), which is $8 \mu\text{m}$ for the second generation barrier.

¹Trey Porto, private communication

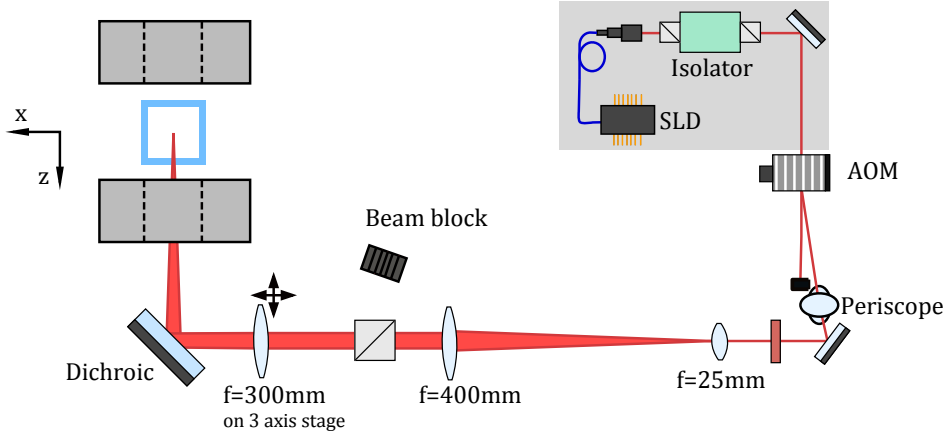


Figure 3.10: Super Luminescent Diode beam layout.

Additionally, magnetic levitation works only for one spin state. Thus, this technique cannot be used for the Larmor time experiments where multiple spin states need to be trapped.

Suppressing the lattice using phase modulation. Phase modulating the ODT beam creates sidebands in the spectrum of the light. This would create multiple lattices with slightly different spacings. The modulation frequency and depth of modulation can be adjusted so that these lattices interfere destructively at the position of the atoms. The frequency of modulation required for this to happen is $c/2L = 7.5 \text{ GHz}$ for a cuvette length $L = 2 \text{ cm}$. The modulation can be achieved either by using an EOM, or by modulating the current through the laser diode used for seeding the fiber amplifier.

We attempted current modulation by adding a bias tee close to the diode and driving it using the Dual μ -Wave EOM driver designed by Alan Stummer. The driver is designed to drive an EOM and produce sidebands at either of the ^{85}Rb and ^{87}Rb hyperfine transitions at 3.03 GHz and 6.8 GHz respectively. It gives a maximum of 21 dBm of power at 3 GHz. The light from the diode is sent to a fast photo detector and monitored on a spectrum analyzer. Small sidebands were seen in the spectrum when modulated at 3 GHz. However, no sidebands were seen when modulating at 6.8 GHz. We concluded that we need more microwave power, better coupling and better impedance matching to be able to modulate at 7.5 GHz. The time and money that would be spent was considered not worth it, given that we would not achieve perfect suppression. We decided to abandon the project and explore the possibility of using broadband light for the optical dipole trap.

Seeding the fiber amplifier with broadband light. The Nufern fiber amplifier used for the hybrid trap has a bandwidth of $\sim 20 \text{ nm}$, centered at 1064 nm. We decided to seed the amplifier with broadband light so that the ODT beam has a small coherence length ($< 1 \mu\text{m}$). Light from Amplified Spontaneous Emission (ASE) sources and Super Luminescent Diodes (SLD) have a bandwidth of tens of nanometers and have extremely short coherence lengths while still having good spatial mode since the light is fiber coupled. ASE sources have been used in ultra cold atom traps to avoid unintentional modulations in the trapping potential due to speckle and multiple reflections[40].

The fiber amplifier needs a minimum of 50 mW of polarized seed power in fiber. While exploring our options for a broadband source, we found that most ASE sources at 1064 nm were limited to ~ 20 mW of power, whereas SLDs offered up to 300 mW of power and also more power per dollar.

A 100 mW SLD manufactured by Innolume was used to seed the the fiber amplifier. The total power output of the amplifier was about 30% less than when seeded with a narrowband source at 1064 nm. Nevertheless, we were successful in trapping atoms in the ODT and create a BEC. The atoms expanded smoothly in the waveguide and there were no signs of Bragg diffraction when the BEC was accelerated in the waveguide. Unfortunately, after a week of operation, the SLD malfunctioned, giving only 100 μ W of power. Upon inspection, the technical staff at Innolume found the front facet of the diode to be damaged. We initially suspected feedback from the the fiber amplifier to have caused the damage. However, Nufern support informed us that the fiber amplifier has an optical isolator at the input which is designed to operate at 1064 ± 5 nm and in theory should not be feeding back to the SLD. The bandwidth of the SLD is 22 nm, so we cannot completely rule out the possibility of the feedback causing damage.

Not knowing the cause of the failure and lacking detailed spec sheets of the amplifier, we decided not risk damaging another SLD. Instead, we opted for using a higher power SLD beam as a second stage optical dipole trap.

Second Stage Optical Dipole Trap. A 300 mW Innolume SLD-1060-20-YY-300 diode is used for the second stage ODT beam. The SLD comes in a 14 pin butterfly package with a built in TEC and thermistor and a polarization maintaining pigtailed fiber output. It is mounted on a Thorlabs LM14S2 mount and powered by a Wavelength Electronics LDTC1020 laser diode and TEC controller. Auxiliary electronics and the box for the driver were built by Ramon Ramos and the optics were assembled and tested by David Spierings.

The optical layout for the SLD beam is shown in Fig. 3.10. The SLD mount, along with the fiber collimator, isolator and a steering mirror are mounted on a 12" \times 12" portable optical breadboard which is screwed on to the main table. A single pass AOM is used for controlling the power in the beam. A periscope is used to raise the beam height to 14.5 cm, followed by a 16x Galilean telescope. A PBS is used to deflect the vertically polarized counter propagating hybrid trap beam towards a beam dump. Finally, a 300 mm achromat is used to focus the beam at the atoms. The power in the SLD beam is measured before the telescope. The power reaching the atoms was found to be $\sim 55\%$ of this power, with an unusually low 60% transmission at the PBS, even after adjusting the polarization with a half-wave plate. We suspect that this is due to the waveplate being a multi-order waveplate and the SLD light being broadband.

When the SLD beam is aligned with the atoms, it is exactly counter propagating with the main hybrid trap beam. The hybrid trap beam power can go as high as 5 W and we were concerned that some of this light might get coupled into the SLD diode and damage it. A PBS placed in the path deflects 99.9% of the hybrid trap light towards a beam dump. The optical isolator right after the collimator provides additional isolation. At full hybrid trap beam power, we measured 10 μ W passing through the isolator when the AOM controlling the SLD power was off. This should not

damage the SLD.

The focused spot size and the divergence of the beam was measured “offline”, by assembling all the optics on a separate optical table. Knife edge scans at multiple points along the beam propagating direction were done to determine the beam waist ($1/e^2$ radius) to be $15\text{ }\mu\text{m}$ and the Rayleigh range to be $650\text{ }\mu\text{m}$. During the knife edge scans, the beam was found to be fairly Gaussian. However, absorption images of atoms trapped in the beam reveal the presence of a side lobe in the beam (Sec. Fig. 3.12(d))). Lowering the power in the SLD beam removed atoms from the side lobe.

The SLD beam was aligned coarsely by ensuring that it counter propagates with the hybrid trap beam. The atoms were used for fine alignment. A cloud of thermal atoms close to the critical temperature was prepared in the hybrid trap, after which the power in the SLD beam was ramped up. The waist of the SLD beam is 5 times smaller than the hybrid trap beam. Thus ramping up the SLD beam creates a small dimple in the trapping potential, shrinks the trap volume and increases the phase space density[41]. If the cloud is close to the critical temperature, the increased phase space density causes part of the cloud to condense. The SLD beam was aligned by maximizing the condensate fraction created due to this “dimple effect”.

A BEC created by exploiting the dimple effect is reversible. The phase space density can be increased by increasing the depth of the dimple without the need to evaporatively cool the cloud. Lowering the depth of the dimple will bring back the thermal cloud, as demonstrated first in Ref. [41] and shown here in Fig. 3.11.

3.5.3 Barrier Beam

We use a tightly focused blue-detuned light beam as a barrier for the tunneling experiments. The probability of transmission through a tunnel barrier is appreciable when the de Broglie wavelength of the tunneling atom is comparable to the barrier width and goes down exponentially with increasing barrier width(see Sec. 4.2). Hence, it is crucial to create a thin tunnel barrier to observe tunneling. A Gaussian beam with a waist w_0 , when focused using an ideal lens with a focal length f , focuses to a waist w_f given by

$$w_f = \frac{\lambda f}{\pi w_0}, \quad (3.12)$$

where λ is the wavelength of the light. From Eq. 3.12, we see that for a tight focus, one should use light with a short wavelength, focus using a short focal length lens and use a beam with a large waist w_0 . We chose 405 nm light to generate the barrier beam since the short wavelength allows for a tighter focus and also because 405 nm diodes are cheaply available. It is blue-detuned to both the ${}^5S \rightarrow {}^5P$ transition at 780 nm and the ${}^5S \rightarrow {}^6P$ transition at 420 nm. The indigo light is generated by a Mitsubishi ML320G2-11 laser diode and gives 120 mW of light, 50 mW of which is available in single mode fiber.

To bring this light to a tight focus, a custom high Numerical Aperture (NA) objective is used. Eq. 3.12 gives the focused waist of a Gaussian beam when a diffraction limited imaging system is used. Various aberrations occurring in real lenses must be accounted for and corrected to achieve

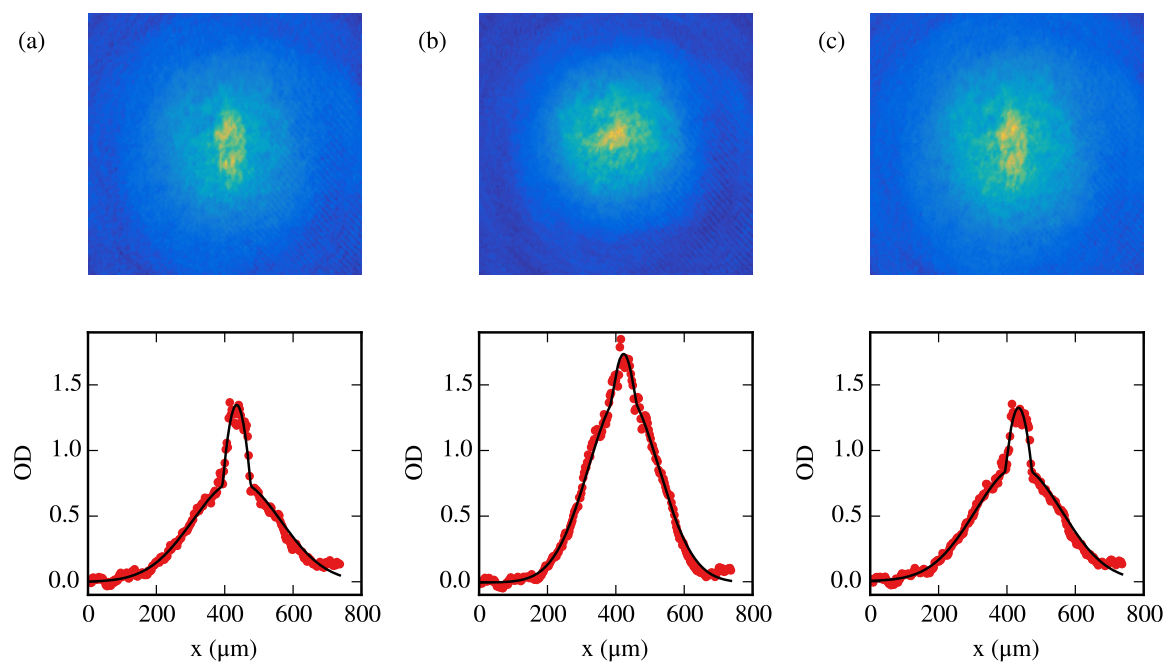


Figure 3.11: Reversible formation of a BEC. A thermal cloud with 1M atoms at a temperature of 130 nK, close to the critical temperature, is prepared in the hybrid trap and the SLD power is ramped up. (a) We see the emergence of a small BEC fraction after ramping up the beam power. A fit to a Gaussian + Thomas Fermi profile shows that the temperature has gone up to 230 nK, even as the phase space density increases. (b) This cloud is thermal again with the original temperature of 130 nK when the SLD power is ramped down after ramping it up first. (c) The BEC fraction re-emerges the second time the power is ramped up.

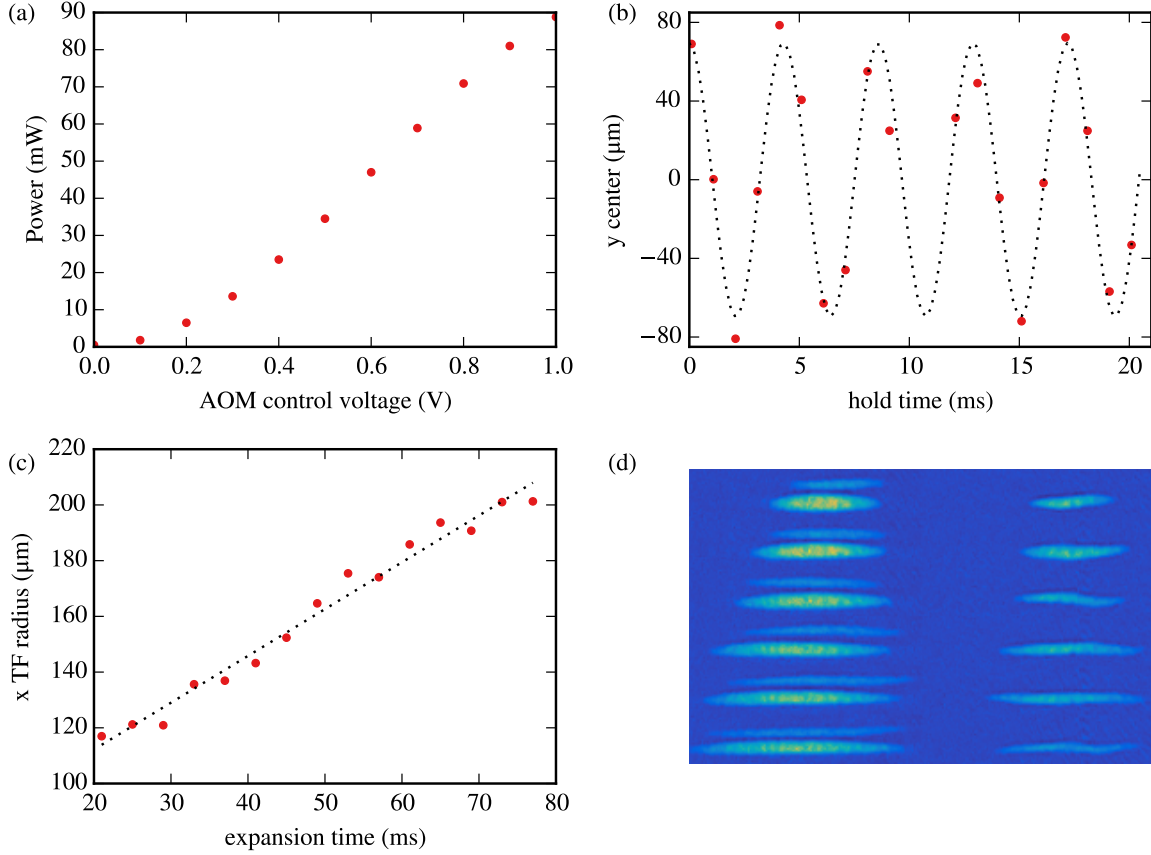


Figure 3.12: SLD Beam and trap characteristics. (a) Power in the SLD beam measured right before the 25 mm lens (see Fig. 3.10). (b) Measuring vertical trap frequency f_y by observing oscillations after displacing the BEC. Fit to a sinusoid gives a trap frequency of $230.0(2)$ Hz. A control voltage of 1.0 V corresponding to a beam power of 90 mW was used. (c) Thomas Fermi radius of a cloud expanding in the SLD waveguide after the cross dipole trap beam is switched off. Fit to a straight line gives $v_{TF} = 1.7 \text{ mm/s}$, which corresponds to an rms velocity spread of 0.65 mm/s. (d) Absorption images of the BEC expanding in the SLD waveguide. Atoms are trapped in two minima for high SLD beam powers (left). When the SLD power is lowered, only one trap minima is seen (right).

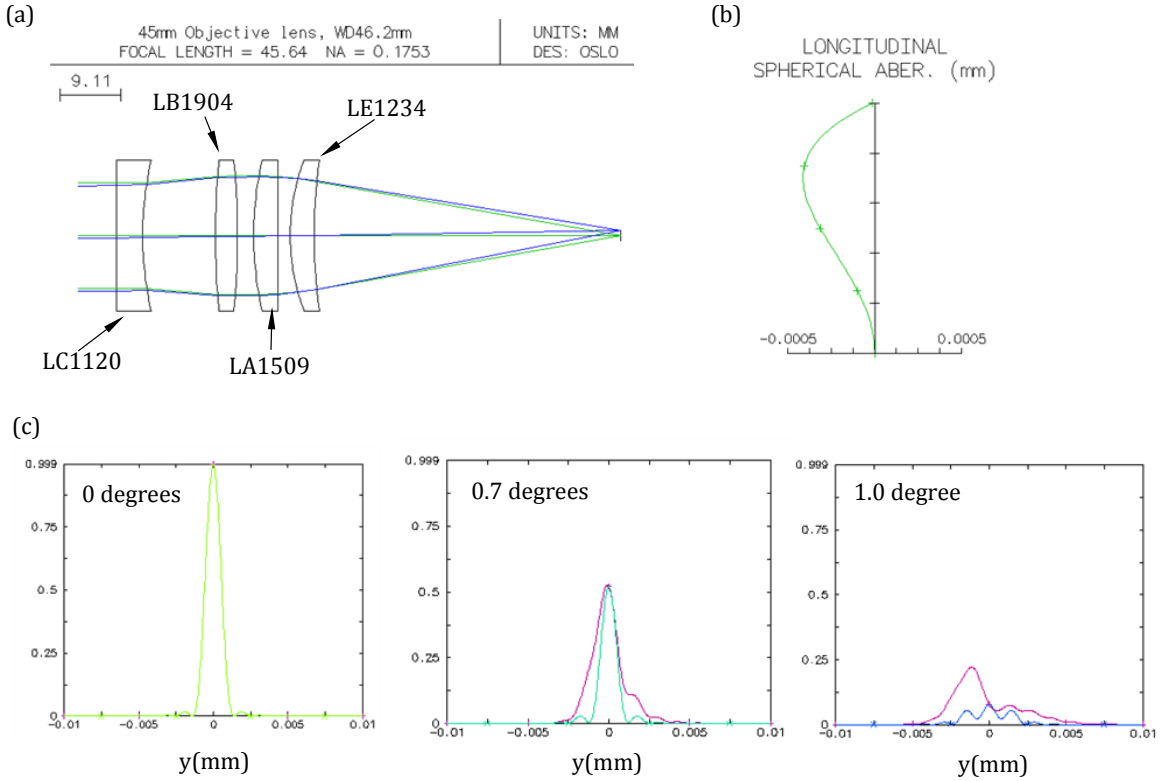


Figure 3.13: Design of the barrier objective in OSLO. (a) Plan showing the lenses and their positions. All lenses are Thorlabs N-BK7 A-coated singlet lenses. The part numbers for all the lenses are indicated. (b) Longitudinal Spherical aberration (x-axis) as a function of the ray height (y-axis). (c) Point spread function for an angle of incidence of 0.0° , 0.7° and 1.0°

this diffraction limited performance. In our system, we are primarily concerned with Spherical aberrations. Since the beam is monochromatic, chromatic aberrations are not important. We carefully align the beam to be incident normally on the lens and at the center to minimize coma and astigmatism.

The objective design, created using the ray tracing software OSLO, is shown in Fig. 3.13. The design is based on the “Alt objective” [42] and consists of 4 singlet lenses. The basic principle behind the design is to divide the total power of the lens between three positive lenses to reduce spherical aberrations. A fourth negative lens is then introduced to cancel the residual aberrations. The original design from Ref. [42] is used as a starting point for the design and all lengths are scaled to get our desired working distance of 45 mm. The lenses were then replaced with stock lenses with the closest focal length, optimizing the distance between the lenses with each replacement. The optimization is carried out to minimize the total spherical aberrations.

The lenses are assembled in a Thorlabs 1” lens tube. When the lenses are inserted in the tube, there is some wiggle room for the lenses which may cause them to be slightly off-center when

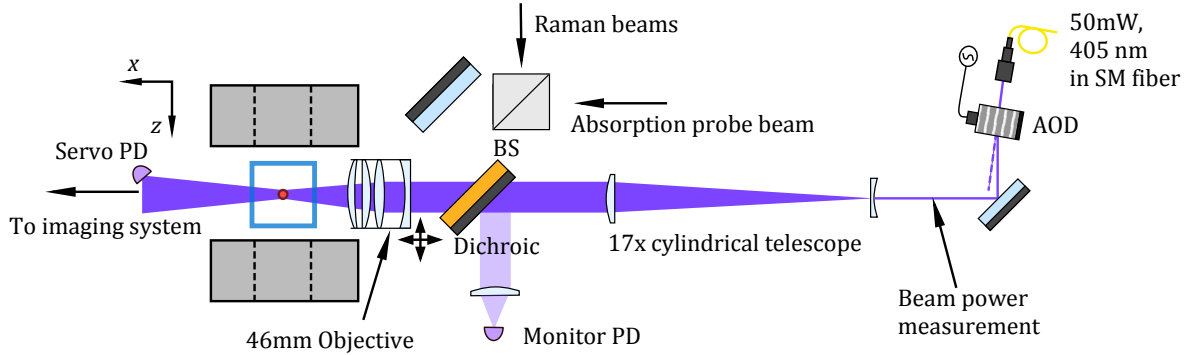


Figure 3.14: Schematic of the setup for generating the barrier sheet. Light from a single mode fiber is sent to an AOD to scan the beam in the horizontal direction. It is then expanded vertically using a cylindrical telescope and then focused on the atoms using the custom high NA objective. The objective is mounted on a two axis motorized translation stage. A small fraction of the light is picked off at the dichroic mirror and sent to a photo-diode to monitor the power in the beam. A second Servo PD picks off a part of the beam and is used to stabilize the beam power.

assembled. To reduce this wiggle, the lenses are taped with one round of foil tape around the edge so that they fit snugly inside the tube. The distance between the lenses was set by using Thorlabs retaining rings. While the spec'd thickness of the rings is 2 mm, there is some tolerance in these rings. We measured the thickness of many rings and found a combination of rings that matches closest to the design spacing. The distance between the lenses in the design was then changed to the actual spacings and the rest of the distances were optimized. By doing this, we could use standard retaining rings instead of having to machine our own spacers. Starting from the concave lens, LC1120, the measured width of the spacers is 10.08 mm (5 retainer rings), 6.05 mm (3 retainer rings) and 4.00 mm (2 retainer rings). The design calls for a tolerance of less than $100\text{ }\mu\text{m}$ for the lens spacings and decentration. Our method of assembling the lenses might have resulted in exceeding these tolerances, since we see some residual spherical aberrations in the focused spot, as described later.

The setup for focusing the beam is shown in Fig. 3.14. A thin sheet of light is generated by expanding the beam vertically using a pair of cylindrical lenses. This creates a beam with a high aspect ratio. When the beam is focused, the aspect ratio is inverted and it is focused tightly in the vertical direction. Additionally, an Acousto-Optic Deflector(AOD) is used to scan the beam in the horizontal direction to create a flat intensity profile in a $100\text{ }\mu\text{m}$ region (see Fig. 3.15(d)). The objective is mounted on a 3-axis translation stage. The two horizontal translation stages are electronic and can be controlled via GPIB. This is convenient while aligning the barrier beam as the alignment procedure can be automated.

Fig. 3.13(c) shows the Point Spread Function(PSD) of the lens for different incident angles. We see that the the PSD is severely distorted when the incident angle is greater than 0.5° and the performance of the objective lens degrades. Hence, the barrier beam has to be aligned carefully to ensure that it is centered on the objective lens and is parallel to the the optical axis of the lens.

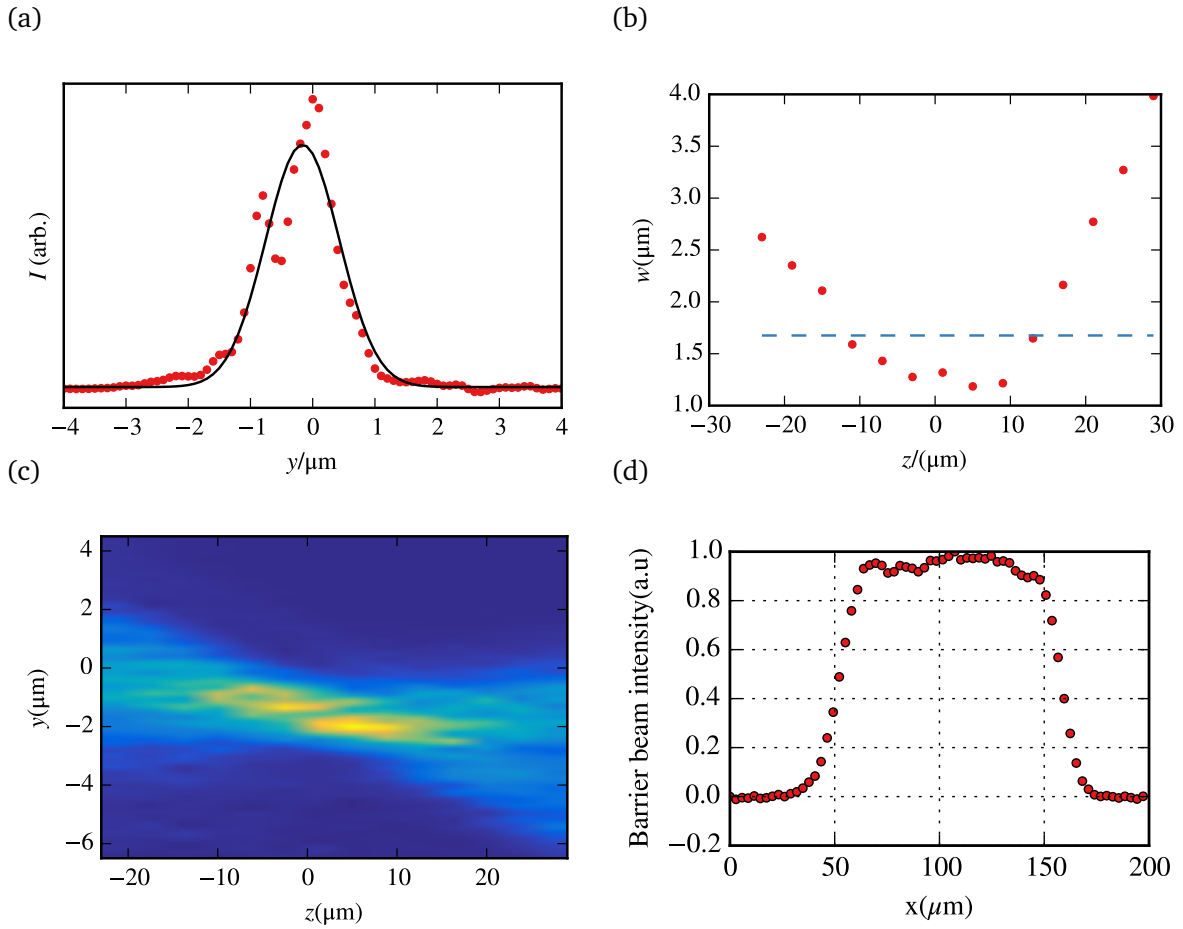


Figure 3.15: Characterizing the focused beam using knife edge scans. (a) The intensity profile of the beam at its focus. A fit to a Gaussian profile gives a waist of $1.3(1)\mu\text{m}$. (b) Fitted waist as a function of the position along the propagation direction of the beam. (c) 2D color map of the intensity profile around the focus. (d) A flat beam profile in the non-focused direction achieved by scanning the barrier beam using an acousto-optic deflector.

This is achieved by aligning the back reflection of the incident beam off the first flat surface of the objective to match with the incident beam. The beam is centered by inserting an iris at the front face of the objective lens. We estimate that we can align the incident angle to be less than 0.3° and the decentration to be less than 0.5 mm.

To test the performance of the objective, we measure the intensity profile of the focused beam using knife edge scans, shown in Fig. 3.15. These scans are done “offline”: the setup is assembled on a separate table and a 2 mm thick glass slide is used instead of the cuvette. The alignment and the beam profile measurements were done several times so that we were confident about the alignment procedure followed as there is no way to measure the beam profile inside the vacuum chamber.

The measured beam profile gives a waist of $1.3(1)\mu\text{m}$ at the focus. This is higher than the expected diffracted limited waist of $0.85\mu\text{m}$. We suspect this is due to residual spherical aberrations caused due to exceeding the tolerances while assembling the lenses. Indeed, in Fig. 3.15(b) we see that the divergence of the focused beam is not symmetric around the focus, which is a sign of

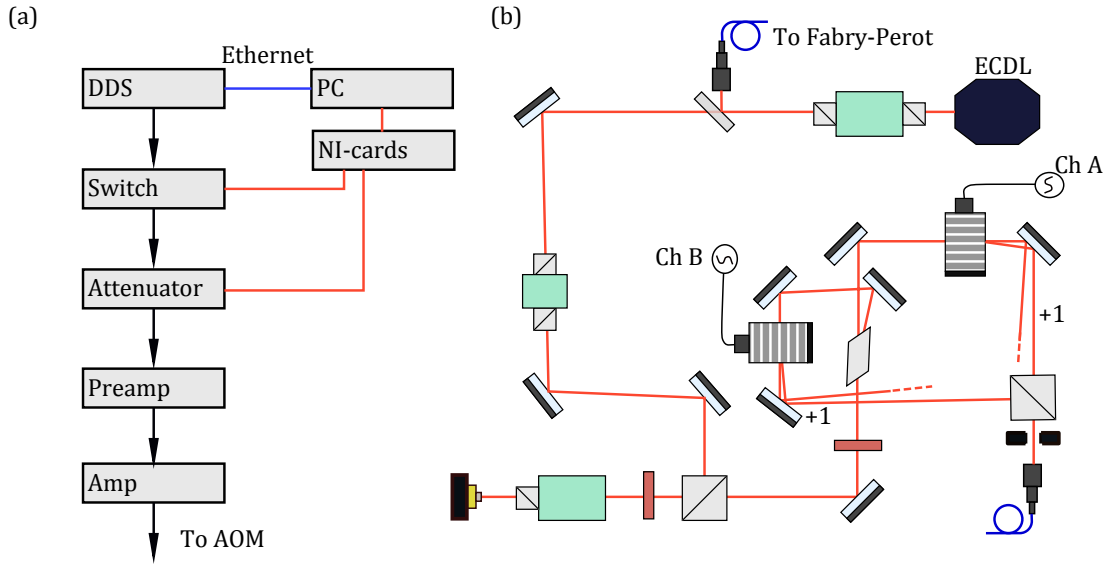


Figure 3.16: Generating Raman light. (a) Schematic for generating RF signals to drive the Raman AOMs. The signal from a 4 channel DDS is sent to a switch and attenuator to control the RF power. The signal then undergoes two stages of amplification before it is sent to the AOM. (b) Light generation for the Raman beams. An ECDL tuned to the “magic-zero” wavelength is used to injection lock a free-running diode. The power from the diode is split and sent to two AOMs. These AOMs are driven with RF signals which have a frequency difference corresponding to the two photon detuning. The diffracted order from these AOMs is combined at a PBS and then fiber coupled into a PM fiber.

spherical aberrations. We also found that removing the glass slide did not change the beam profile significantly, since there is already significant spherical aberrations in the beam. A second suspicion is the collimator used for collimating the light from the fiber. While it is spec'd to give diffraction limited performance, we have seen that the beam profile has a faint ring around the central Gaussian beam. Additional tests are needed to determine and fix the cause of this.

The barrier height due to the AC stark shift experienced by the atoms is directly proportional to the intensity of the beam. For the interaction assisted tunneling experiments, it is essential to determine this barrier height accurately. For this reason, we measure the power in the beam just before the expanding telescope and carefully measure the transmission through all the optics to determine the power inside the vacuum chamber. The total transmission through all the optics is $57.5 \pm 4\%$. The biggest error comes from the transmission through the dichroic mirror, which is slightly polarization dependent.

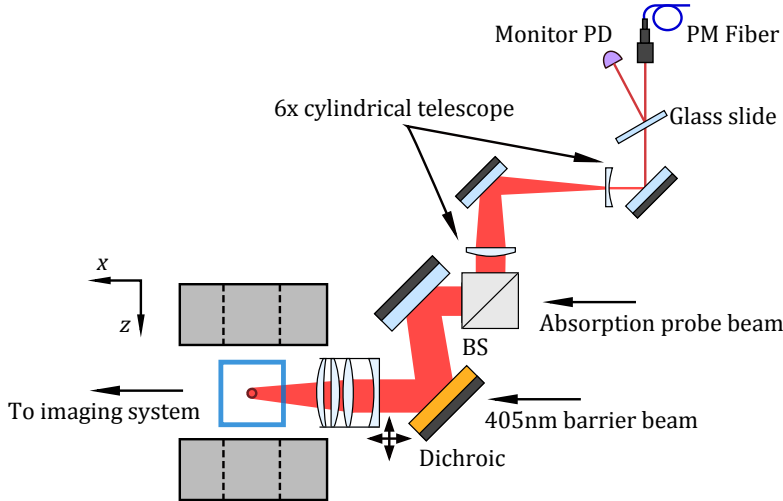


Figure 3.17: Schematic of the setup to focus the Raman beams on the atoms.

3.6 Raman beams

To measure the tunneling time, we plan to implement a clock by focusing a pair of Raman beams inside the tunneling region (see chapter 4). These Raman beams couple the Zeeman ground states of the atom via a two photon transition. The two photon resonance occurs when the frequency difference Δf between the two Raman beams is equal to the Zeeman splitting $\mu_B g_F B / h = 0.7 \text{ MHz/G} \times B[\text{G}]$. We typically operate in a low B field of 1 – 3 G and thus need a frequency difference Δf of 0.5 – 2MHz between the two Raman beams.

In addition to being on the two photon resonance, the Raman beams need to satisfy two other conditions. Firstly, they should be far away from any real atomic transition so that the scattering rate is low. Secondly, the AC stark shift due to the Raman beams should be low enough to not disturb the tunneling process. These two conditions can be satisfied when the Raman beams are tuned to a “magic wavelength” where the AC polarizability of the atom vanishes [43–45]. This happens when the AC stark shift contributions of two excited states are equal and opposite. For ^{87}Rb , the magic-zero wavelength corresponding to the $^5P_{1/2}$ and $^5P_{3/2}$ transition occurs at 790.03 nm.

The electronics and optics for generating the Raman beams were assembled by Sepehr Ebadi. A schematic is shown in Fig 3.16. An ECDL tuned close to the 790.03 nm magic-zero wavelength is used to injection lock a free running diode to get more power. The wavelength is measured using a Bristol 521 wavemeter. The wavemeter has a small offset error of 0.02 nm, which was measured by sending laser light locked to the D2 line. Light from the injection lock diode is split using a Calcite beam displacer and sent to two AOMs.

The AOMs are driven by RF signals with frequencies f and $f + \Delta f$ so that the two beams are on two photon resonance. The RF signals are derived from a 4-channel DDS (Direct Digital synthesis) box designed and built by Alan Stummer. The box uses a Analog Devices AD9959 DDS chip with a 100 MHz reference clock, derived from a crystal oscillator (part number Connor-Winfield

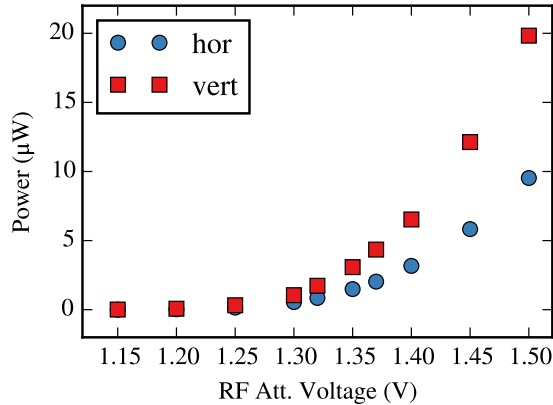


Figure 3.18: Raman beam power at the output of the PM fiber as a function of the control voltage applied to the RF attenuator.

TB524-100.0M) with a ± 1 ppm frequency stability. A Rabbit Minicore RCM6760 controller is used to program the DDS via Ethernet to set the amplitude and frequency of the DDS signal. A mini-circuits switch (ZASWA-2-50DR+) and voltage controlled attenuator (ZX73-2500-S+) are used for controlling the power of the signal during the experimental cycle. The DDS signal is amplified using two stages of amplification: the first using a mini-circuits ZFL-500-BNC amplifier and the second using a mini-circuits ZHL-1-2W(+) amplifier. The voltage controlled attenuators have an exponential response to the control voltage, as shown in Fig 3.18.

The diffracted light from the two AOMs is combined at a PBS and coupled into a PM fiber, which is then sent to the vacuum side of the setup (see Fig. 3.17). The output of the PM fiber is first expanded horizontally using a 6x cylindrical telescope before focusing using the barrier objective. This focuses the Raman beams to a tight focus of $4.2 \mu\text{m}$ horizontally. In the vertical direction, the waist of the Raman beam is $24 \mu\text{m}$. These waists are measured by imaging the Raman beam using the imaging setup depicted in Fig. 3.5.

Currently, the Raman beams are aligned by adjusting the position of the final focusing lens (the barrier objective). Since both the barrier beam and the Raman beams are focused using the same barrier objective, this would not work for future experiments where they are both used simultaneously. A new alignment scheme will have to be devised to independently align them.

We typically operate with around $15 \mu\text{W}$ of power in each Raman beam to get a two photon Rabi frequency of $\sim 1 \text{ kHz}$. This corresponds to a peak intensity of 9.5 W/cm^2 in each of the Raman beams. We had initially anticipated that we would need much more power in the Raman beams as we are quite far off the single photon resonance. However, the tight focusing of the Raman beams works to our advantage and gives us a high intensity for a small amount of power. Theoretically determining the expected two photon Rabi frequency is not trivial as the effect of the entire excited state hyperfine manifold has to be taken into consideration[46].

The ECDL was used to injection lock a free running diode for fine tuning of the wavelength to precisely determine the magic-zero wavelength. However, it was found that the AC stark shift

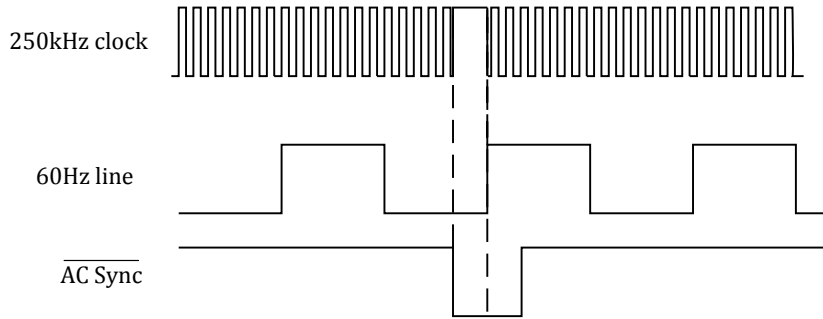


Figure 3.19: Synchronizing the clock to the line voltage. The clock is pulled to high at the rising edge of AC Sync and reset to the clock line at the rising edge of the 60 Hz line voltage. The timings shown are not to scale.

is negligibly small in a 0.05 nm range around the magic wavelength. Hence, after determining the magic wavelength we no longer used the ECDL and let the injection lock diode free run. The wavelength of the free running diode is found to be stable to 0.02 nm within a single day. The optical isolator after the diode has to be aligned carefully when the diode is free running to avoid optical feedback.

3.7 Control and Data Acquisition

3.7.1 Hardware and Timing

The experiment is controlled using digital and analog outputs from three National Instruments cards connected to PCI slots on the main control PC. All digital lines are provided by a NI PCI-6229 board (device name: Dev1). It provides up to 48 digital I/O lines and 4 16-bit analog outputs. Of these, 24 digital lines (Dev1/port0/line8:31) and 4 analog outputs (Dev1/ao0:3) are currently being used. This card receives an external clock as input (on line /Dev1/PFI8), which times the experiment.

The clock is built into the line voltage synchronization circuitry and comprises of a ECS-2100A 2 MHz oscillator divided down to 250 kHz, giving a resolution of $4\mu\text{s}$. The clock can be paused when an AC-Sync signal is received and resumed at the rising edge of the 60 Hz line signal (see Fig. 3.19). The clock is synchronized to the line voltage after preparing a BEC and before beginning any experiment on the BEC. This ensures the magnetic field noise at the line frequency has the same phase in every shot.

Two NI PCI-6229 cards (device names: Dev2 and Dev3) provide 8 12-bit analog outputs per card (Dev2/ao0:7 and Dev3/ao0:7) with a voltage range of $\pm 10\text{ V}$. The sample clocks for these cards is provided by the digital card. All channels are buffered using a home-built buffer box before

sending the voltages to the experiment. This protects the cards against feedback and provides a low output impedance to drive $50\ \Omega$ loads.

Function generators, oscilloscopes, power supplies, motorized translation stages, laser diode controllers and other remotely controllable devices are connected via GPIB to the same control PC. GPIB commands can be sent either at the beginning of a ramp or during the ramp through timed callbacks (see Sec. 3.7.3).

A second computer is responsible for data acquisition. A National Instruments PCI-1424 card acquires images from the main absorption imaging camera (see Sec. 3.4.10). A Pulnix TM-7AS CCD camera used for monitoring the upper MOT is connected via a VGA to USB adapter and a Thorlabs DCC1545M CMOS camera connected via USB monitors the lower MOT (see Fig. 3.21). Laser powers in the experiment are monitored by photo-diodes connected to a Labjack-U3-HV data acquisition device, which is also connected via USB.

Temperature at various places inside the lab is constantly monitored and logged using a second Labjack-U3-HV device (see Sec. 3.7.5).

3.7.2 Migration to python

Until 2012, LabView was used for controlling the experiment as well as for data acquisition. While it is great for prototyping and quickly creating user interfaces, maintaining and extending a large LabView project can quickly become a frustrating experience as one tries to navigate through a spaghetti of virtual wires. For this reason, we decided to move away from LabView, writing all new code in python and slowly migrating old LabView code to python as well. Everything except acquiring absorption images now runs on python. Python was chosen as it is relatively easy to learn, has a large user base and a helpful community, and mature packages for scientific computing. The following modules were indispensable for migrating from LabView to python:

- **ctypes**: Almost all hardware vendors provide a C library to interface with their devices. The `ctypes` module allows easy access to functions in these libraries.
- **numpy, scipy**: These packages provides data structures and functions for linear algebra and scientific computing.
- **PyQt4**: Provides bindings for the Qt Framework to create GUIs. The Qt-designer software was used to quickly design GUIs needed for the experiment.
- **pyqtgraph**: Provides Qt widgets for interactive plots.
- **PyDaqmx**: Wrapper for NIDAQmx C library. Provides access to National Instruments data cards in python.
- **PyVisa**: Used for sending GPIB commands to various instruments in the lab.
- **zeromq**: An advanced socket library used for inter process communication. It is used by processes on different computers to talk to each other via TCP/IP.

3.7.3 Rampage

Rampage is the software used to program digital and analog voltage ramps that are sent to the National Instruments cards. It is written in python and is primarily GUI based, with modules available to edit and run ramps over the command line. It follows a client-server architecture: the server is a command line program running on the control PC and the client communicates with the server via TCP/IP using zeromq. This allows the experiment to be controlled from anywhere within the local network. The server runs on Windows, since it requires the National Instruments DAQmx libraries. However, the client can run on Windows, Linux or Mac since all the modules used are cross-platform.

The design of rampage is based on two key observations about cold atom experiments. Firstly, over the entire length of the ramp, most channels change only in a small time segment. For example, the channel modulating the frequency of the trapping light is mostly set to its default value, except during the 12 ms molasses stage when it is swept. Secondly, the timing of many events is fixed relative to a few key events. For example, when acquiring an absorption image, the timing of the shutters, frame grabber, and AOM modulation is fixed with respect to the time when the image is to be taken.

A ramp is composed using “key-frames”, which are positions in time. This concept is borrowed from animation software. The value of an analog or digital channel is defined at certain (but not all) key-frames, along with a method of interpolation between key-frames. In the example above, the trapping frequency would be defined only at two points in the ramp description: at the beginning and end of the molasses stage, eliminating the need to define a value in each time segment. The time position of a key-frame is defined with respect to any other key-frame and can be negative. This is particularly useful for shutters, which need to be opened a few ms before the laser is flashed on. Thus the key-frames form a tree structure with one main trunk and a few small branches. Fig. 3.20 shows a screen shot of the GUI editor.

The client GUI is used to create a ramp description, which is stored in a JSON (JavaScript Object Notation) format and added to a queue on the server. The server creates the voltage ramps from the ramp description, uploads it onto the cards and starts the ramp. Ramps can be modified and queued up even as the previous ramp is running. This minimizes dead time between runs.

Apart from the analog and digital voltage channels, additional hardware components connected via GPIB are controlled via timed software interrupts. This is done by using the callback functionality provided by DAQmx. The timing of the execution of these functions is not fixed, and varies by tens of ms, depending on the CPU load.

The modular structure of the code allows external python scripts to upload a ramp to the server, analyze the resulting absorption image and determine the next course of action. This feature was used to automatically detect slow drifts in the magnetic field and correct for it (see Sec. 4.4.1). In the future, this can be used to optimize the ramp using genetic algorithms[47].

Additional features such as the ability to queue a batch of ramps with variable parameters, logging the ramps and broadcasting the server status for other processes are also implemented.



Figure 3.20: Screen-shot of the GUI used to edit ramps. (a) The top row shows the key-frames and their time positions. The arrows indicate the parent-child relationship of the key-frames. The bottom three rows show three analog voltage channels. The values of these channels need not be defined at all key-frames. The software interpolates the values between the key-frames where the values are defined. The kind of interpolation can be specified for each segment. (b) Example of a complex key-frame structure. The key-frame “Take abs image” is a child of “Science stops”. Other key-frames related to taking an absorption image such as “Clean frame” and “Open abs shutter” are children of “Take abs image” with negative time. To change the total time of flight, one has to simply change the time value of “Take abs image” and the timing of the rest of the events is automatically adjusted.

After development of this software, we found that a very similar client-server architecture is used in other cold atom groups[48, 49]. This is not surprising given that the problems faced by other cold atom groups are the same. The Cicero Word Generator [48] developed at MIT has a host of useful features not implemented in rampage. Our software has the advantage of being completely cross-platform: The client has been tested on Windows, Linux and Mac. The server can in principle run on Linux since the National Instruments DAQmx is available for Linux, but has not been tested.

Rampage is open-source and is available for download from GitHub².

3.7.4 IP-BEC

IP-BEC (IP stands for image processing) is the software used for browsing and analyzing absorption images. Similar to rampage, it is GUI based, but all the image browsing, image processing and fitting subroutines are available as python modules which can be used for scripting. Some of the features implemented in the software include adding tags and comments to absorption images, fringe reduction using the eigen-face algorithm (see Sec. 3.4.10), correcting for saturation due to high probe intensity, fitting the 2D column density to various functions. Additional features are added via plugins, which themselves can be python modules so that they can be reused in external scripts. IP-BEC is available for download from GitHub³.

3.7.5 Photo Diode and Temperature monitors

Two LabJack U3-HV data acquisition devices are used to monitor and log laser beam powers and lab temperatures. Photodiodes pick off a small fraction of all MOT beams, optical pumping beam, push beam and tapered amplifier beam. The photodiodes are connected via BNC connectors to an electronics box which houses the LabJack. The box has circuitry to reverse bias the photodiodes at 5 V and read off the voltage across a $40\text{ k}\Omega$ load resistor connected in series with the photodiode. 12 photodiodes can be connected simultaneously. Additionally, 4 inputs with a $\pm 10\text{ V}$ range are available to monitor miscellaneous signals in the experiment.

The temperature monitor LabJack logs temperatures at the vacuum and spectroscopy side of the table, the temperature of the coils and of the water running through the coils, the temperature of the half nipple holding the Rubidium ampoule and the temperature of the lab ventilation and air-conditioner inlets.

3.8 Ramp to BEC

This section describes the experimental cycle starting from capturing atoms in a vapor cell MOT and ending with a Bose-Einstein condensate. The entire 25 s ramp is broken into four stages. The first three stages are common to all experiments performed on the BEC. In the final stage, depending on

²<https://github.com/shreyaspatnis/rampage>

³<https://github.com/shreyaspatnis/ipbec>

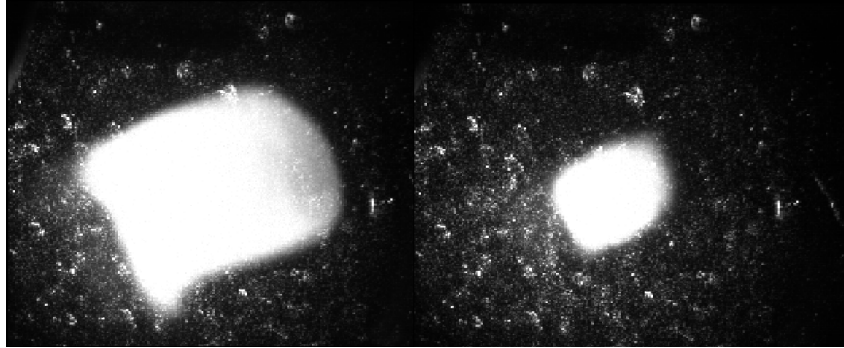


Figure 3.21: Lower MOT imaged on the side camera. The left picture shows a fully loaded MOT after 30 s of loading. The right picture shows a MOT after 5 s of loading, which is sufficient to achieve condensation.

the experiment being performed, the BEC is loaded in one of four different traps: the hybrid trap, crossed dipole trap, SLD trap and the ReST trap.

3.8.1 Stage 1: MOT loading

The lower MOT is loaded using a cold atom beam created by continuously outcoupling atoms from the upper MOT using a push beam. The MOT loading stage typically lasts for 2-6s, depending on how well the push beam alignment and power are optimized. A magnetic field gradient of $B'_z = 14 \text{ G/cm}$ is applied and the detuning of the trapping light is set to -18 MHz . The MOT is monitored on the side camera (see Fig. 3.21).

After loading, the MOT is compressed by ramping the magnetic field gradient to a final value of 20 G/cm in 6 ms . This final gradient is an estimate. In reality the control voltage to the current driver is set to a high value. Since the driver has a slow response time of 100 ms , the current in the coil rises by a small amount in the 6 ms . The optimal value of the control voltage is found by optimizing loading in the quadrupole trap. The detuning of the trapping beam is jumped to -26 MHz .

3.8.2 Stage 2: Molasses and Optical pumping

The compressed MOT stage is followed by a 6 ms molasses stage. The quadrupole field is switched off in 1 ms using the FETs. The trapping light power is jumped to 80% of its maximum value and then ramped down to zero in 6 ms . The trapping light detuning is jumped to -32 MHz . The temperature at the end of molasses is $80 \mu\text{K}$. This temperature is much higher than the $5\text{-}10 \mu\text{K}$ temperature that is typically achieved during molasses. We suspect it is due to re-scattering of the trapping light due to high atom density[50]. A MOT with 500M atoms, obtained by loading for a shorter time, has a temperature of $40 \mu\text{K}$.

After the molasses stage, the atoms are optically pumped to the $|F = 2, m_F = 2\rangle$ magnetically trappable state. This is done by setting a vertical bias field and shining the σ^+ polarized optical

pumping beam for 1.1 ms. The strength of the magnetic field during optical pumping is not constant since the current in the bias coils has not reached steady state in the short 1.1 ms duration. The control voltage applied to the driver corresponds to a steady state magnetic field of 5 G.

The repump beam is kept on to pump atoms from $F = 1$ to $F = 2$. The optical pump pulse duration, detuning, and power as well as the repump power are determined by maximizing the number of atoms loaded in the quadrupole trap. We typically use 3-4 mW of light in a beam with a waist of 8 mm and detuned 28 MHz above the $F = 2 \rightarrow 2$ transition.

3.8.3 Stage 3: Quadrupole Magnetic Trap

After the optical pumping stage, all light beams are switched off and the quadrupole trap with a field gradient of $B'_z = 120$ G/cm is turned on to magnetically trap the atoms. A mechanical shutter is used to block all the light to avoid heating due to light scattering. The RF signal used for evaporative cooling is turned on and set to 29 MHz for 400 ms as the trapped cloud equilibrates. At this point there are 2.5-3.0B atoms in the trap at a temperature of $400\text{ }\mu\text{K}$. The lifetime of the atoms in the quadrupole trap is 140 s.

After the initial hold, the RF frequency is swept linearly from 29 MHz to 3 MHz in 9.6 s. At the end of the evaporation cycle, 100-110M atoms at a temperature of $33\text{ }\mu\text{K}$ are left. The truncation parameter, defined as $\eta = 2h\nu/kT$, where ν is the frequency of the RF knife, goes from $\eta = 7.0$ at the beginning of the ramp to $\eta = 8.8$ towards the end. Near the end of evaporation, Majorana losses due to spin flips at the center of the magnetic trap start to dominate trap loss and evaporation is inefficient, since colder atoms are lost from the center of the trap. The lifetime of the atoms at the end of RF-evaporation is 11 s. At this point, we transfer atoms from the quadrupole trap to the hybrid trap.

3.8.4 Stage 4: Hybrid Trap

The power in the hybrid trap is ramped up linearly during the RF evaporation stage, to a maximum power of ~ 5 W. This corresponds to a trap depth of $\sim 65\text{ }\mu\text{K}$. After RF evaporation, the atoms are transferred to the hybrid trap in two steps. In the first step, the magnetic field gradient is linearly ramped from 120 G/cm to 80 G/cm in 1 s, while the RF knife is ramped from 3 MHz to 2 MHz. In the second stage, the field gradient is further ramped down to 30 G/cm, while the RF knife is switched off. $B_z = 30.4$ G/cm, which corresponds to a vertical field gradient $B_y = B_z/2 = 15.2$ G/cm cancels gravity. Hence lowering the field gradient beyond this value causes the atoms to adiabatically transfer from the magnetic field center to the hybrid trap beam center. The position of the hybrid trap beam is optimized to maximize the transfer efficiency. The optimal point is found to be 150 μm below the center of the magnetic trap. After the transfer, we are left with 20M atoms at $10\text{ }\mu\text{K}$.

Further evaporation is done by both decreasing the the hybrid trap beam power and the magnetic field gradient. Reducing the magnetic field gradient creates a tilted potential due to gravity and reduces the effective trap depth. This is again done in two stages. In the first stage, the hybrid trap

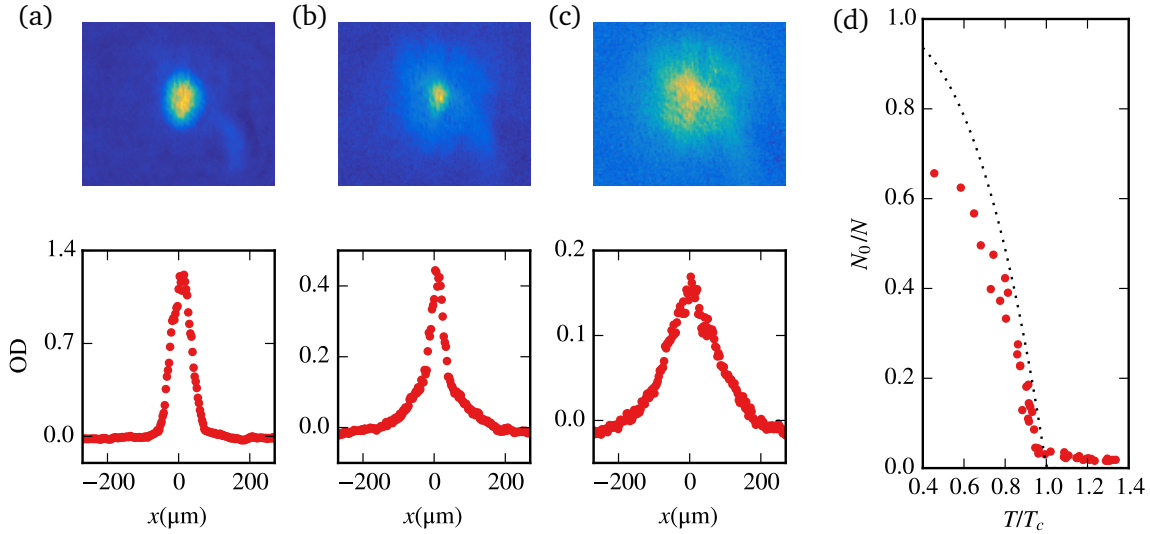


Figure 3.22: Crossing the critical temperature by heating a pure condensate. (a) A pure condensate produced in the hybrid trap with a high trap depth of 9.5 μK . (b) With time, the cloud develops a thermal fraction as it heats up, until (c) it is completely thermal. (d) Condensed fraction as a function of the temperature of the cloud. Dotted black line is the prediction for an ideal Bose gas in the Thermodynamic limit.

beam power is reduced from 5 W to 400 mW in 4.5 s. An exponential ramp with a time constant of 1.1 s is used for this ramp. At the same time, the magnetic field gradient is ramped down from 30 G/cm to 24 G/cm using an exponential ramp with a time constant of 1.8 s. At this point the trap depth is 3.3 μK and the cloud is partially condensed. To get a pure BEC in the hybrid trap, the beam power is lowered to 300 mW in 1.9 s, corresponding to a final trap depth of 2.2 μK . We typically produce pure condensates with 700k to 1M atoms.

Bose-Einstein condensation is characterized by a discontinuous rise in the condensed fraction as the cloud is cooled below a critical temperature T_c . For an ideal Bose gas in a harmonic trap, the transition temperature is given by

$$T_c^0 = \frac{\hbar\bar{\omega}}{k_B} \left(\frac{N}{g_3(1)} \right)^{1/3} \quad (3.13)$$

and the condensed fraction is given by $N_0/N = 1 - (T/T_c)^3$ [51]. The transition temperature T_c depends on the number of atoms. Thus, comparing the measured transition temperature with the theoretically predicted value serves as a verification that our atom number calibration is correct[52].

During evaporation in the hybrid trap, the trapping frequency is not constant but decreases with the trap depth, making it difficult to evaluate the critical temperature. To overcome this, we observe the transition through the critical temperature in a somewhat different way than the traditional method of measuring the temperature at different times during evaporation. First, we create a pure BEC with negligible thermal fraction in the hybrid trap. Subsequently, we adiabatically ramp up the

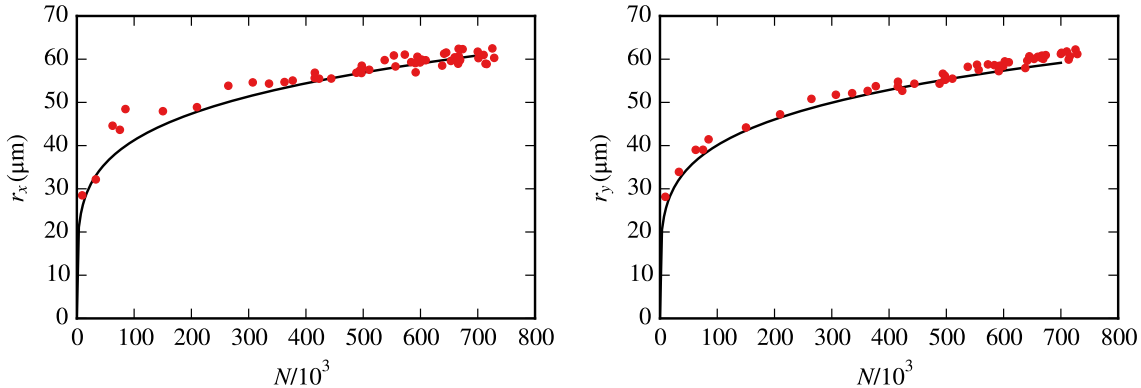


Figure 3.23: Thomas-Fermi radius of a condensate after time of flight as a function of atom number. Solid line is a prediction using the scaling solution.

the hybrid trap beam power to 650 mW and the magnetic field gradient to 30 G/cm in 1 s to get a final trap depth of 9.5 \$\mu\text{K}\$. We then hold the condensate in the trap for a variable amount of time from 0-3.5s. Heating due to the hybrid trap beam shrinks the condensed fraction while the thermal fraction grows until the cloud is purely thermal (see Fig. 3.22). The condensate fraction \$N_0/N\$ and the temperature of the cloud are determined by following a fitting procedure outlined in Ref. [53]. This fitting was performed by Ramon Ramos.

Fig. 3.22(d) shows the condensed fraction as a function of temperature of the cloud. The measured critical temperature is 5% less than the prediction for an ideal gas. A small reduction is expected due to inter-atomic interactions which decrease the density of the condensed atoms [54, 55]. The fractional correction, given by

$$\frac{\delta T_c}{T_c} = -1.33 \left(\frac{a}{a_{ho}} \right) N^{1/6}, \quad (3.14)$$

reduces the expected transition temperature by 7% for our trap parameters. The remaining 2% discrepancy could be due to an error in measuring the trap frequency (2%) or due to incorrect atom number calibration. Since \$T_c \propto N^{1/3}\$, the atom number calibration is accurate to within 6%.

In addition to the transition temperature, we studied ground state properties of a zero temperature condensate. In particular, we measured the Thomas-Fermi radius of a condensate after time of flight and compared it to the scaling solution[25]. Fig. 3.23 shows the fitted Thomas-Fermi radius of a cloud released from an trap with frequencies \$(\omega_x, \omega_y, \omega_z) = 2\pi \times (40, 37, 42)\$ Hz after 20 ms of time-of-flight. The scaling solution is calculated numerically using the experimentally measured trap frequencies and agrees reasonably well with data.

3.8.5 Stage 4: Crossed Dipole Trap

Purely optical traps have the advantage of trapping all the magnetic ground state levels, as opposed to only the weak field seeking states. We transfer our atoms from the hybrid trap to the crossed dipole trap to interrogate the atoms with RF fields in the presence of a constant magnetic field (see Sec. 4.4).

The ramp to BEC proceeds the same way until the transfer to the hybrid trap. After the transfer, we simultaneously decrease the power in the hybrid trap beam, decrease the magnetic field gradient and ramp up the power in the cross dipole trap beam in 4.3 s. The hybrid trap power is ramped down to 0.7 W with an exponential ramp with a time constant of 1.1 s. The magnetic field gradient is ramped down to 7.0 G/cm exponentially with a time constant of 1.8 s and the cross-dipole trap beam is ramped up linearly to ~ 0.2 W.

In a second stage, the magnetic field gradient is ramped down to 0 G/cm in 900 ms and the crossed dipole trap beam is ramped down to 150 mW to get a pure BEC with 200k-400k atoms.

3.8.6 Stage 4: SLD Trap

The Superluminescent diode trap provides a waveguide with a tight transverse confinement of 230 Hz (see Fig. 3.12(b)) suitable for the dwell time and tunneling time experiments. After the first stage of hybrid trap evaporation described in Sec 3.8.4, the power in the SLD trap beam and the crossed dipole trap beam is ramped up in 100 ms to 90 mW and ~ 0.2 W respectively. The SLD power is measured right after the control AOM and the power at the atoms is $\sim 55\%$ of this. After the ramp up, the hybrid trap power and the magnetic field gradient are ramped down to 0 in 2 s to transfer the cloud to the SLD trap. The SLD beam power is ramped down to 70 mW in the same interval to reduce the trap depth and get a pure BEC with 60-80k atoms.

3.8.7 Stage 4: ReST Trap

The Repulsive Sheet Trap (ReST) is formed by a combination of a magnetic field gradient and a thin barrier sheet and is used to study tunneling of a BEC out of a quasi bound state. Details of the trap, loading procedure, and ground state properties may be found in Chapter 5.

3.9 Outlook

This chapter describes the upgrades and additions made to the setup over the past five years. Continuing the quest for a reliable BEC machine, the optical layout for the light generation was compacted to reduce path lengths and beam drifts. The upper MOT optics were modularized and a stable anti-Helmholtz coil mount was built. These upgrades markedly increased the stability of the machine and allowed for continuous data runs for more than 36 hours, in addition to reducing the number of knobs that needed to be tweaked daily to get a BEC.

Significant progress was made towards measuring the tunneling time with the addition of the second generation barrier beam, Raman coupling beams at the magic-zero wavelength and a smooth waveguide generated by a Superluminescent diode beam.

On the software side, a powerful and customizable system to generate and execute control ramps was developed. The GUI is used for quick changes to the ramp, while the modular structure of the software allows external python scripts to upload and run ramps and analyze the resulting absorption images. This paves the way for automating the optimization of the ramp to BEC, a task which is quite tedious to be carried out manually.

Chapter 4

Progress Towards Measuring the Tunneling Time

In this chapter I will describe our progress towards measuring the tunneling time of a particle, which is the main long term goal of our experiment. After a brief introduction on the subject, I will present a detailed analysis of the experimental requirements. This is followed by a description of the experimental methods developed to meet these requirements.

4.1 Introduction and Motivation

Quantum tunneling, a phenomenon where a particle traverses a barrier region which classically it cannot surmount, is one of the many striking features of quantum mechanics. While quantum mechanics successfully gives the rate of tunneling of particles, the seemingly simple question of the time it takes to tunnel through a barrier, to date, lacks a resolute answer. This is fundamentally due to a lack of well defined trajectories in space-time for quantum particles[56]. The trajectory $x(t)$ of a classical particle can be used to unambiguously determine the time when it enters and exits a given region. This is not the case for quantum particles, which are waves. The problem is more severe in the case of tunneling since the wavefunction is evanescent inside the forbidden region and the momentum inside the forbidden region is not well defined. Lacking an unambiguous definition, researchers have resorted to operational definitions based on thought experiments that measure a time. A review of these definitions and the scope of their validity can be found in Refs. [20, 57]. The thought experiments can be categorized broadly into two classes: those measuring the arrival time or delay due to tunneling and those which measure the barrier interaction time[58].

Arrival time experiments measure the time delay in the arrival of a tunneled particle as compared to a particle traveling in free space. When the delay is measured with respect to the peak of the wavepackets, this measurement yields the Wigner time[59], also called the group delay. It was pointed out that the Wigner time saturates with the thickness of the barrier region[60], which would imply superluminal propagation for sufficiently thick barriers. Superluminal arrival times have been

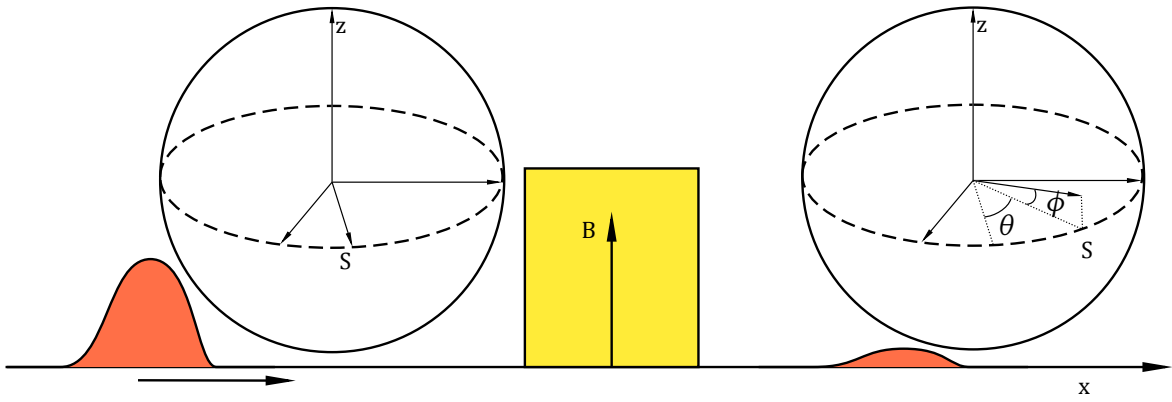


Figure 4.1: The Larmor clock thought experiment. A spin 1/2 particle precesses under the influence of a magnetic field confined in the barrier region. The spin of the incident and the tunneled particles is depicted on the Bloch sphere.

reported in many systems, for example with single photons[61] and femtosecond pulses tunneling through a photonic band gaps[62] and surface evanescent microwaves[63]. A zero delay time due to tunneling is reported for electrons undergoing tunnel ionization[64, 65]. The superluminal arrival might seem surprising at first; however, it was shown that the peak of the incident and tunneled particles need not have a causal relationship[66]. For the same reason, the group delay also need not correspond to the time spent inside the barrier region[57].

The second class of thought experiments attempt to measure the time spent inside the barrier region, either by modulating the barrier[66], or invoking a clock that “ticks” only when the particle is inside the barrier region[67]. Barrier modulation results in generating sidebands in the transmission amplitude, and Büttiker and Landauer argued that the sideband asymmetry can be used to measure the barrier interaction time[66]. The intuitive picture is that if the modulation frequency ω is small compared to the barrier interaction time, i.e. $\omega \ll 1/\tau$, then the transmission amplitude essentially follows the modulation. As ω is cranked up, a tunneling particle sees multiple barrier oscillations within the interaction time and the transmission amplitude no longer adiabatically follows the modulation. Although the transition between these two regimes is smooth, there is a time scale associated with it. This time is called the Büttiker-Landauer time, or the semi-classical time, since in the opaque barrier limit, it is proportional to the width of the barrier.

The clock approach is best illustrated with the classic Larmor time thought experiment[67–69]. As shown in Fig. 4.1, a spin 1/2 particle with its spin initially in the $x - y$ plane is incident upon a barrier. A small magnetic field along z is applied inside the barrier region, which causes the spin to precess as the particle traverses the barrier. The time spent inside the barrier can now be read off from the precession angle θ : $\tau = \theta/\omega_l$, where $\omega_l = \mu B/\hbar$ is the Larmor frequency. While the clock approach is quite elegant, Büttiker realized that in addition to the in-plane precession θ , there is a tendency of the spin to align with the magnetic field[67]. This is because the interaction with the magnetic field lowers the energy of spins pointing along the magnetic field, hence increasing their

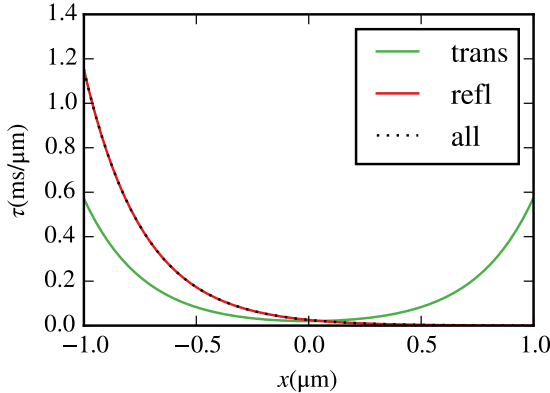


Figure 4.2: Conditional probabilities for ^{87}Rb atoms tunneling through a $2\text{ }\mu\text{m}$ square barrier. The barrier height is 50 nK and the particles are incident from the left with an energy of 40 nK .

transmission probability. The out of plane rotation angle ϕ introduces another timescale $\tau_z = \phi / \omega_l$ and its interpretation is not immediately clear.

It is straightforward to show that the Larmor clock thought experiment measures the dwell time of a particle, conditioned on the particle being transmitted. The dwell time, first introduced by Smith[70], is just the probability of finding the particle in a particular region, integrated over all times:

$$\tau_d = \int_{-\infty}^{\infty} dt \int_{x_a}^{x_b} dx |\psi(x, t)|^2. \quad (4.1)$$

Here x_a and x_b are the boundaries of the region of interest and ψ is the wavefunction. While the dwell time gives us the expectation value of the time spent in a particular region, it fails to distinguish between transmitted and reflected subensembles. The weak measurement formalism, as first introduced by Aharonov, Albert and Vaidman (AAV)[71], naturally allows for addressing such subensembles. The interpretation of the two time scales associated with the in-plane and out-of-plane rotation is apparent when the Larmor clock thought experiment is recast in the language of weak measurements[56].

The weak value of an observable \hat{A} , for a particle initially prepared in state $|i\rangle$ and later found in the state $|f\rangle$ is given by

$$\langle A \rangle_w = \frac{\langle f | A | i \rangle}{\langle f | i \rangle} \quad (4.2)$$

The dwell time formula in Eq. 4.4 can be written as the time integral of the expectation value of the projector

$$\Theta_B = \int_{x_a}^{x_b} dx |x\rangle \langle x|, \quad (4.3)$$

which gives

$$\tau_d = \int_{-\infty}^{\infty} dt \langle \psi | \Theta_B | \psi \rangle. \quad (4.4)$$

If ψ is an eigenstate of the Hamiltonian and is unbounded, then it is not normalizable. In such cases, the amplitude of the incident wavefunction is chosen to be 1 and the dwell time is given by the expectation value of Θ_B divided by the incident flux:

$$\tau_d = \frac{m}{\hbar k} \langle \psi | \Theta_B | \psi \rangle. \quad (4.5)$$

As mentioned earlier, the dwell time does not distinguish between particles which are transmitted or reflected. Following AAV, we can imagine a weak von Neumann measurement of the projector Θ_B . The tunneling time τ_t is the time measured when the particle was initially in the state $|i\rangle$ and was later transmitted and found in the state $|t\rangle$:

$$\tau_t = \frac{m}{\hbar k} \frac{\langle t | \Theta_B | i \rangle}{\langle t | i \rangle}. \quad (4.6)$$

The reflection time τ_r can be obtained by replacing $|t\rangle$ with the reflected wavefunction $|r\rangle$. The weak value in Eq. 4.6 can be complex. However, the interpretation of the complex part of the weak value is clear. The real part of the weak value corresponds to the shift of the pointer position, whereas the complex value results in a shift of the momentum of the pointer, which is a result of the backaction of the measurement on the particle. Going back to the Larmor time experiment, the real part of the weak value is related to the in-plane rotation, whereas the imaginary value is related to the out-of-plane rotation[56].

Further insight can be obtained by extending the Larmor clock thought experiment to probe where inside the barrier region a particle spends time[21]. The “clock” is now localized in a small region within the barrier and probes the time spent only in that region. As with the previous case, the measured dwell time can be conditioned on the particle being transmitted or reflected. Such a calculation reveals an astonishing result for the transmitted particles. Fig. 4.2 shows the conditional dwell time for a particle tunneling through a square barrier. We see that while the reflected particles spend most of the time close to the entrance of the tunnel barrier, the situation is quite different for the transmitted particles. The transmitted particles spend equal time at the entrance and exit face of the barrier, but negligible time in the center of the barrier.

This surprising result can be intuitively understood from the symmetric nature of the weak value with respect to the pre- and post-selected states[72]. The initial state of the particle is a wavepacket on the left of the barrier at early times and is traveling towards the barrier. The incident wavepacket decays exponentially after penetrating the entrance face of the barrier. On the other hand, a transmitted particle is found to be on the right of the barrier at late times. Propagating the transmitted wavepacket back in time, we find that it decays exponentially inside the barrier while penetrating through the *exit* face. The weak value is a product of the incident and transmitted wavefunctions and is symmetric around the barrier.

The principal goal of our experiment is to verify the prediction that the tunneled particles spend equal time at the entrance and exit faces of the barrier and an exponentially small time in the center. The reflected particles, on the other hand, penetrate only the entrance face of the barrier. We

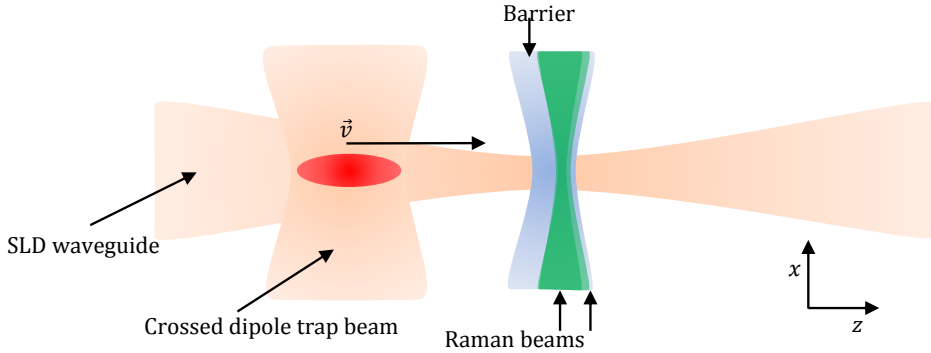


Figure 4.3: Experimental scheme for measuring the tunneling time.

also wish to investigate the connection between the various proposed tunneling times. In particular, Büttiker-Landauer time is related to the imaginary components of the conditional dwell times. Further details about the motivation of these experiments may be found in Refs.[73, 74].

4.2 Experimental considerations

This section provides a detailed analysis of the experimental requirements to study the tunneling time of a ^{87}Rb Bose-Einstein condensate. A schematic for the envisioned experimental scheme is shown in Fig. 4.3. A waveguide created using far off resonant light (see Sec. 3.5.2) confines the BEC in two dimensions, so that the dynamics of a condensate released in the waveguide are effectively one dimensional. The tunnel barrier is formed by intersecting the waveguide with a second, tightly focused beam. This beam is blue-detuned to the atomic resonance, and creates a repulsive potential (see. Sec. 3.5.3). The Larmor clock is implemented by focusing a pair of Raman beams inside the tunnel barrier. The Raman beams are tuned to a two photon resonance and cause the atomic spin to precess as the BEC traverses the Raman beams. After interacting with the barrier, the transmitted and reflected portions of the condensate can be imaged using absorption imaging. A Stern-Gerlach sequence applied before imaging is used to detect the population in each spin state.

This experimental sequence realizes tunneling in a scattering configuration, i.e. tunneling from one unbound state into another. Tunneling in scattering configuration is more challenging to realize than tunneling out of a bound state, or tunneling between two bound states. In a bound state the particle bounces back and forth in the trapping well and has multiple chances to tunnel out. Hence a significant tunneling rate can be measured even though the probability of tunneling per round trip time is low. In a scattering configuration, the wavepacket has only one chance to tunnel and the tunneling probability has to be high.

We wish to maximize the probability of tunneling and be in a regime where we can detect the tunneled fraction in a single shot. Using current absorption techniques we can reliably detect a cloud with around 500 atoms (see Sec. 3.4.10). Starting with a cloud of 50k atoms, we would need a

tunneling probability of a few percent to be able to detect any tunneling. We could start with a higher atom number; however, the higher spread in energy due to interactions makes it difficult to differentiate between classical transmission and tunneling.

Below, we will determine the optimal configuration for carrying out the tunneling experiments. Various factors have to be considered and optimizing for one almost always worsens something else, making it important to settle with the right trade off. These factors, and the associated trade offs, are listed briefly before delving into the details:

- **Barrier width:** Perhaps the most critical parameter, reducing the barrier width exponentially increases the probability of tunneling. Since the barrier is made optically by focusing a laser beam, the trade off is that a tightly focused beam diverges faster. The diverging beam constrains the transverse size of the cloud to be less than the Rayleigh range z_R of the barrier beam.
- **Transverse Size:** Reducing the transverse size of the wavepacket ensures that it tunnels through the thinnest part of the barrier. However, it also increases the density of the wavepacket and hence the longitudinal spread in velocity.
- **Longitudinal velocity spread:** When the BEC is released in the waveguide by switching off the longitudinal confinement, the mean field energy of the atoms is converted into kinetic energy, thus creating a large spread in longitudinal velocity. This makes it harder to clearly differentiate between tunneling and classical transmission. The mean field energy is density dependent and increases with increasing the transverse confinement and the number of atoms.
- **Number of atoms** Increasing the number of atoms increases the signal to noise ratio when detecting tunneled atoms. However, it also increases the longitudinal velocity spread.
- **Width of the Raman beams:** In order to measure the tunneling time, the Raman beams have to localized to at least within the forbidden region. In the long run, we wish to probe the time spent in different parts inside the barrier, which would require the Raman beams to be focused much tighter than the barrier beam.
- **Precision of the Larmor clock:** The Larmor clock measures the time spent in a given region. We would like the clock to be precise enough to reliably measure the dip in the conditional dwell time inside the barrier region.

4.2.1 Barrier width

The tunnel barrier in our experiment is created optically by focusing a far blue-detuned sheet of light to a waist $w_0 = 1.3 \mu\text{m}$. (see Sec. 3.5.3). It has a Rayleigh range of $z_R = 8 \mu\text{m}$. The beam waist is limited by residual spherical aberrations in the focusing system. The waist of the barrier beam sets an upper limit on the longitudinal velocity spread and the Rayleigh range sets an upper limit on the transverse size, as seen in the next two sections.

4.2.2 Longitudinal velocity spread

To evaluate the required longitudinal velocity spread, we first look at the tunneling properties through a Gaussian barrier. Consider a potential of the form

$$U(x) = U_0 \exp(-2x^2/w^2) \quad (4.7)$$

and a particle with a kinetic energy E incident upon it. When $E < U_0$ the particle tunnels through the barrier and has an exponentially decaying wavefunction inside the forbidden region. The full width of this forbidden region w_f is not a constant, like in the case of a square barrier. It depends on the incident energy as

$$w_f = w \sqrt{-2 \log(E/U_0)}. \quad (4.8)$$

w_f decreases as the incident energy is closer to the barrier height. For the tunneling time experiments, we are interested in probing the wavefunction in the forbidden region. In order to be able to localize the Raman probe within this region, we would like to make it as large as possible by keeping the incident energy low. This contradicts the need to keep the transmission probability high which requires the incident energy to be close to the barrier height. We will show that the solution is to work at very low barrier height U_0 . Note that the w_f depends only on the ratio E/U_0 .

The transmission probability through a Gaussian barrier does not have an analytical expression and has to be calculated numerically. An approximate WKB solution works well as long as E is not too close to U_0 . It gives some insight on the dependence of the transmission probability on different parameters and is worth deriving.

The WKB formula for transmission probability T through a Gaussian barrier is given by[75]

$$\log T = -2 \int_{x_1}^{x_2} \frac{\{2m(U(x)-E)\}^{1/2}}{\hbar} dx. \quad (4.9)$$

Here x_1 and x_2 are positions of the classical turning points:

$$x_2 = -x_1 = w \sqrt{\log(U_0/E)/2}. \quad (4.10)$$

Defining non-dimensional quantities $t = x/w$ and $s = E/U_0$ and using Eq. 4.7, Eq. 4.9 becomes

$$\log T = -\frac{2w\sqrt{2mU_0}}{\hbar} \mathcal{S}(E/U_0), \quad (4.11)$$

where $\mathcal{S}(s)$ is the dimensionless action, given by

$$\mathcal{S}(s) = 2 \int_0^{\sqrt{-\log(s)/2}} [\exp(-2t^2) - s]^{1/2} dt. \quad (4.12)$$

From Eq. 4.11, we see that for a fixed ratio of E/U_0 , and hence for a fixed forbidden region width

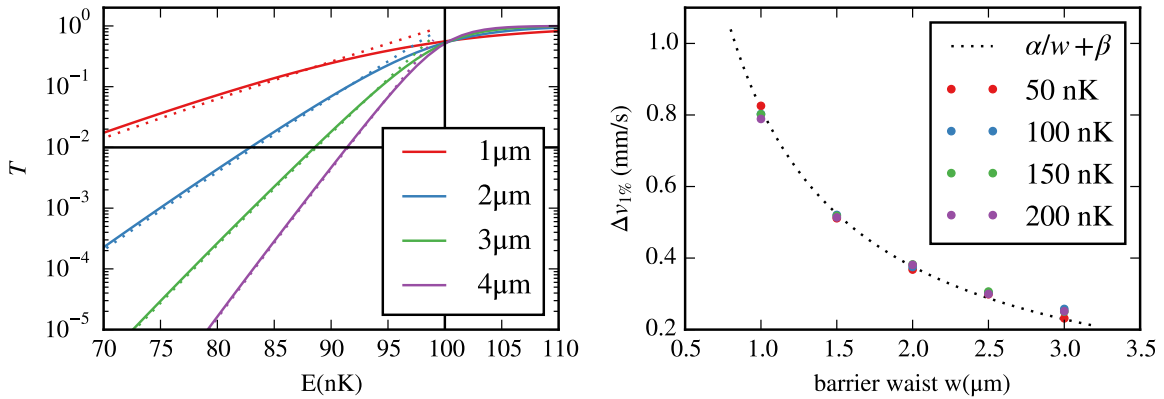


Figure 4.4: Transmission probability through a Gaussian barrier. (a) Solid lines show transmission probability through a $k_B \times 100$ nK Gaussian barrier with a waist of 1 μm -4 μm . Dotted lines are a WKB approximation. Black horizontal line indicates 1% transmission probability. (b) The 1% velocity window as a function of the barrier waist for different barrier heights. The velocity window depends mostly on the width of the barrier and very weakly on the barrier height. Fitting the 50 nK data to the function $\Delta v = \alpha/w + \beta$ (dotted line) gives $\alpha = 0.88$ (mm/s)(μm) and $\beta = -6.6 \times 10^{-2}$ mm/s

w_f (Eq. 4.8), the transmission probability goes down with increasing barrier height U_0 . Thus, the barrier height U_0 should be kept as low as possible. In the experiment, the incident wavepacket is not monochromatic and has a spread in energy ΔE . In order to clearly differentiate between tunneling and classical transmission, U_0 cannot be reduced to less than ΔE , the spread in energy of the incident wavepacket.

For a cloud of atoms initially prepared in the ground state of a trap and then accelerated towards the barrier, it is more convenient to use the rms spread in velocity Δv , rather than the spread in energy ΔE . This is because Δv is constant when accelerating the wavepacket, whereas the energy spread $\Delta E \sim 2\sqrt{E\Delta E_0}$ increases.

The tunneling probability is significant only for a small range of incident energies close to U_0 . We define a velocity window $\Delta v_{1\%}$ as the range of velocities for which the tunneling probability is greater than 1%. The experimental goal is to reduce the velocity spread of the incident wavepacket to less than $\Delta v_{1\%}$ so as to maximize the tunneling probability. Fig. 4.4(b) plots the 1% window as a function of the waist of the barrier for barrier heights ranging from 50 nK to 200 nK. Interestingly, this width depends very weakly on the height of the barrier. This is a peculiar feature of the Gaussian barrier and is due to the width of the forbidden region decreasing with increasing velocity. Intuitively, one would expect the velocity window Δv to be such that the de Broglie wavelength $\hbar/m\Delta v$ is comparable to the barrier waist w . Indeed, the data in 4.4(b) fits well to the function $\Delta v = \alpha/w + \beta$. The extracted fit parameter $\alpha = 0.88$ (mm/s)(μm) is surprisingly close to the naively expected value of $\hbar/m = 0.73$ (mm/s)(μm).

The waist of the second generation barrier is 1.3 μm (see Sec. 3.5.3) which places the veloc-

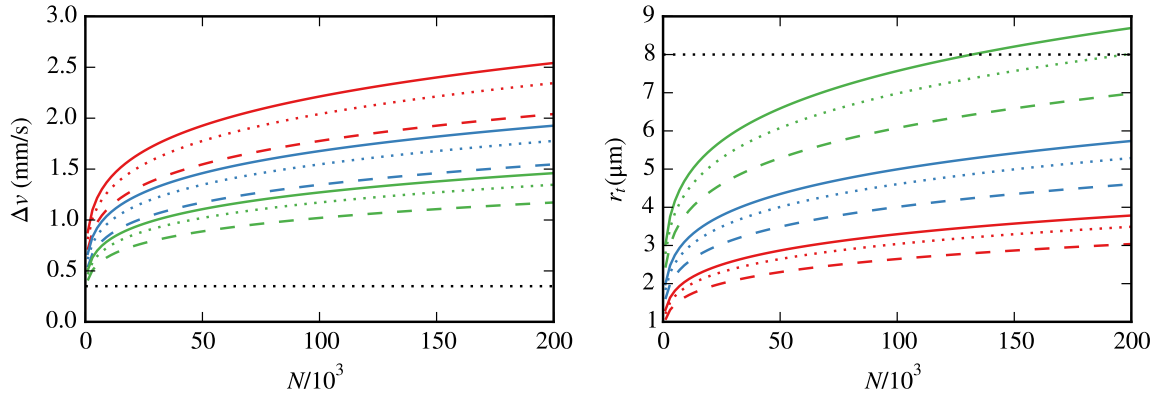


Figure 4.5: Longitudinal velocity spread Δv and transverse radius r_t as a function of number of atoms N . Red, blue and green curves correspond to a transverse frequency of 200 Hz, 100 Hz and 50 Hz respectively. Solid, dotted and dashed lines correspond to a longitudinal trapping frequency of 30 Hz, 20 Hz and 10 Hz respectively. Horizontal dotted black lines indicate the maximum allowed velocity spread and transverse radius for a $1.1 \mu\text{m}$ barrier (see Eq. 4.14 and Eq. 4.15)

ity window $\Delta v_{1\%}$ at 0.6 mm/s . Since this is the full width of the window, the rms spread in the longitudinal velocity should be less by a factor of 2, giving us

$$\Delta v < \Delta v_{\max} = 0.3 \text{ mm/s}. \quad (4.13)$$

In general, for a barrier waist w ,

$$\Delta v < (\alpha/w + \beta)/2 = (0.44/w [\mu\text{m}] - 0.03) \text{ mm/s} \quad (4.14)$$

Ideally, we would like $\Delta v \ll \Delta v_{\max}$; however, for typical trap parameters $\Delta v \sim 1 \text{ mm/s}$.

4.2.3 Transverse size

The diverging barrier beam limits the transverse size of the condensate to less than z_R . Let $r_t = r_s z_R$ be the transverse radius of the condensate. r_s is a dimensionless scaling factor. Using Eq. 2.7 for the Thomas-Fermi radius in a harmonic trap, we get an additional constraint

$$r_s^2 = \frac{2\mu}{mz_R^2\omega_t^2} < 1. \quad (4.15)$$

Here μ is the chemical potential and ω_t is the transverse trapping frequency.

4.2.4 Number of atoms

The chemical potential scales weakly with the number of atoms: $\mu \propto N^{2/5}$ (see Eq. 2.6). Both Δv and r_t , which are proportional to $\sqrt{\mu}$ scale as $N^{1/6}$. For typical atom number in the range of 20-

100k, the velocity spread does not change significantly. The reduction in velocity spread by reducing atom number does not justify the hit taken on signal to noise due to very few tunneled atoms.

Fig. 4.5 summarizes the results of this section. We see that the transverse radius can be kept a factor of 2 less than the Rayleigh range for a trapping frequency of 200 Hz. However, Δv is greater than Δv_{\max} for all trap geometries. Hence additional cooling or momentum filtering is required after preparing the condensate for the tunneling time experiment to be feasible. Attempts to reduce the momentum spread are discussed in Sec. 4.3.

A similar analysis can be found in Rockson Chang's thesis (Sec 5.2 in [29]). An important difference is consideration of the transverse size of the condensate here. We realized its importance while studying the tunneling of the condensate out of a bound state. The tunneling happened predominantly off focus where the barrier height is lower, but the width is higher.

In summary, given our tunnel barrier, the ideal parameters to study tunneling are $\omega_t = 2\pi \times 200\text{Hz}$, $\omega_l = 2\pi \times 10 - 30\text{Hz}$ and $N = 50\text{k} - 100\text{k}$. The SLD beam trap is designed to allow us to be in this regime (see Sec. 3.5.2). Additional cooling to reduce the velocity spread by $\sim 4x$ is required. We have demonstrated cooling by a factor of $2.4x$ in a magnetic waveguide (see Sec. 4.3).

4.2.5 Width of the Raman beams

The width of the Raman beams affects the spatial resolution with which we can measure the conditional dwell time. Fig. 4.6 shows the conditional dwell time for the tunneled particles as a function of the position inside the barrier region. The characteristic feature we would like to measure is a dip in the conditional dwell time inside the tunnel barrier. The dwell time inside the barrier region decays exponentially over a length scale $1/2\kappa$, where κ is the imaginary wave-vector inside the forbidden region. Thus, in order to resolve the dip, the waist of the Raman beams has to be less than $w_0 - 1/2\kappa$. Reducing κ so that the wavefunction decays faster inside the barrier region would help, but at the expense of exponentially decreasing the transmission probability. From Fig. 4.6(b), we see that the waist of the Raman beams has to be $0.5\text{ }\mu\text{m}$ or less. This condition can be relaxed if the Barrier beam was wider, which is possible if the velocity spread is reduced even further.

The first generation Larmor clock uses Raman beams at the 790 nm magic-zero wavelength and cannot be focused to the required waist using our current optics. The planned second generation clock would use blue light at the 421 nm magic-zero wavelength[44]. The shorter wavelength would allow for a smaller diffraction limited waist for the same numerical aperture.

4.2.6 Precision of the Larmor clock

Consider a particle with two internal ground states $|a\rangle$ and $|b\rangle$ interacting with a pair of Raman beams. It is initially prepared in the state $|a\rangle$ and has a velocity v . As it traverses through a region where the Raman beams are focused, its internal state will undergo a rotation. The internal state after the interaction can be written as $|\psi\rangle = \cos \theta |a\rangle + \sin \theta |b\rangle$. If the Raman beams are on two-

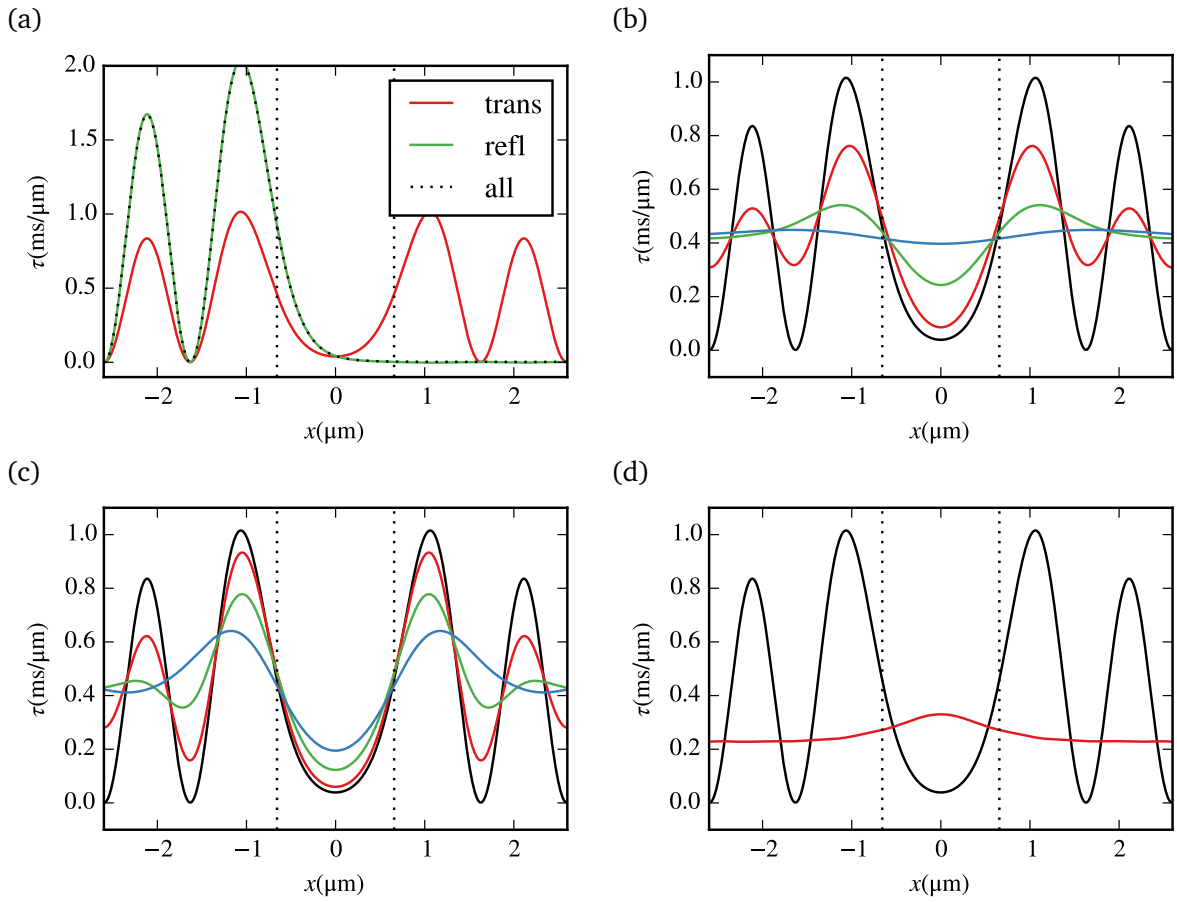


Figure 4.6: Conditional dwell times for ^{87}Rb atoms tunneling through a Gaussian barrier with a 50 nK height and a waist of 1.3 μm . The incident energy is 30 nK and the transmission probability is 1.5%. Vertical lines indicate the position of the classical turning points. (a) Conditional dwell time for the transmitted particles (red) and reflected particles (green). Black dotted line is the unconditioned dwell time. (b) The effect of the finite width of the Raman beams is calculated by convolving the conditional dwell time with the width of the Raman beams. These are calculated for Gaussian Raman beams with a waist of 0.5 μm (red), 1.0 μm (green) and 2.0 μm (blue). (c) Effect of the finite velocity spread of the atoms. Black line is for a monochromatic beam. The effect of a finite spread is calculated for an rms velocity spread of 0.2 mm/s (red), 0.4 mm/s (green) and 0.8 mm/s (blue). (d) Comparison of dwell times of tunneling particles (black) (30 nK energy) and classically transmitted particles (red) (100 nK energy). The barrier height is 50 nK. A classically transmitted particle slows down as it climbs a repulsive barrier and spends more time in the barrier region, where as a tunneled particle jumps from the entrance face to the exit face while spending very little time in the center.

photon resonance, the rotation angle θ is given by

$$\theta = \int \Omega_{2\nu}(t) dt \quad (4.16)$$

where $\Omega_{2\nu}$ is the two photon Rabi frequency. Since this is a two photon transition, $\Omega_{2\nu}$ is proportional to the intensity of the Raman beams[76]. For perfectly overlapping Raman beams with a Gaussian beam profile of waist w , $\Omega_{2\nu}$ has a spatial profile given by

$$\Omega_{2\nu}(x) = \Omega_0 e^{-\frac{2x^2}{w^2}}. \quad (4.17)$$

A particle traversing the Raman experiences a time dependent Rabi frequency $\Omega_{2\nu}(\nu t)$ and the rotation angle θ is given by

$$\theta = \int \Omega(\nu t) dt = \sqrt{\frac{\pi}{2}} \Omega_0 \left(\frac{w}{\nu} \right) \quad (4.18)$$

For the tunneling time measurement to be weak, $\theta \ll 1$, which gives us the condition

$$\Omega_0 \ll \sqrt{\frac{2}{\pi}} \left(\frac{\nu}{w} \right). \quad (4.19)$$

For a $1 \mu\text{m}$ waist and an incident energy of 50 nK , this gives us $\Omega_0 \ll 2\pi \times 400 \text{ Hz}$.

The above analysis started with the assumption that the two photon resonance condition is met. As a first requirement, we want the fluctuations in the two-photon detuning to be much less than the Rabi frequency for a precise clock. If the two states are Zeeman sublevels, then the two photon resonance condition is determined by the external magnetic field. This requires the magnetic field to be stable to much better than 0.5 mG .

4.3 Delta-kick cooling

In Sec. 4.2, we saw that the longitudinal velocity spread Δv of the condensate expanding in the waveguide is always larger than the maximum allowed spread to reliably distinguish between classical transmission and tunneling. This velocity spread, caused by the interaction energy of the condensate, can be reduced by decompressing the trap, which reduces the density of the cloud. However, the transverse frequency has to be high enough to keep the transverse extent of the cloud less than the Rayleigh range of the barrier beam. One could adiabatically decrease the longitudinal trapping frequency ω_l , which is around $2\pi \times 10 - 15 \text{ Hz}$ at the end of the evaporation cycle. The criteria for adiabaticity would be

$$\frac{d\omega_l}{dt} = -k\omega_l^2, \quad (4.20)$$

where $k = \mathcal{O}(1)$. Thus, adiabatic decompression takes a time $T > k/\omega_f$, where ω_f is the final trapping frequency. In our case, the time required would be $\sim 2 \text{ s}$, which is impractical. Delta-kick cooling results in the same final momentum distribution as adiabatic decompression, but has

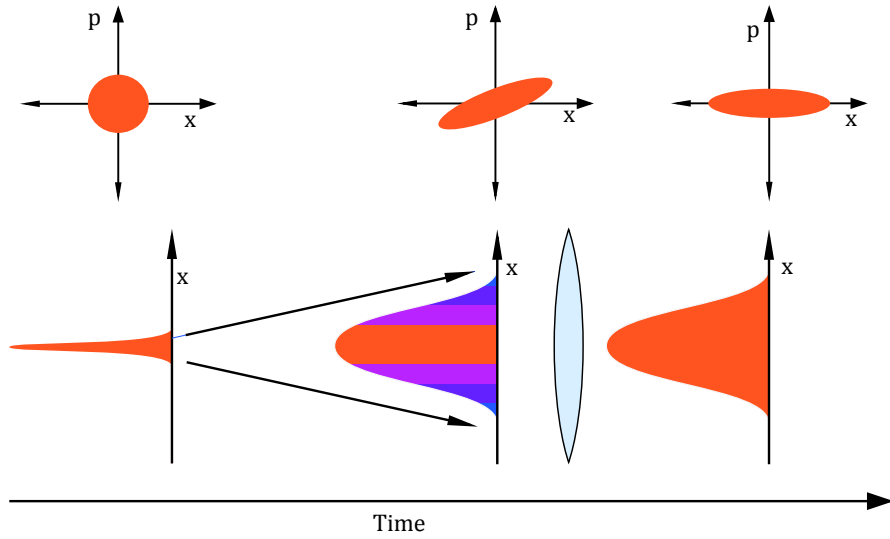


Figure 4.7: Illustration of the delta-kick cooling technique. An initially trapped cloud when released freely expands so that the fast momentum components travel further as compared to the slow ones. This correlates position with momentum. Pulsing an a lens, which is harmonic trapping potential, for a short duration brings the cloud to rest.

the practical advantage of being $\Delta x_f / \Delta x_0$ times faster than adiabatic decompression. Here, Δx_f and Δx_0 are the final and initial rms widths of the cloud respectively. While the idea of Delta-kick cooling has been around for some time[77–79], there has been a renewed interest in this technique in atom interferometer experiments using a Bose-Einstein condensate[80–83]. The motivation to use Delta-kick cooling in these experiments is the same as in ours: to non-adiabatically decompress and collimate the cloud so that the effect of mean field energy is negligible. It should be noted that unlike evaporative cooling, both adiabatic decompression and delta-kick cooling do not increase phase-space density of the cloud. The velocity spread Δv decreases at the cost of increasing the size of the cloud Δx , such that $\Delta x \Delta v$ never increases ($\Delta x \Delta v$ is constant for an ideal kick).

The basic principle behind the technique, as illustrated in Fig. 4.7, is to pulse on a harmonic potential for a short duration and apply a “ δ -kick” to a freely expanding cloud and bring it to rest. This is exactly equivalent to using a lens to collimate a diverging beam of light. Consider a cloud of initial rms size Δx_i and an rms velocity spread Δv_i released from a trap so that it freely expands for a time t_0 . If $t_0 \gg \Delta x_i / \Delta v_i$, then the final velocity and position of the cloud are correlated, i.e. the velocity of particles at a position x is given by x/t_0 , with an error $\Delta x_0/t_0$ due to the finite initial size of the cloud. When a harmonic potential of trapping frequency ω is pulsed for a short time τ , the total momentum transferred to a particle at a position x is given by $-m\omega^2 \tau x$. The velocity of the particle after the kick is given by

$$v_f = (1/t_0 - \omega^2 \tau)x. \quad (4.21)$$

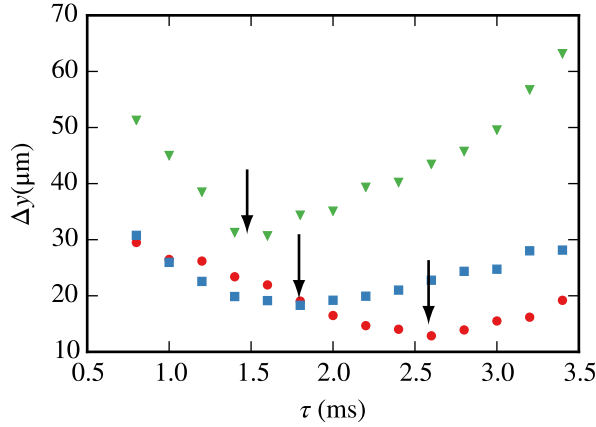


Figure 4.8: Collimating the wavepacket by adjusting the kick strength. The rms width of the cloud as a function of the delta-kick pulse duration for three expansion times: 20 ms (red circles), 42 ms (blue squares) and 60 ms (green triangles). The arrows indicate the kick strength required to focus the atoms for a particular expansion time.

An ideal kick, which would bring the particle to rest ($v_f = 0$) satisfies the condition $\omega^2\tau = 1/t_0$. If the kick is not ideal, the particle would either focus at some later point in time, or keep diverging, depending the strength of the kick. The time at which it focuses t_f , is given by $t_f = -x/v_f$. Plugging this in Eq. 4.21 gives us the lens equation for delta-kick cooling:

$$\frac{1}{t_f} + \frac{1}{t_0} = \frac{1}{f}. \quad (4.22)$$

Here, f is the focal time, given by $f = 1/\omega^2\tau$. In the case of a collimating pulse, the collimation would be perfect if we started with a point source. However, if the initial cloud has a size Δx_0 , then the final velocity of the particle has an uncertainty $\Delta v_f = \Delta x_0/t$. The size of the cloud after expansion is related to the initial spread in velocity: $\Delta x_f = \sqrt{\Delta x_0 + \Delta v_0 t} \approx \Delta v_0 t$. Combining these, we get $\Delta x_0 \Delta v_0 = \Delta x_f \Delta v_f$, which is the condition for conserving phase space density. Thus, the final velocity spread for an ideal collimating kick is given by $\Delta v_f = (\Delta x_0 / \Delta x_f) \Delta v_i$. In practice, effects due to interactions between the atoms, aberrations due to non-harmonic potentials and interference patterns in the delta-kick beam will limit the achievable reduction in the velocity spread.

In this section, I will present preliminary one dimensional delta-kick cooling results. A reduction of 2.4x in the velocity spread was achieved for atoms expanding in a magnetic waveguide. The magnetic waveguide was chosen as the SLD waveguide (see Sec. 3.5.2) was still under development at that time.

We start with 300k atoms in a pure BEC prepared in the hybrid trap (see Sec. 3.8.4). After preparing the BEC, the magnetic field gradient is ramped to $B'_y = 15.2 \text{ G/cm}$ to cancel the gradient due to gravity. When the hybrid trap beam is switched off, the atoms freely expand in the vertical (y) direction and are confined in the horizontal x and z directions with trapping frequencies $(\omega_x, \omega_z) =$

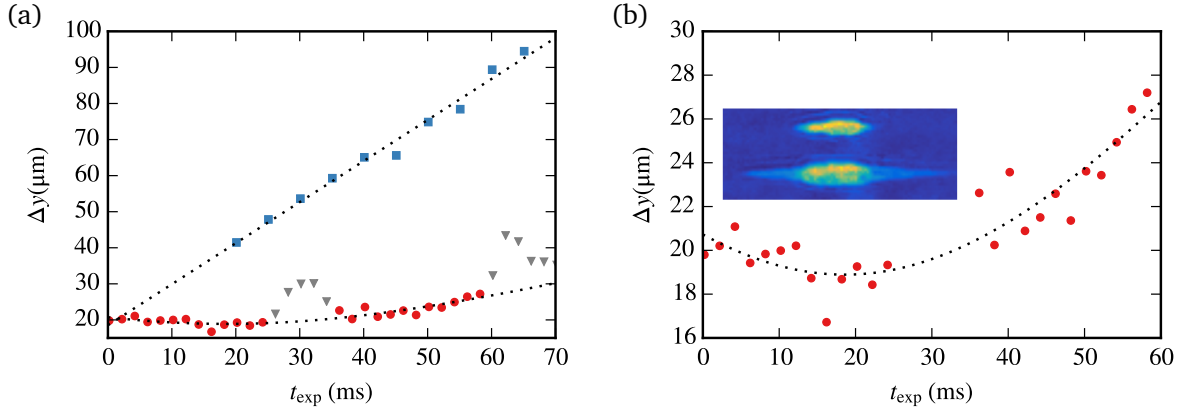


Figure 4.9: Delta-kick cooling in the magnetic waveguide. (a) The rms size of the non-kicked (blue squares) and kicked cloud (red circles). Fits give an rms velocity spread of $1.10(5)$ mm/s and $0.46(5)$ mm/s for the non-kicked and kicked cloud respectively. The corresponding temperatures are $13(1)$ nK and $2.0(4)$ nK. The gray triangles are excluded from the fit as the optical density saturates at those points, causing the fit to over-estimate the width of the cloud. The cloud undergoes breathing mode oscillations in the x induced by the delta-kick beam and the optical density saturates when the cloud is compressed. (b) rms size of only the kicked cloud as a function of expansion time. Inset shows an absorption images of the kicked cloud right after the kick and after 60 ms of expansion time. The horizontal extent of the image is $100\text{ }\mu\text{m}$.

$2\pi \times (16, 32)$ Hz. The initial y confinement, provided by the hybrid trap beam is $\omega_y = 2\pi \times 35$ Hz. The rms width of the cloud during free expansion without the kick is shown in Fig. 4.9(a). The initial expansion is driven by the mean field energy of the cloud.

The delta-kick beam is formed by a 1064 nm beam propagating along the imaging direction. The beam is sent through the barrier objective (see Sec. 3.5.3). The waist of the beam when it hits the atoms is $150\text{ }\mu\text{m}$, measured using the imaging system. The beam is centered on the atoms by applying a strong kick and measuring the position of the cloud after a long time of flight. If the beam is off center, this results in a non-zero center of mass velocity of the cloud.

We choose an initial expansion time of $t_0 = 15$ ms and determine the strength of the kick required to collimate the atoms by focusing the atoms at progressively larger expansion times (see Fig. 4.8). A kick duration of 1.5 ms focused the cloud at 60 ms. A kick duration slightly less than 1.5 ms, was chosen to collimate the atoms. Fig. 4.9(b) shows the rms width as a function of the expansion time for a 1.3 ms kick duration.

We see that the kick reduces the velocity spread by a factor of 2.4 to $0.46(5)$ mm/s, which is about 4 times higher than our the expected reduction for an ideal kick. The expected reduction is calculated by first using the scaling solution[25] to estimate the size and phase curvature of the condensate after 15 ms of expansion 4.10(a). The effect of the kick is included by applying a phase mask $\phi(x)$ across the wavefunction. A parabolic phase mask is applied to simulate an ideal kick, whereas a Gaussian phase mask is used to determine the aberrations due to the finite size of the beam. From Fig. 4.10(b), we see that even after accounting for the Gaussian profile of the kick, we

expect $\Delta v \sim 0.1 \text{ mm/s}$. Thus aberrations due to finite beam size cannot explain the discrepancy between the measured and expected value.

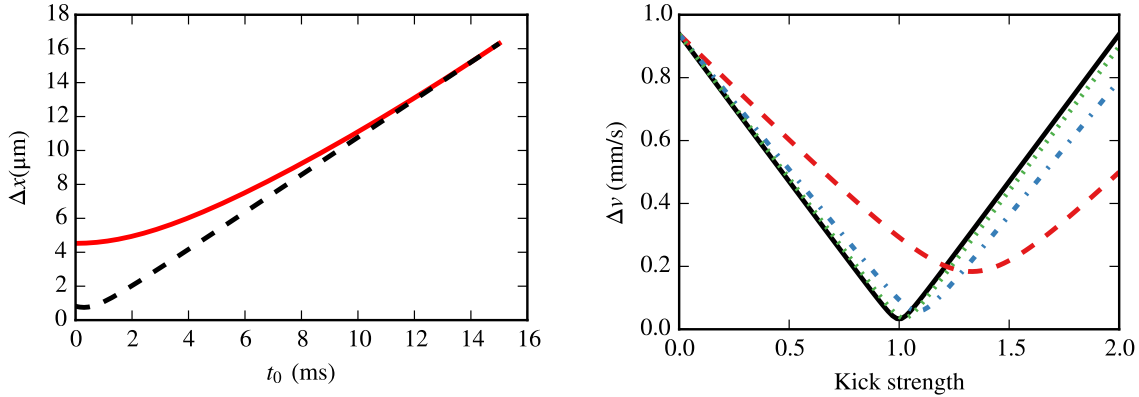


Figure 4.10: Role of interactions and aberrations in delta-kick cooling. (a) Expansion of an interacting condensate in the waveguide determined by numerically solving the scaling solution. The black dashed line is determined by propagating the final wave-function back in time with the interactions turned off. This determines the size and position of a virtual source of a non-interacting cloud. (b) Velocity spread after the kick as a function of the kick-strength for an ideal parabolic potential (solid black), a Gaussian potential with a 50 μm waist (dashed red), 100 μm waist (dashed-dotted blue) and 200 μm (dotted green). A kick-strength of 1 collimates the atomic cloud.

The inset in Fig. 4.10(b) shows the absorption images right after the kick and after 60 ms of expansion. We see that the cloud develops a bi-modal distribution, with the central lobe essentially the same size as the original cloud. In fact, if we fit the distribution to a sum of a Thomas-Fermi and a Gaussian distribution the width of the central part is the same as the initial size of the cloud. The extra contribution to Δx comes solely from the wings. The bi-modal distribution could be due to high frequency spatial interference patterns in the intensity profile of the beam, which would severely distort the cloud[83]. We expect heating due to scattering of photons from the beam to minimal.

In summary, using delta-kick cooling, a velocity spread $\Delta v = 0.46(5) \text{ mm/s}$ for a cloud size $\Delta x = 20 \mu\text{m}$ is achieved for atoms expanding in a magnetic waveguide. The velocity spread is 25 times larger than the Heisenberg limited spread $\hbar/2m\Delta x = 0.02 \text{ mm/s}$ and is twice the required spread for the tunneling time experiments. Similar results are expected when the atoms are expanding in the SLD waveguide, since we start with a similar initial velocity spread (see Fig. 3.12). The less than optimal performance of the kicking is suspected to be due to interference patterns in the delta-kick beam.

4.4 First generation Larmor clock

We use the Zeeman levels in the $F = 2$ hyperfine manifold of the ground state for the first generation Larmor clock. The Zeeman states are used as the frequency difference required between the Raman

beams for two photon resonance is in the MHz range and can be easily generated using acousto-optic modulators. State preparation and detection is also relatively straightforward using RF pulses and Stern-Gerlach time of flight measurements. The downside of using Zeeman states is that the two-photon detuning is susceptible to fluctuations in the background magnetic field. In Sec. 4.2, we determined that the magnetic field stability had to be much better than 0.5 mG. Such a high degree of magnetic field stability is hard to achieve without some form of active feedback or mu-metal shielding[84, 85]. As a first step, we decided to characterize the magnetic field stability.

In this section, I will describe our excursions into exploring the interaction of spins with RF fields and Raman beams. I will begin by describing our efforts to characterize and reduce magnetic field noise. The atoms were used as a probe to measure fluctuations in the magnetic field. We explored Rabi oscillations of $F = 2$ spins, where to our surprise, we could detect the effect of the quadratic Zeeman shift even in small ~ 1 G magnetic fields. Preliminary experiments with condensates traversing the Raman beams were carried out and the dwell time of a freely propagating BEC was used to calibrate the Larmor clock.

4.4.1 Magnetic Field Noise

The magnetic field experienced by the atoms is subject to noise from various sources— mains noise at 60 Hz, noise in the current drivers for the bias coils, eddy currents induced by fast switching of coils, electrical equipment turning on and off in the building, streetcar and subway noise, etc. In April 2015, we made an attempt to characterize the noise, first using a magnetometer and then using the atoms themselves as a magnetic field sensor.

Fig. 4.11 and Fig. 4.12 show B field measurements using the magnetometer placed on the optical table about 20 cm away from the vacuum chamber. The voltage output of the magnetometer was sent to a summing amplifier with a gain of 3 and a low pass filter with a cutoff frequency of ~ 300 Hz. The second input of the summing amplifier was connected to a variable voltage power supply to null the offset in the magnetic field. The output of the amplifier was monitored on a Tektronix TDS1002 oscilloscope. A computer read off 1 s averages via GPIB and time stamped it. The magnetometer was calibrated using earth's magnetic field as a reference.

The magnetic field in the vertical direction (Fig. 4.11) shows fluctuations of 1.6 mG (computed as the standard deviation around a 1 minute running average), which is an order of magnitude higher than the 0.14 mG fluctuations in the z direction (Fig. 4.12). Interestingly, the vertical field fluctuations go down to 0.16 mG at night between 2 a.m. to 6 p.m. This data was taken over the weekend, where there was no activity inside the lab and no equipment in the lab was switched on or off, indicating that the cause was outside the lab. Similar fluctuations were seen in Prof. Thywissen's lab and the street cars running on College St. or Spadina St. were suspected of causing it. However, this data was taken while the street car lines were closed due to undergoing repairs, so the source of the fluctuations remains a mystery.

To further investigate the magnetic field noise, the atoms themselves were used as a sensitive probe of the magnetic field. A BEC is prepared in a crossed dipole trap and a bias field of 0.9 G

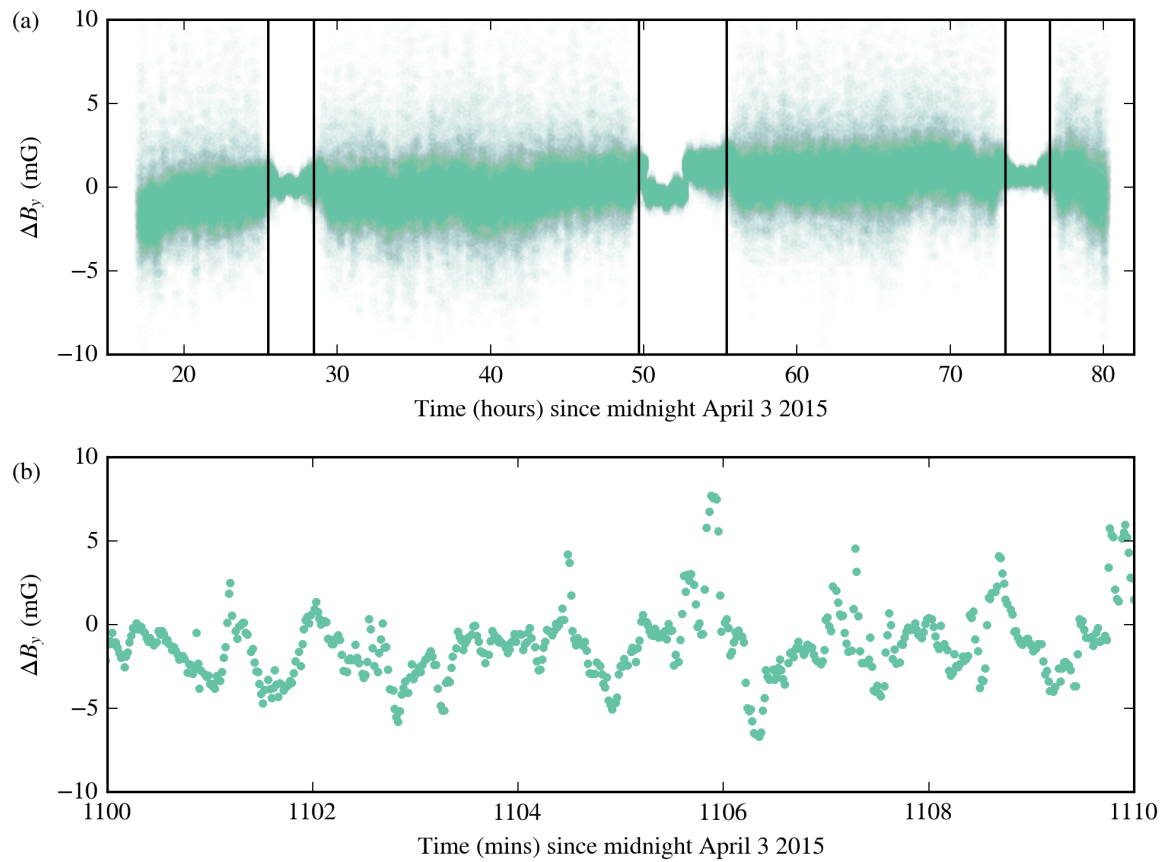


Figure 4.11: Magnetic field in the vertical (y) direction as a function of time. The magnetic field is quieter at night, between 2 a.m and 6 a.m as indicated in regions between the solid black lines. (b) shows typical slow drifts of a few mG on a time scale of a minute.

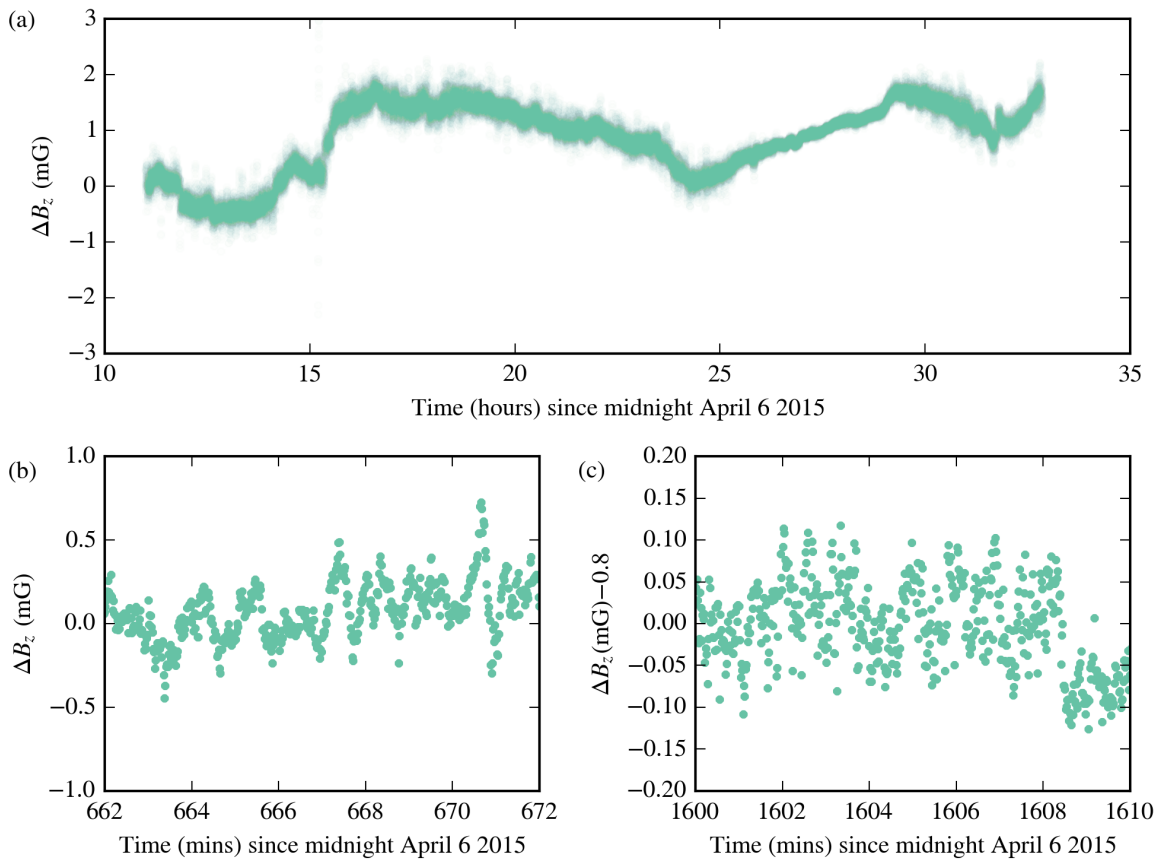


Figure 4.12: Magnetic field in the bore (z) direction as a function of time. Fluctuations in the magnetic field are an order of magnitude less than in the vertical direction (see Fig. 4.11). (b) shows typical fluctuations over the course of a few minutes whereas (c) shows the relatively quiet magnetic field during the night.

is applied in the z direction. The x and y bias coils are used to null the transverse magnetic field to less than 20 mG (see Sec. 3.3.2). The Zeeman shift is measured by applying a 1 ms RF π -pulse and scanning the frequency of the pulse (see Fig. 4.13). Once the resonance frequency is found, 15 shots with the RF frequency set to the resonance frequency are taken and the shot to shot stability of the angle of rotation θ of the spin is measured. The rotation angle is given by

$$2 \cos \theta = \langle F_z \rangle / \hbar \quad (4.23)$$

and for an ideal on resonance π -pulse, $\theta = \pi$. Deviations from an ideal π pulse are used to characterize the magnetic field noise. The entire sequence of finding the center frequency and then probing the stability of π pulses is put in a loop which is run for a period of around 14 hours starting at 5 p.m. The spread in angles seen in the data (see Fig 4.14) is consistent with the fluctuations in B_z measured using the magnetometer (Fig. 4.12). The spread in angles goes down by a factor of 2 at night when the magnetic fields are quieter.

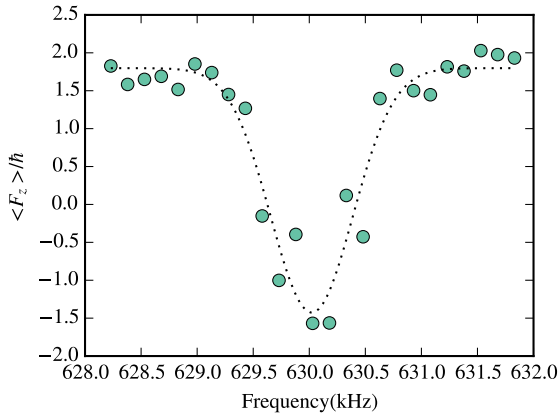


Figure 4.13: Measuring the Zeeman shift using a 1 ms RF pulse. The magnetization of the BEC is plotted as a function of the frequency of the RF pulse. A Gaussian fit is used to determine the resonance frequency and width of the resonance.

Apart from slow drifts, 60 Hz fields from the mains line are a significant source of noise. For all experiments probing the spin of the BEC, the experiment clock is paused after preparing the BEC in a crossed dipole trap and resumed in sync with the mains line (see Sec. 3.7.1). When the duration of the experiment is much smaller than the period of the mains line (16.7 ms), the synchronization ensures that the atoms experience a constant offset due to the main line. The synchronization is done after making the BEC rather than at the beginning of the ramp as the phase of the mains line can drift by 2π in 15-20 seconds.

Synchronizing to the mains line dramatically increases the shot to shot stability of Rabi oscillations. In the absence of synchronization, Rabi oscillations with $\Omega = 2\pi \times 3.5$ kHz are stable only for the first 200 μ s, whereas with the stabilization they persist for ~ 5 ms (see Fig. 4.16).

In experiments measuring the dwell time, the BEC interacts with the Raman beams for a duration

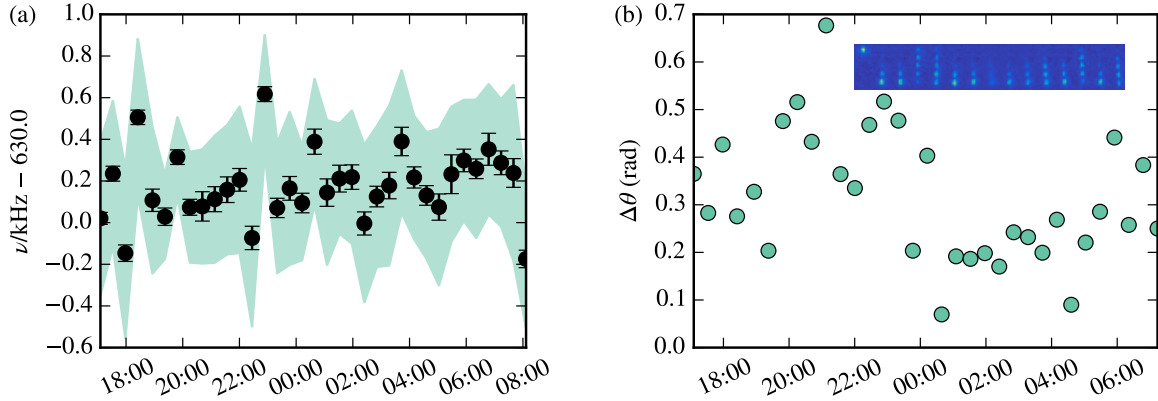


Figure 4.14: Long term B field drifts measured using RF spectroscopy. (a) Measured resonance frequency as a function of the time of day when the data was taken. Cyan bands indicate the fitted width of the Gaussian, whereas the black dots indicate the center. (b) Spread of angle of rotation of the spin when a π pulse is applied. The spread goes down by a factor of 2 between 2 a.m. and 6 a.m. The inset shows typical shot to shot stability for a 1 ms π -pulse. In the absence of B field fluctuations, all the atoms should be transferred to the bottom ($m_F = -2$).

of ~ 10 ms. The 60 Hz noise causes the resonance frequency to change as the BEC traverses the Raman beams. Depending on the two photon detuning and the phase of the mains line, only parts of the BEC undergo spin rotations. This is a major source of noise in the dwell time measurements.

4.4.2 Quadratic Zeeman shift

The degeneracy of the magnetic sublevels is lifted when an external magnetic field is applied. To first order, the energy shift of the magnetic sublevel m_F is given by $\Delta E = \mu_B m_F g_F B$. Higher order corrections arise since interaction Hamiltonian $H_Z = -\boldsymbol{\mu} \cdot \mathbf{B}$ is not diagonal in the total angular momentum basis (see Appendix B). For ^{87}Rb , the quadratic correction is given by

$$\Delta E_{|F,m_F\rangle}^2 = h \times (-1)^F (1 - m_F^2/4) (287.6 \text{ Hz/G}^2) \times B [\text{G}]^2 \quad (4.24)$$

The quadratic Zeeman shift breaks the uniform ladder between m_F states and can be used to prepare atoms in a specific m_F state. For example, we can transfer atoms to the $F = 2, m_F = 0$ clock state starting from the magnetically trappable $F = 2, m_F = 2$ state with high fidelity using RF sweeps. Fig. 4.15 shows how the resonance frequencies for transitions between m_F states deviate from the linear Zeeman shift. At moderate B fields in the 15 G to 20 G range, two RF sweeps of 2 ms duration across the $f_{2,1}$ and $f_{1,0}$ resonances transfers the atoms first to the $m_F = 1$ and then $m_F = 0$ state. Alternatively, a broad sweep starting with a high frequency and going to a lower frequency will transfer the atoms one m_F state per sweep.

A fascinating consequence of the quadratic Zeeman shift is the appearance of beat notes in Rabi oscillations when a RF field is applied, as shown in Fig. 4.16(a). A BEC is prepared in a crossed

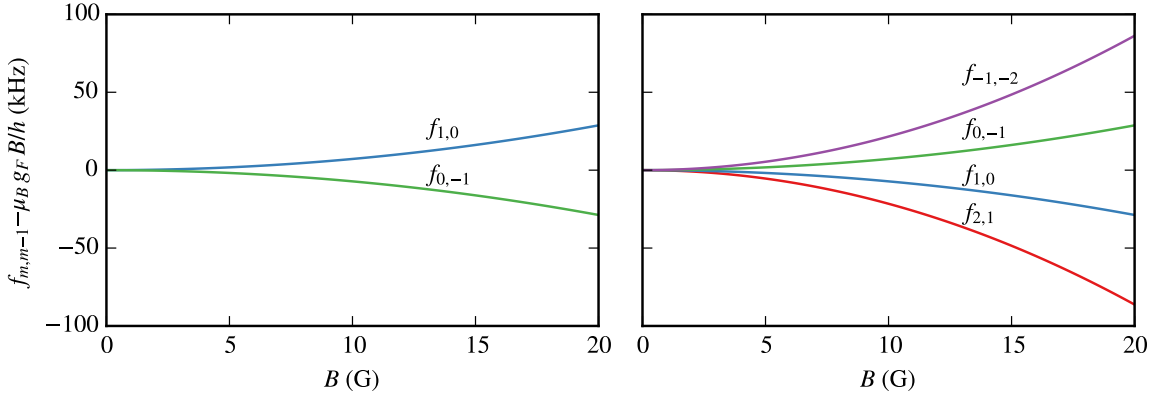


Figure 4.15: Resonance frequencies $f_{m,m-1}$ for transitions $m \rightarrow m-1$ after subtracting the linear part of the Zeeman shift as a function of the applied bias field B for the $F = 1$ (left) and $F = 2$ (right) manifolds.

dipole trap in the $F = 2, m_F = 2$ ground state and a bias field of 1.96 G is applied in the x direction (see Sec. 3.3.2). An square RF pulse with a center frequency of 1375.8 kHz and a varying pulse width from 8 μ s to 5 ms is applied. After this the BEC is released from the trap by abruptly turning off the trapping potentials. A magnetic field gradient is applied in the z direction, which spatially separates atoms in different Zeeman sublevels. After 20 ms of time of flight, an absorption image is taken (see Fig. 4.16(c)). The number of atoms in each m_F state is counted by integrating the optical density in a given region of interest and the average magnetization is calculated using

$$\langle F_z \rangle / \hbar = \frac{\sum_{i=-2}^2 i N_i}{\sum_{i=-2}^2 N_i}. \quad (4.25)$$

The magnetization $\langle F_z \rangle$ oscillates at a Rabi frequency of $\Omega = 2\pi \times 3.8$ kHz. In addition, the envelope is seen to oscillate with a time period of 3.6 ms. This can be seen as a splitting of lines by $1/3.6$ ms = 280 Hz, as seen in Fig. 4.16(b). The splitting matches with the energy difference between the $m_F = 0$ and $m_F = 1$ states

$$E_1 - E_0 = \frac{\hbar}{4} 287.6 \text{ Hz/G}^2 \times B [\text{G}]^2 = \hbar \times 276 \text{ Hz} \quad (4.26)$$

for a magnetic field strength of 1.96 G.

4.4.3 Larmor clock calibration

Characterization of the magnetic field in Sec. 4.4.1 indicated that the long term drift in the magnetic field in the z direction is about 1 mG over a few hours, whereas the short term drift on a 1 minute scale is less than 200 μ G. The short term stability increases by a factor of 2 at night between 2 a.m and 6 a.m. If the long term drifts are corrected for, the magnetic field noise seemed to be just on

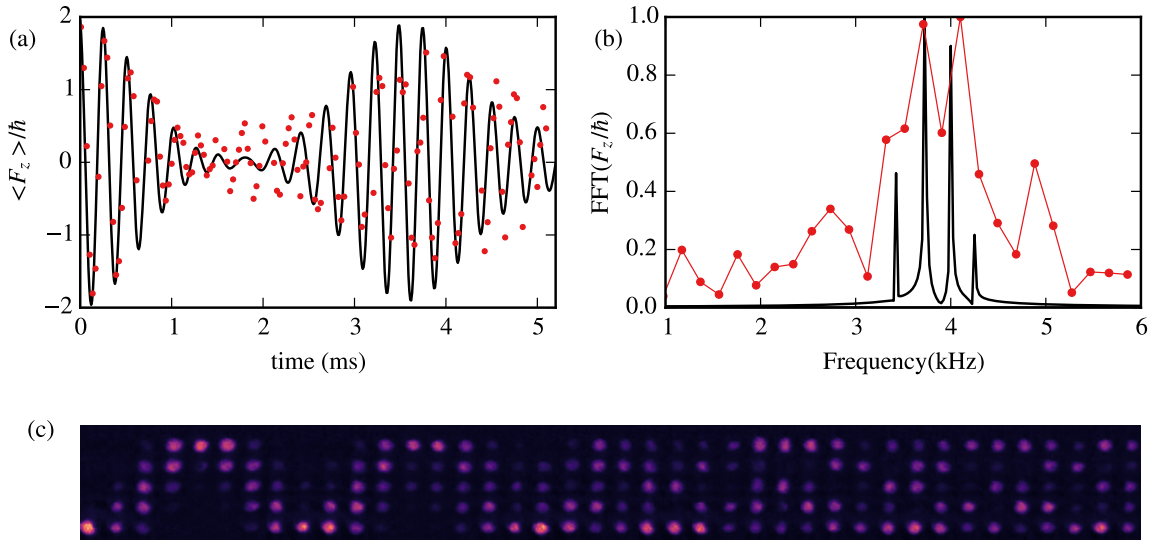


Figure 4.16: Observing the quadratic Zeeman shift for low magnetic fields. (a) Magnetization of the BEC as a function of time in the presence of a RF field. Red circles are data and solid black line is a numerical simulation of a five level system in an RF field with center frequency 1375.8 kHz and strength $\Omega_{rf} = 2\pi \times 3.8$ kHz. (b) Fourier transform of the data and simulations shown in (a). In the absence of the quadratic Zeeman shift, a single peak at 3.8 kHz is expected. The data can clearly resolve the two peaks, whereas the simulations show peaks corresponding to all four resonances. (b) Collage of absorption images showing populations in different m_F states as a function of time. The first and the second Rabi oscillations are clearly visible. From the third oscillation onwards, a buildup of population in the $m_F = 0$ state is seen, which reduces the expectation value of F_z .

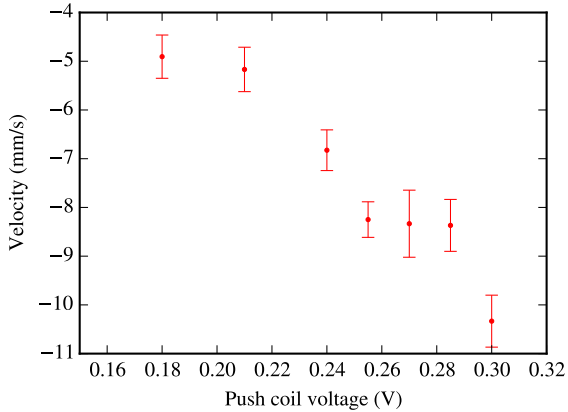


Figure 4.17: Push coil calibration. The velocity of the condensate is plotted as a function of the control voltage applied to the push coil current driver.

the border of being acceptable for the Larmor clock experiments. Hence, we decided to try out the Raman beams and test the stability of the Larmor clock.

The setup for generating and focusing the Raman beams is described in Sec. 3.6. We use light at the 790.03 nm tune-out magic wavelength for the Raman beams. At this wavelength, the AC stark shift vanishes[43–45]. This is important for the tunneling experiments as we do not want the Raman beams to change the height of the barrier. The Raman beams are focused to a beam waist of $4.2\text{ }\mu\text{m}$, which is much higher than the required focus for the tunneling time experiments. Since the preliminary experiments only study properties of the Larmor clock, we did not bother to focus the Raman beams tighter.

The following experiments measure the rotation angle of the spin of the condensate as it traverses through these Raman beams. The experimental sequence is as follows: a pure BEC with $\sim 80\text{k}$ atoms is initially prepared in the $|F = 2, m_F = 2\rangle$ ground state in a purely optical trap formed by the SLD beam and the crossed dipole trap beam. A 1.7 G magnetic field applied along the z direction sets the quantization axis and the Zeeman splitting. The condensate is released into the SLD waveguide and a magnetic field gradient along z is pulsed on for 4 ms to accelerate the condensate to a final velocity v . The magnetic field gradient is applied by a single 45 turn push coil (see Sec. 3.3.4). Fig. 4.17 shows the calibration of the push coil. A pair of Raman beams propagating in the x direction intersect the waveguide. The Raman beams induce $\pi - \sigma_-$ two photon transitions when the atoms traverse through them. The z position of the Raman beams is adjusted so that the leading front of the condensate collides with the Raman beams 6 ms after the magnetic field gradient is turned off. This allows for transients in the magnetic field to settle down. The sequence is timed so that the collision happens at a maxima of the 60 Hz line voltage to minimize the effect of a time dependent magnetic field. Depending on the velocity of the condensate, the entire condensate takes 10-20ms to traverse through the Raman beams. After this, the Raman beams and the waveguide is turned off and a magnetic field gradient is applied along the y direction to spatially separate the spin components during time-of-flight. After 20 ms of time-of-flight, an absorption image is taken.

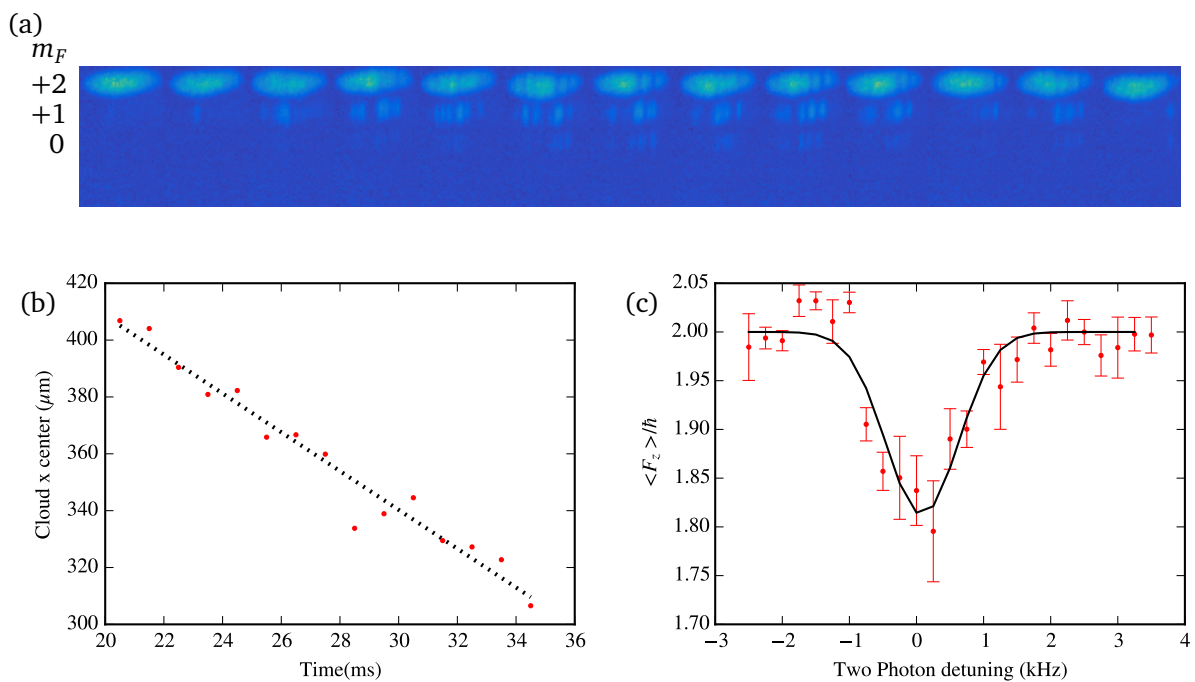


Figure 4.18: Measuring spin rotation due to the Raman beams. (a) A collage of absorption images of the condensate when the two-photon detuning is scanned. (b) Position of the condensate with time after accelerating it in a magnetic field gradient. A straight line fit gives a velocity of 6.8(4) mm/s. (c) The expectation value of \hat{F}_z as a function of the two-photon detuning. Each data point is an average of 5 shots.

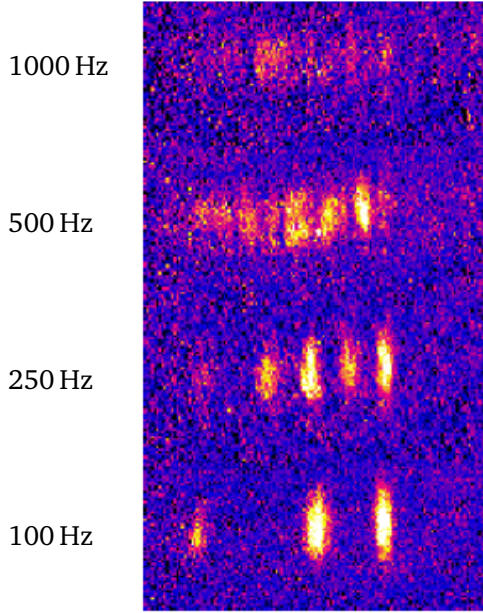


Figure 4.19: Intentional modulation of the magnetic field. The population in the $m_F = 1$ state when the magnetic field is intentionally modulated. Vertical stripes are seen whenever the Zeeman splitting matches the two photon resonance.

The Larmor clock is calibrated by measuring the angle of rotation θ of the spin for various incident velocities v . For each incident velocity, the two photon detuning is scanned to determine the resonance frequency. The two photon Rabi frequency is set to be low enough so that θ is small. The spin is predominantly in the $m_F = 2$ state after the interaction, with a small population in the $m_F = 1$ state and very little population in the $m_F = 0$ state. The effect of the Raman beams is not a simple rotation of the $F = 2$ spin, but depends in a non-trivial way on the Clebsch-Gordon coefficients between the ground state and the intermediate virtual states[46]. Restricting the rotation to small angles simplifies the analysis.

Fig. 4.18(a) shows a collage of absorption images as the two-photon detuning is scanned across the resonance. We see that when off resonance (images on the left and right), there is no coupling to the $m_F = 1$ state. When close the two photon resonance, a large number stripes in the $m_F = 1$ states are seen. These stripes are due to fluctuations in the magnetic field bringing the Zeeman states in and out of resonance as the condensate traverses the Raman beams. The frequency of the spatial modulations of the intensity pattern in $m_F = 1$ directly corresponds to the frequency of the fluctuating magnetic field. We see, for example, that if the incident velocity of the condensate is higher, then the stripes are spaced apart at a larger distance. The structure of the stripes can, in principle, be used to extract information about the nature of the magnetic field fluctuations. While we did not perform a detailed analysis, we determined that the dominant source of noise in the magnetic field was at ~ 250 Hz. This was done by intentionally modulating the magnetic field at a known frequency and comparing the resulting stripe pattern with the naturally observed pattern (see Fig. 4.19).

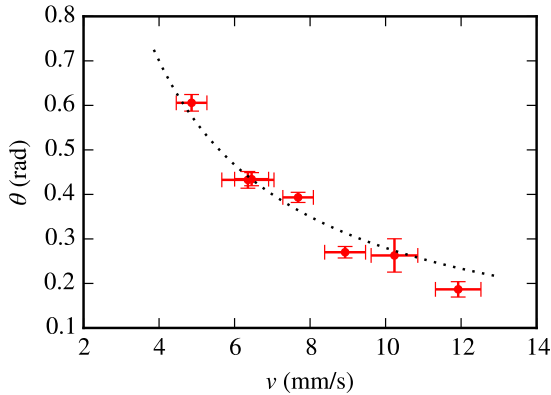


Figure 4.20: Rotation angle θ vs. incident velocity v . Dotted line is a fit to the function $\theta = k/v$, with $k = 2.80 \pm 0.05$ rad/(mm/s).

While the magnetic field fluctuations somewhat degrade the signal, it is still possible to extract an average rotation angle θ . Fig. 4.18(c) shows the expectation value of \hat{F}_z as a function of the two photon detuning. We fit the data to a Gaussian function and determine the height of the Gaussian $\langle \hat{F}_z \rangle_{\max}$. The rotation angle θ is given by

$$\theta = \cos^{-1} \left(\frac{\langle \hat{F}_z \rangle_{\max}}{2\hbar} \right). \quad (4.27)$$

Fig. 4.20 plots the rotation angle θ as a function of the incident velocity v . From Eq. 4.18, we expect θ to be inversely proportional to v . Fitting the data to a function of the form $\theta = k/v$ gives us the calibration of the Larmor clock.

Although the data in Fig. 4.20 clearly shows the expected trend of the Larmor clock, whether this clock can be used for the tunneling time experiments depends on how well the fast fluctuations in the magnetic field can be suppressed. We have seen that long term drifts in the magnetic field can be corrected for by periodically scanning across the resonance. The shot-to-shot stability when the experiment is synchronized to the line voltage is less than $200 \mu\text{G}$ over a 1 ms period. However, the interaction time of the condensate with the Raman beams, given by $t_{\text{int}} = l/v$, where l is the extent of the condensate wavepacket, ranges from 10-20 ms. The effects of noise at 60 Hz, as well as noise at a higher frequency of ~ 250 Hz can be clearly seen in the data.

A number of steps are currently being taken to reduce the magnetic field noise. Electronics and power supplies stacked close to the chamber are being moved to a separate rack ~ 6 m away. Preliminary attempts to measure and correct for the 60 Hz noise have been partially successful. We are also investigating using active feedback to suppress noise in a 1 kHz bandwidth.

If these attempts at reducing magnetic field noise are not successful, an alternative is to use the $|F=2, m_F=0\rangle \rightarrow |F=1, m_F=0\rangle$ clock transition which does not have a first order Zeeman shift. The downside is that the preparation and detection sequence would be significantly more

complicated than the current scheme.

4.5 Summary

This chapter describes the experimental progress made towards measuring the tunneling time. A number of new tools were developed to meet the experimental requirements for the tunneling time experiments. These include a thin optical barrier using 405 nm light, a smooth optical waveguide using broadband light and Raman beams operating at the 790 nm magic-zero wavelength. A 2.4x reduction in the longitudinal velocity spread of the atoms was demonstrated using Delta-kick cooling.

While these improvements and additions bring us ever closer to measuring the tunneling time, a number of challenges still remain. An additional factor of 2 reduction in the velocity spread is required to reliably distinguish between tunneling and classical transmission. The Raman beams have to be focused well within the barrier region to measure conditional dwell times. Finally, the stability of the Larmor clock has to be increased, either by suppressing magnetic field noise, or by switching to using the magnetically insensitive clock states.

Chapter 5

Interaction Assisted Tunneling of a BEC Out of a Quasi Bound State

The construction and characterization of a thin barrier beam naturally led us to the question: *can we observe tunneling through this barrier?* The basic criteria to observe tunneling is that the incident particles have a well defined energy which is very close to the barrier height. Ch. 4 considered tunneling in the scattering configuration, where a condensate released in a waveguide has one chance to tunnel through the barrier. We concluded that during expansion in the waveguide, the interaction energy of the condensate increases the kinetic energy spread and severely limits the number of atoms that participate in tunneling. Additional cooling is required to increase the tunneling signal.

However, a zero temperature condensate prepared in the ground state of a trapping potential does have a well defined energy and is phase coherent over the entire length of the cloud. This has been demonstrated in numerous experiments. While the observation of quantized vortices implies long-range order[86–88], phase coherence has been explicitly observed by interference of two BECs[89], interference of atoms outcoupled from different positions within a condensate[90] and measurement of higher order coherences[91]. Tunneling of trapped condensates does not suffer from the problem of large energy spreads. Furthermore, a trapped condensate has many chances to tunnel as it bounces back and forth in the trap, making tunneling easier to observe. This motivated us to explore tunneling dynamics of a trapped condensate, which I will describe in this chapter.

5.1 Introduction

The escape of a particle from a quasi-bound state due to tunneling is one of the earliest problems studied in Quantum Mechanics and was successfully applied to explain α -decay of nuclei[92]. It explained the random nature of the decay and also why the range of nuclear lifetimes spans many orders of magnitude, while the energy of the emitted particles changes by only about a factor of two. Since then, bound state tunneling has been studied in numerous systems, ranging from particle physics to biological systems. Most of these systems have the property that particles decay indepen-

dently of one another, which leads to the usual exponential dependence of the survival probability with time.

There has been a growing interest in studying tunneling of systems with many degrees of freedom. This is motivated by the desire to observe novel many body effects that affect the tunneling process, arising either due to inter-particle interactions or particle statistics (or both)[9]. A second motivation is to test the validity of Quantum Mechanics at the macroscopic level, and investigate the crossover from Quantum to Classical, by studying manifestly quantum phenomenon, like tunneling, in macroscopic systems[93].

Recent advances in techniques for probing and manipulating ultra-cold atoms offer the possibility of exploring both these avenues. A number of beautiful experiments have been performed studying tunneling of the macroscopic order parameter between bound states. These include experiments in double-well systems, studying Josephson oscillations and self trapping[94], the DC and AC Josephson effect[95], and the crossover from hydrodynamic and Josephson regimes[96]. In optical lattice systems, the interplay between inter-well tunneling and strong interactions gives rise to the superfluid to Mott insulator transition. This was studied both for bosonic[10] and fermionic[11] species.

Experiments studying tunneling from a bound state into the continuum are fewer, and all of them study Landau-Zener(LZ) tunneling out of an optical lattice. Early work studying LZ tunneling showed pulse trains emitted at the Bloch frequency, which resulted due to interference of tunneled atoms from different lattice wells. This confirmed phase coherence of the condensate between lattice wells[7]. Since then, the role of inter-atomic interactions has been investigated in LZ tunneling[97, 98]. The experiments showed an increasing rate of LZ tunneling with increasing density of the condensate, which could be explained as a reduction of the lattice depth due to the mean-field energy of the condensate.

While experiments have been focused on studying tunneling between bound states, there has been much theoretical activity studying decay due to tunneling of ultra-cold gases. The effect of mean-field interactions on the tunneling rate has been calculated for both attractive and repulsive interactions[99], predicting a non-exponential decay curve. Dynamics of a trapped condensate tunneling out through a barrier reveal formations of shock waves inside the condensate, and blips emerging on the tunneled side, as well as the formation of solitons[100–102]. Studies of beyond mean-field effects consider decay of a strongly interacting Tonks-Girardeau gas[103] and the development of correlations and fragmentation in the tunneling process[104].

In this experiment, we report the observation of tunneling of a BEC out of a quasi bound state. A highly non-exponential decay is observed and the escape dynamics strongly depend on the mean-field energy. This gives rise to three distinct regimes— classical over the barrier spilling, quantum tunneling, and decay dominated by background losses. We show that in the tunneling regime, the decay rate goes down exponentially with decreasing chemical potential. Our results show good agreement with numerical solutions of the 3D Gross-Pitaevskii equation. To our knowledge, this is the first observation of tunneling of ultra-cold atoms out of a single trapping well(as opposed to a

lattice).

5.2 Repulsive Sheet Trap (ReST)

The Repulsive Sheet Trap (ReST) is a novel trap geometry used for studying escape dynamics of a condensate out of a quasi bound state. It is formed using a combination of a magnetic quadrupole trap and a single thin sheet of blue-detuned light. The acronym is inspired by the fact that the condensate “rests” above (or below, depending on the magnetic field gradient) the barrier sheet.

Blue-detuned light repels atoms since the dipole induced by the oscillating electric field is out of phase with the electric field[105]. At first glance a repulsive field seems unsuitable to create a trapping well. However, by combining it with other attractive potentials, a potential with a minima can be created. Such a minima occurs at places where the light intensity is low, hence these traps are also called dark optical traps[106]. The use of blue-detuned light for trapping atoms is not uncommon in ultra-cold atom experiments. The primary advantage, particularly in optical lattices with large depth[107, 108], is that since the atoms are trapped close to a intensity minimum, heating due to spontaneous emission is reduced. Dark optical traps are also used to create tight traps to create a 1D condensate[109], precisely control the trap depth and observe sub-Poissonian number statistics[110] and create uniform box potentials[111].

The ReST trap is conceptually similar to the gravito-optical surface trap[112], where the evanescent wave from total internal reflection acts as a mirror, reflecting back atoms which are falling due to gravity. In our case, a thin $1.3\text{ }\mu\text{m}$ sheet of light acts as the mirror, reflecting atoms vertically. Harmonic confinement in the horizontal x and z directions is provided by a magnetic quadrupole trap. The B -field zero of the quadrupole trap is above the atoms. Thus the atoms experience a magnetic field gradient in the vertical(y) direction, which is used to tune the net vertical acceleration a . Changing the field gradient also changes the horizontal trapping frequencies ω_x and ω_z .

5.2.1 Trapping Potential

For a quadrupole magnetic trap, the potential experienced by atoms in the $F = 2, m_F = 2$ ground state at a position y_0 below the B -field zero can be approximated as a field gradient with an acceleration $\mu_B B'_y/m$ vertically upwards and harmonic confinement in the x and z direction with trapping frequencies $\omega_x = 2\omega_z = \sqrt{4\frac{\mu_B B'_y}{my_0}}$ (see Sec. 3.8.4¹). In addition to the magnetic trapping potential, the atoms experience a repulsive potential $V_b(\mathbf{r})$ due to light sheet, and acceleration along the y direction due to gravity. The net potential energy is

$$V(x, y, z) = \frac{1}{2}m\omega_x^2x^2 + \frac{1}{2}m\omega_z^2z^2 + (\mu_B B'_y - mg)y + V_b(x, y, z). \quad (5.1)$$

¹Note that the x and z directions have been swapped here as compared to Sec. 3.8.4. This was done so that the barrier and absorption propagate in the z direction.

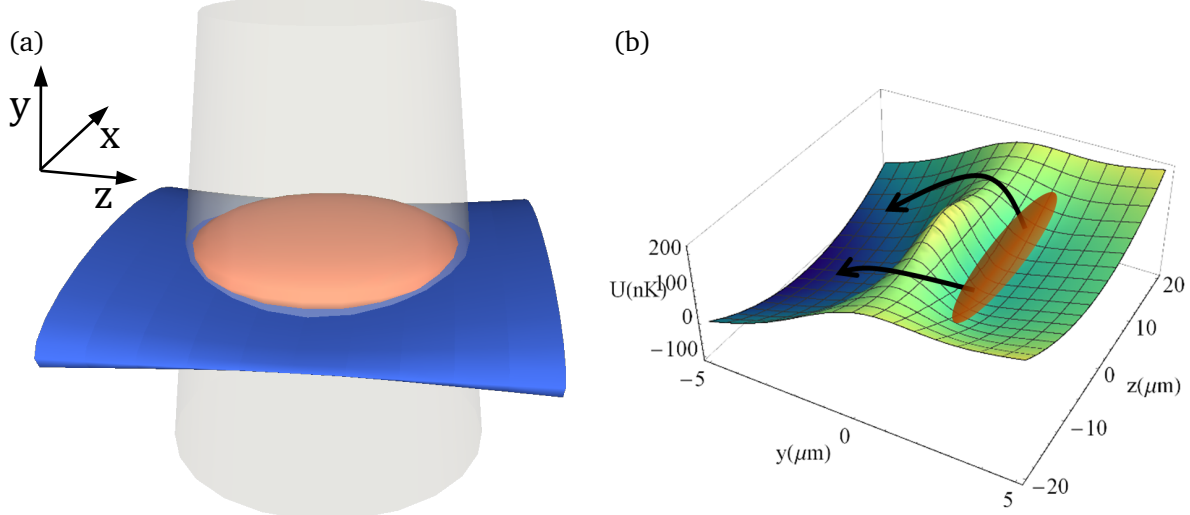


Figure 5.1: Trap geometry for studying tunneling out of a quasi-bound state. (a) A barrier sheet propagating in the z direction, shown in blue, forms a repulsive potential. The atoms are trapped above this sheet. The magnetic fields provide confinement in the horizontal x and z directions (shown in gray), and control the acceleration a in the vertical direction. (b) Potential energy experienced by the atoms at $x = 0$. The atoms are trapped in a small pocket created just above the barrier and tunnel down. The barrier height is a function of z since the tightly focused barrier beam diffracts out, reducing the barrier height off focus. The barrier is thinnest at $z = 0$ and broadens off focus.

The light sheet is described in detail in Sec. 3.5.3. Briefly, a Gaussian beam propagating in the z direction is tightly focused in the vertical(y) direction and weakly focused along x . Furthermore, the beam is scanned along x using an acousto-optic deflector at a frequency of 100 kHz, much faster than any atomic motion. The atoms see a time averaged potential in the x direction, which we sculpt using an arbitrary function generator.

The potential energy due to the light sheet is proportional to the intensity. For a Gaussian beam, it is given by

$$V_b(x, y, z) = V_0 \left(\frac{w_0}{w(z)} \right) \exp(-2y^2/w(z)^2) \quad (5.2)$$

where

$$w(z) = w_0 \left(1 + (z/z_R)^2 \right)^{1/2}. \quad (5.3)$$

$w_0 = 1.3 \mu\text{m}$ is the $1/e^2$ radius (Gaussian beam waist) of the beam, $z_R = 8 \mu\text{m}$ is the Rayleigh range and V_0 is the peak barrier height.

The trap geometry, along with the net potential is shown in Fig. 5.1. In Fig. 5.1b we see that since the barrier beam is diffracting out, the intensity of the beam, and hence the barrier height, is z dependent. It is maximum at $z = 0$ and drops as we move away from the focus. Similarly, the width of the barrier increases with z . For a condensate in this trap the tunneling proceeds through the edges where the barrier height is lower. The effective width of the tunnel barrier therefore depends

on the transverse size of the condensate.

In the experiment, there are two knobs available to change the trapping potential: the barrier beam power which changes V_0 and the magnetic field gradient B'_y , which changes the net tilt a as well as the horizontal trapping frequencies ω_x and ω_z . We have explored tunneling dynamics of the condensate in two different trapping configurations. This allows us to measure tunneling rates through two different effective barrier widths.

In the first configuration a magnetic field gradient $B'_y = 12.1 \text{ G/cm}$ is applied, which partially cancels gravity resulting in a net downward acceleration $a = 2.08(8) \text{ m/s}^2$ and a horizontal trapping frequency $\omega_x = 2\pi \times 32.7(3) \text{ Hz}$. (see Fig. 5.2).

For the second configuration, a higher magnetic field gradient of 28.3 G/cm is used so that the tilt due to the field gradient overcompensates gravity. This results in a net acceleration $a = 8.40(6) \text{ m/s}^2$ upwards and a tighter horizontal trapping frequency($\omega_x = 2\pi \times 86.6(6) \text{ Hz}$) as compared to the first configuration. The condensate is trapped *below* the barrier sheet and tunnels upwards towards the B -field zero. The escaped atoms are still confined in the magnetic trap and oscillate about the B -field zero. An RF knife at 1 MHz is used to transfer these atoms to an untrapped m_F state so that they escape. This configuration has a higher trapping frequency, which confines the condensate closer to the focus of the barrier, thus decreasing the effective width of the tunnel barrier.

The two trapping configurations will be discussed quite often, so for the sake of brevity they will be referred to as the *weak configuration* and the *tight configuration* respectively.

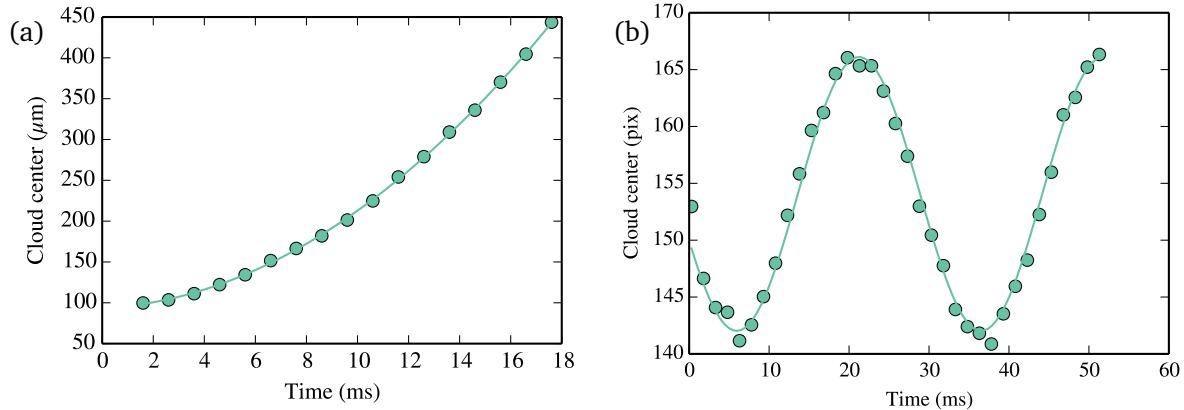


Figure 5.2: Measurement of trap parameters of the ReST trap in the weak configuration. (a) The acceleration is determined by measuring the position of the cloud as a function of time after switching off the barrier beam. Fit to a parabola gives $a = 2.08(8) \text{ m/s}^2$. (b) Oscillations in x are set up by briefly shifting the trap center to measure the trap frequency. A fit to a sinusoid gives $\omega_x = 2\pi \times 32.7(3) \text{ Hz}$.

5.2.2 Ground state properties

A glance at Eq. 5.1 shows that unlike the case of a simple harmonic oscillator, the ReST trap has a number of length scales and energy scales associated with it. The relative magnitude of these energy

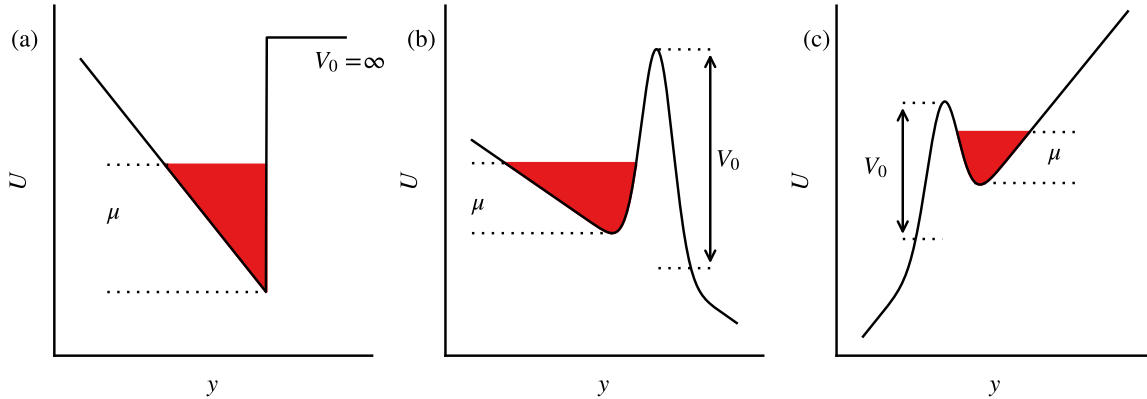


Figure 5.3: Potential energy as a function of the vertical position y in the ReST trap at $x = z = 0$. (a) The barrier is replaced by a hard wall to get an analytical expression for the chemical potential. (b) Potential energy in the weak configuration. The acceleration a due to the tilted potential is small, so the hard wall approximation is still valid. We see that the trap depth, defined as the potential energy difference between the bottom of the well and the top of the barrier, is less than V_0 due to a sag introduced by the tilt. (c) Potential energy in the tight trap. The atoms are trapped vertically below the barrier in the tight trap and tunnel upwards. Due to the high acceleration a , the hard wall approximation breaks down in the tight configuration.

scales will determine the size and shape of the ground state of the condensate, its dimensionality and ultimately the tunneling properties. We will briefly go over these energy scales before describing the ground state properties of the condensate.

Transverse trapping: The harmonic confinement in the x and z directions have an energy scale $E_{\perp} = \hbar\omega$ and a length scale $l_{\perp} = \sqrt{\hbar/m\omega}$ corresponding to the energy and width of the Gaussian ground state. The transverse trap frequencies in the weak and strong configurations are $\omega_x = 2\pi \times 32.7$ and $\omega_x = 2\pi \times 86.6$ respectively, and the energy scales are $k_B \times 1.6$ nK and $k_B \times 4.1$ nK. The corresponding length scales are $1.9 \mu\text{m}$ and $1.1 \mu\text{m}$.

Tilt: The tilt in the potential due to an acceleration a has a characteristic length scale l_0 which can be found out by equating the kinetic and potential energy terms for a wavepacket of size l_0 [113]: $\hbar^2/2ml_0^2 = mal_0$, giving us

$$l_0 = \left(\frac{\hbar^2}{2m^2a} \right)^{1/3}. \quad (5.4)$$

The corresponding energy scale $E_0 = mal_0$ is

$$E_0 = \left(\frac{\hbar^2 ma^2}{2} \right)^{1/3}. \quad (5.5)$$

The two trapping configurations have accelerations 2.08 m/s^2 and 8.4 m/s^2 which give length scales $l_0 = 0.50 \mu\text{m}$ and $l_0 = 0.32 \mu\text{m}$ respectively. Similarly, the energy scales are $E_0 = 11 \text{ nK}$ and $E_0 = 28 \text{ nK}$. l_0 is much smaller than the transverse length scale l_{\perp} , which suggests that a condensate is

pancake shaped, tightly confined in the y direction and spread out in the x and z directions, as shown in Fig. 5.1a.

Barrier: Typical barrier heights used in the experiment range from $k_B \times 100\text{ nK}$ to $k_B \times 400\text{ nK}$ and the barrier waist w_0 is $1.3\text{ }\mu\text{m}$. For a Gaussian barrier with a waist w_0 and height V_0 , the maximum force exerted by the barrier is given by

$$F_{max} = \frac{2V_0}{\sqrt{\epsilon}w_0}. \quad (5.6)$$

Chemical potential

The ground state of a weakly interacting Bose gas is described well by the Gross-Pitaevskii Equation(GPE)[24],

$$\left(-\frac{\hbar^2}{2m} \nabla^2 + V + g |\psi|^2 \right) \psi = \mu \psi, \quad (5.7)$$

where μ is the chemical potential of the condensate and $g = 4\pi\hbar^2 a_s/m$ characterizes the two-body interaction strength. a_s is the s-wave scattering length. The solution of the GPE minimizes the energy functional

$$E[\psi] = \int d^3r \left\{ \frac{\hbar^2}{2m} |\nabla\psi|^2 + V |\psi|^2 + \frac{g}{2} |\psi|^4 \right\}. \quad (5.8)$$

The three terms appearing in the energy functional correspond to the kinetic energy (K.E), potential energy (PE) and interaction energy (I.E) respectively.

In a regime where the interaction energy dominates over the kinetic energy, the ground state can be described by the Thomas-Fermi approximation, which neglects the kinetic energy term in Eq. 5.7. The density $|\psi|^2$ is given by

$$|\psi_{TF}|^2 = \begin{cases} (\mu - V)/g & \text{for } \mu - V > 0 \\ 0 & \text{otherwise} \end{cases} \quad (5.9)$$

Integrating Eq. 5.9 over all space gives us a relationship between the chemical potential and the total atom number

$$N = \int d^3r \frac{(\mu - V)}{g} \mathcal{H}(\mu - V), \quad (5.10)$$

where \mathcal{H} is the Heaviside step function. This integral does not have an analytical solution for the potential described by Eq. 5.2 and it has to be evaluated numerically. However, when we replace the complicated barrier potential V_b with an infinitely sharp and high wall, we can get an analytical expression.

Hard Wall Approximation

The potential for a hard wall is given by

$$V(x, y, z) = \begin{cases} \frac{1}{2}m\omega_x^2x^2 + \frac{1}{2}m\omega_z^2z^2 - may & \text{for } y < 0 \\ \infty & \text{for } y > 0 \end{cases} \quad (5.11)$$

Plugging this in Eq. 5.10, we get,

$$N = \frac{1}{g} \int_{-l_y}^0 dy \int_0^{r_m} \left[(\mu + may) - \frac{1}{2}m\bar{\omega}^2 r^2 \right] 2\pi r dr \quad (5.12)$$

where $\bar{\omega} = \sqrt{\omega_x \omega_z}$, $l_y = \mu/ma$, and $r_m^2 = 2(\mu + may)/m\bar{\omega}^2$. Evaluating the integral we get the chemical potential

$$\mu = \left(\frac{3gNm^2a\bar{\omega}^2}{\pi} \right)^{1/3}. \quad (5.13)$$

The chemical potential can be expressed as a function of the scattering length a_s instead of g . This gives us

$$\mu = \{12(\hbar\bar{\omega})^2(ma)(Na_s)\}^{1/3}. \quad (5.14)$$

The Thomas-Fermi radius in the transverse directions is given by $r_{x,z} = \sqrt{2\mu/m\omega_{x,z}^2}$ and the length of the condensate in the y direction is given by $l_y = \mu/ma$.

An experimentally relevant quantity is the interaction energy, or mean field energy, per particle. The width of a condensate after time of flight is used to extract this quantity. It is given by

$$\epsilon_{\text{int}}/N = \frac{1}{2} \int \frac{g}{N} |\psi|^4 dV. \quad (5.15)$$

Using Eq. 5.9 and Eq. 5.13, we get

$$\epsilon_{\text{int}}/N = \frac{\pi}{gN} \int_{-y_m}^0 dy \int_0^{r_m} \left[\mu + may - \frac{1}{2}m\bar{\omega}^2 r^2 \right]^2 r dr. \quad (5.16)$$

Evaluating the integral, we find that

$$\epsilon_{\text{int}}/N = \frac{\mu}{4}. \quad (5.17)$$

A similar integral for the potential energy can be evaluated to get

$$\epsilon_{\text{pe}}/N = \frac{\mu}{2}. \quad (5.18)$$

Extracting the chemical potential

The chemical potential is extracted from the width of the condensate after time of flight. The condensate is initially pancake shaped with the tight axis along y and an aspect ratio of

$$\gamma = \frac{2r_{\text{TF}}}{l_y} = 2 \left[\frac{2m^2 a^5}{3\hbar^2 \omega^8 N a_s} \right]^{1/6}. \quad (5.19)$$

Unlike the case of a 3D harmonic oscillator, the aspect ratio is dependent on the atom number N and increases for low atom number. This is due to different scaling of the size of the condensate with μ in the vertical and transverse directions ($l_y \propto \mu$, whereas $r_{\text{TF}} \propto \sqrt{\mu}$). In both trap configurations, $\gamma \sim 10 - 15$ is quite high, making the expansion of the condensate highly anisotropic. During time of flight, the condensate explodes in the y direction, initially converting its interaction energy into kinetic energy[25, 114, 115] while the width in the transverse direction does not change significantly.

We study the expansion of the condensate in the two trapping configurations in slightly different ways. In the weak configuration where the net acceleration is downwards, during time of flight the barrier beam is abruptly turned off, but the magnetic waveguide is kept on. This causes the condensate to expand vertically in the magnetic waveguide and accelerate downward with an acceleration of 2 m/s^2 . Since the acceleration is about 5 times smaller than g , the acceleration due to gravity, we get about $\sqrt{5}$ times more expansion time for the same distance traveled. We take an absorption image after 40 ms time of flight. The higher time of flight increases our precision in measuring the chemical potential.

In the tight configuration, the net acceleration is upwards. Switching off the barrier causes the condensate to accelerate towards and eventually reach the B -field center. We have tried reducing the magnetic field gradient so that the condensate accelerates downward instead of going up. However, the large time constant of ~ 100 ms of the current driver for the quadrupole coils(see Sec. 3.3.3) prevents us from changing the acceleration fast enough. Instead we opt to switch off the barrier beam and the magnetic trapping simultaneously and take an absorption image after 20 ms of time of flight in free space.

During time of flight, the interaction energy of the condensate is converted into kinetic energy. The total final energy ϵ_f is given by

$$\epsilon_f = \epsilon_{\text{ke}} + \epsilon_{\text{int}}, \quad (5.20)$$

where ϵ_{ke} is the initial kinetic energy, which is neglected in the Thomas-Fermi approximation. If the time of flight is large, then the density after time of flight is low and the final interaction energy can be neglected. Thus, the final kinetic energy is equal to ϵ_f . If the size of the final condensate is much larger than the initial size, the final kinetic energy per particle is given by

$$\epsilon_f/N = \frac{1}{2} m \left(\frac{\Delta y_{\text{rms}}}{t_{\text{tof}}} \right)^2, \quad (5.21)$$

where t_{tof} is the total time of flight and Δy_{rms} is the root mean squared length in the y direction, given by

$$\Delta y_{\text{rms}} = \sqrt{\langle y^2 \rangle - \langle y \rangle^2}. \quad (5.22)$$

In our experiment, the initial size $l_y \sim 2 \mu\text{m}$, whereas the final size is $\sim 100 \mu\text{m}$ (see Fig. 5.4), making Eq. 5.21 an excellent approximation. Eq. 5.21 assumes that all the interaction energy is converted to kinetic energy in the y direction, but makes no assumption about the trap geometry.

To extract Δy_{rms} from the absorption images, we rely on fitting the divided image to a two dimensional integrated Thomas-Fermi profile

$$\text{OD}(x, y) = \text{OD}_0 \times \max \left(1 - \left(\frac{x - x_0}{r_x} \right)^2 - \left(\frac{y - y_0}{r_y} \right)^2, 0 \right)^{3/2}. \quad (5.23)$$

An extra offset OD_{off} is added as a free parameter in Eq. 5.23 to account for the small mismatch between absorption and reference probe intensity (see Sec. 3.4.10).

Δy_{rms} can be calculated by evaluating the integral

$$\Delta y_{\text{rms}}^2 = \frac{\int dx dy \text{OD}(x, y) (y - y_0)^2}{\int dx dy \text{OD}(x, y)}, \quad (5.24)$$

which gives us

$$\Delta y_{\text{rms}}^2 = \frac{r_y^2}{7}. \quad (5.25)$$

Eq. 5.23 is strictly valid only for self similar expansion starting with a condensate in a parabolic trapping potential. However, we find that in practice the TF profile fits well to our data (see Fig. 5.4). A fit independent method would be to calculate the expectation values by summing over the divided image pixels:

$$\langle y^2 \rangle = \frac{\sum y_j^2 \text{OD}(x_i, y_j)}{\sum \text{OD}(x_i, y_j)}. \quad (5.26)$$

However, we have seen that this method is sensitive to small background offsets in the divided image. Some images contain atoms which have just escaped from the trap. The fit successfully ignores these atoms (see Fig. 5.4), whereas the direct method over-estimates the width in these cases.

Returning to the problem of extracting the chemical potential, from Eq. 5.7 and Eq. 5.8, we find that

$$\mu = \epsilon_{\text{ke}}/N + \epsilon_{\text{pe}}/N + 2\epsilon_{\text{int}}/N. \quad (5.27)$$

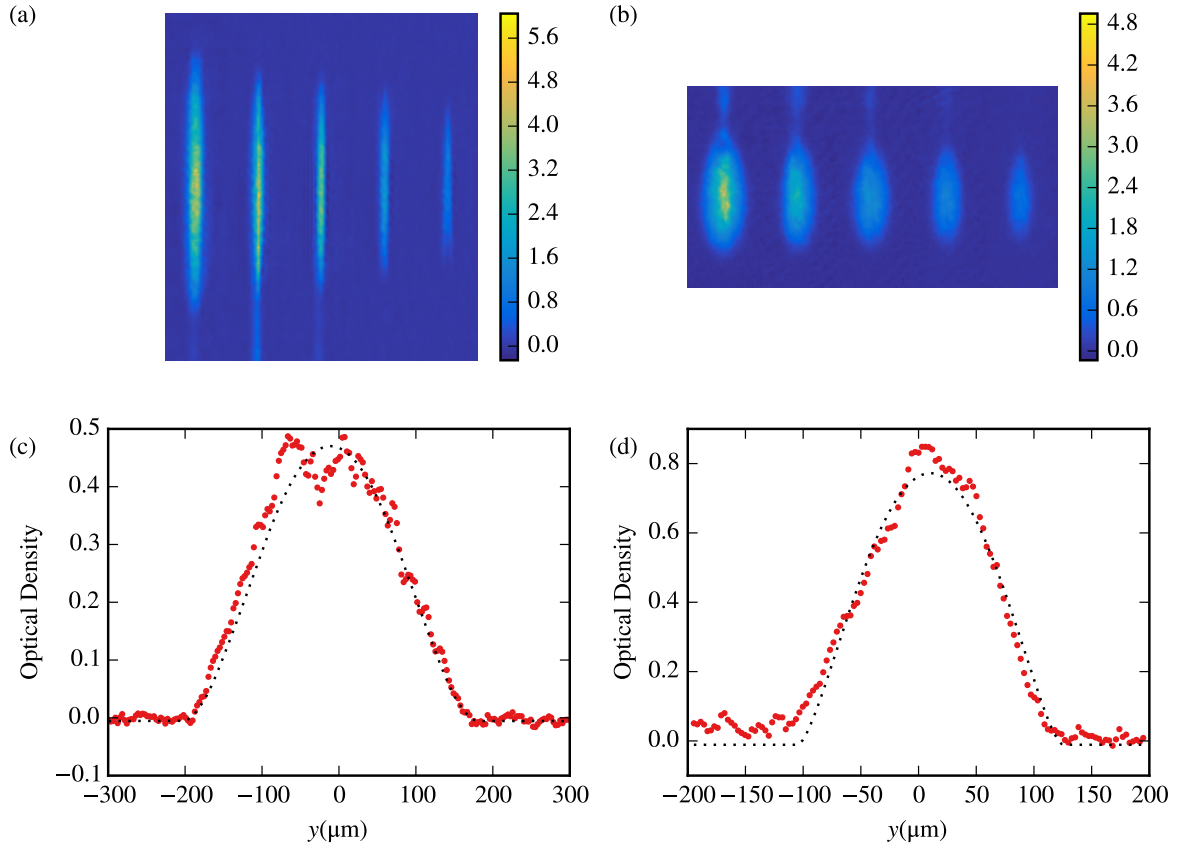


Figure 5.4: Sample absorption images and fits. (a) Absorption images of atoms 40 ms after releasing them in the waveguide starting in the weak trap configuration. A trail of atoms below the main cloud is seen in first few time steps where the atoms rapidly spill out of the trap. (b) Time of flight images in the tight configuration. Both the barrier beam and the magnetic waveguide are switched off in this configuration. Note that the trail of atoms is seen escaping upwards since the atoms are trapped below the barrier beam. (c,d) Fits of the absorption images to a 2D Thomas-Fermi profile. The fit successfully ignores the spilt atoms.

Combining this with Eq. 5.17, Eq. 5.20, and Eq. 5.21, we get

$$\begin{aligned}\mu &= \epsilon_{\text{ke}}/N + \epsilon_{\text{pe}}/N + 2\epsilon_{\text{int}}/N \\ &= \epsilon_{\text{ke}}/N + 2\epsilon_{\text{int}}/N + 2\epsilon_{\text{int}}/N. \\ &= \epsilon_{\text{ke}}/N + 4(\epsilon_f - \epsilon_{\text{ke}})\end{aligned}$$

Hence,

$$\mu = 2m \left(\frac{\Delta y_{\text{rms}}}{t_{\text{tof}}} \right)^2 - 3\epsilon_{\text{ke}}/N. \quad (5.28)$$

As usual, in the Thomas-Fermi limit, the kinetic energy term in Eq. 5.28 can be ignored. However, we will see that in the tight trap configuration the kinetic energy term is significant for low atom number.

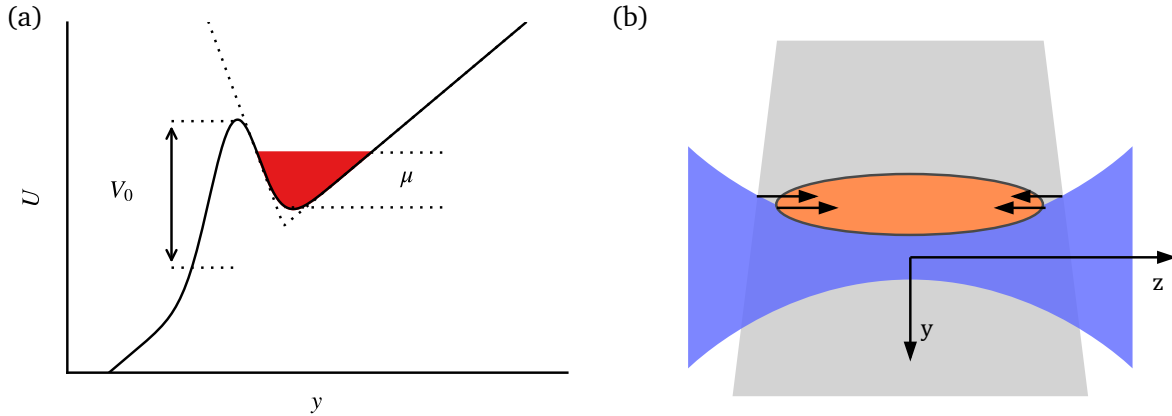


Figure 5.5: Corrections to the simple hard-wall model. (a) The barrier potential is replaced with a tilt shown in dotted lines. (b) The diffraction of the barrier beam as it propagates along the z direction provides additional confinement along the z direction.

Validity of the Thomas Fermi and hard wall approximation

The chemical potential formula in Eq. 5.13 is as valid as the approximations that went into deriving it. These approximations are: ignoring the kinetic energy term, and replacing the barrier potential with a hard wall. In this section we will examine the conditions when these approximations break down and derive corrections to the chemical potential formula.

The hard wall formula assumes that the potential jumps sharply at $y = 0$. This is valid when the force exerted by the barrier F_b is much larger than the force due to the tilt: $F_b \gg ma$. From Eq. 5.6, we get the condition

$$\frac{2V_0}{\sqrt{e}w_0} \gg ma. \quad (5.29)$$

In the experiment, this approximation is valid only for the weak configuration where the acceleration a is small. A simple fix for this is to replace the hard wall with a slope (see Fig. 5.5). The acceleration due to this slope is given by

$$a_b = \frac{2V_0}{\sqrt{e}mw_0} - a \quad (5.30)$$

It can be shown that all of the analysis for the hard wall potential is still valid provided the acceleration a is replaced by a reduced acceleration \bar{a} , given by

$$\bar{a} = aa_b / (a + a_b) = a \left(1 - \frac{\sqrt{e}ma w_0}{2V_0} \right). \quad (5.31)$$

The chemical potential formula is the same as in Eq. 5.14, but with a replaced by the reduced acceleration \bar{a} :

$$\mu = \left\{ 12(\hbar\bar{\omega})^2(m\bar{a})(Na_s) \right\}^{1/3}. \quad (5.32)$$

This results in a 7.5% reduction in the acceleration in the weak trapping configuration and 32%

reduction in the tight configuration.

An additional correction of a few percent arises due to the diffraction of the barrier beam away from the focus (see Fig. 5.5). Since the additional confinement introduced by the barrier beam is not harmonic, it is hard to estimate the corrections analytically and one has to resort to numerically calculating the chemical potential.

The kinetic energy term in Eq. 5.7 can be neglected when $\mu \gg E_0$, where E_0 is the energy scale of the tilt potential (see Eq. 5.5). For the first trapping configuration, this is an excellent approximation and the TF formula fits well with the data. However, for the second configuration where the acceleration is large, the kinetic energy has a significant contribution, especially for low atom numbers. For very low atom numbers, the interaction energy is small and can be treated perturbatively. However, in our experiment, we are in the intermediate regime, where the kinetic energy term has a small, but significant contribution. Various theoretical approaches have been developed to estimate the chemical potential in this regime. These include using a variational approach with a trial ansatz[24, 116], evaluating the kinetic energy near the classical turning points[113], and modifying the Thomas-Fermi solution to account for the zero-point energy[117, 118]. While these approaches provide some insight into the scaling behaviour of the kinetic energy term, they are quite cumbersome to evaluate, especially for the our complicated trapping potential. Hence, we choose to evaluate the chemical potential numerically instead of using analytical approximations.

An additional complication due to the kinetic energy term is that the chemical potential cannot be calculated simply from the width of the condensate after time of flight. Additional information about the dependence of the initial kinetic energy on the chemical potential is required (see Eq. 5.28). We resort to numerical results to obtain this relation. For the weak trapping configuration, the kinetic energy correction is about 1-2nK and can be ignored. For the tight configuration, the correction is 3-5nK (see Fig. 5.6), and is included as a correction to the chemical potential obtained from the width of the condensate(see Eq. 5.28). In Sec. 5.4.1, we will see that the measured chemical potential agrees well with the theory described here.

5.2.3 Trap depth and effective barrier width

Owing to the complicated trap geometry, the trap depth is not simply the barrier height V_b , but depends on the trap parameters a and ω_z , as well as the barrier Rayleigh range z_R . The tilt a reduces the trap depth, in a manner similar to attractive optical traps. In optical traps, a tilt causes the trap center to sag and decreases the trap depth. For repulsive barriers, a tilt shifts the peak of the barrier uphill and decreases the effective barrier height(see Fig. 5.3).

The barrier height is proportional to the intensity of the barrier beam. Consequently, it is maximum where the beam is focused and decreases off-focus as the barrier beam diverges. If not for the transverse trapping due to the magnetic waveguide, the atoms would simply travel off-focus until a point where the barrier height has dropped enough so that they can escape. An interplay between the diverging barrier beam and the parabolic trapping potential creates a saddle point, which is the weakest point in the trap (see Fig. 5.1). We define V_{saddle} as the potential difference between the

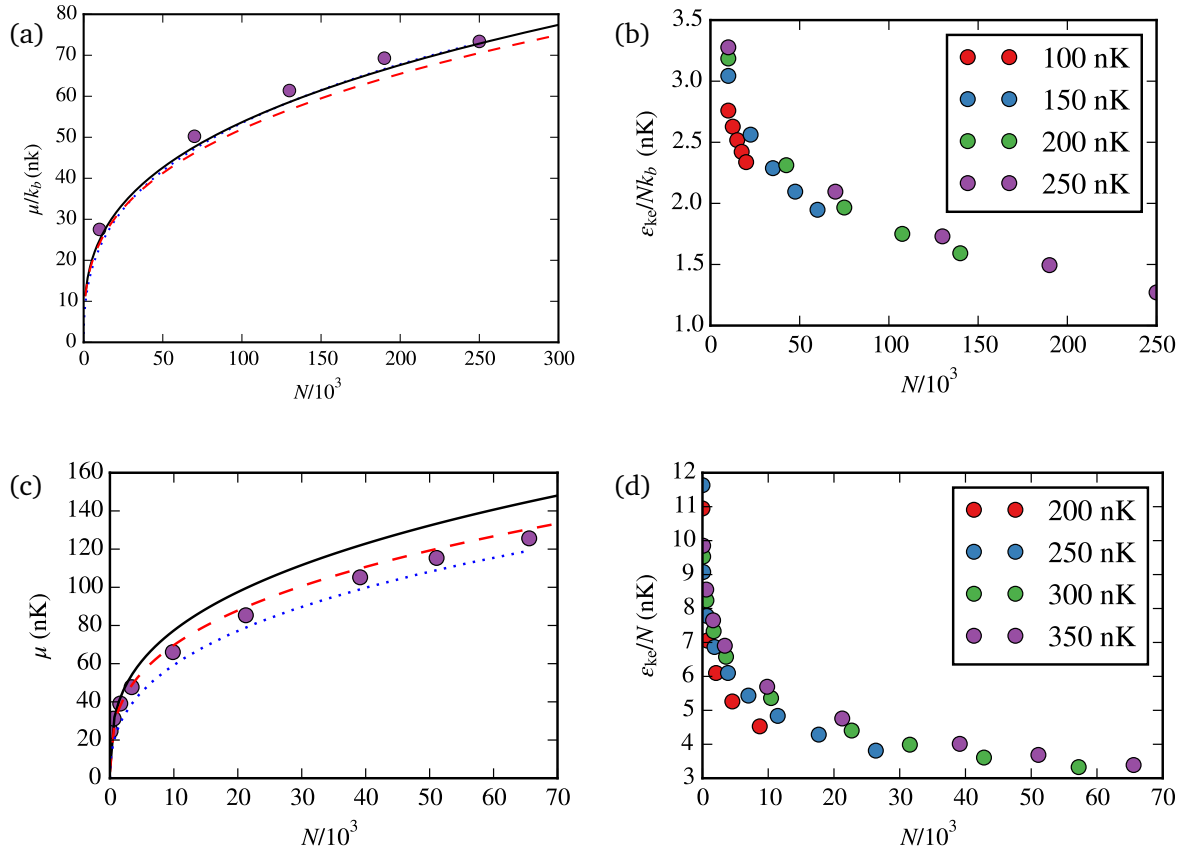


Figure 5.6: Estimating the chemical potential in the ReST trap. (a), (c) Chemical potential as a function of atom number in the weak and tight trapping configurations respectively. Black solid line is calculated using the hard wall approximation (see Eq. 5.13), dashed red line includes corrections due to the finite size of the barrier (see Eq. 5.31), blue dotted line is the Thomas-Fermi chemical potential calculated numerically for the full potential and purple dots are calculated by numerically finding the ground state of the full 3D potential using the split-step operator method. (b), (d) Kinetic energy contribution to the chemical potential as a function of number of atoms for various barrier heights. These are calculated by numerically solving the full 3D GPE equation using imaginary time propagation. As the number of atoms increases, the kinetic energy contribution decreases, increasing the accuracy of the Thomas Fermi approximation.

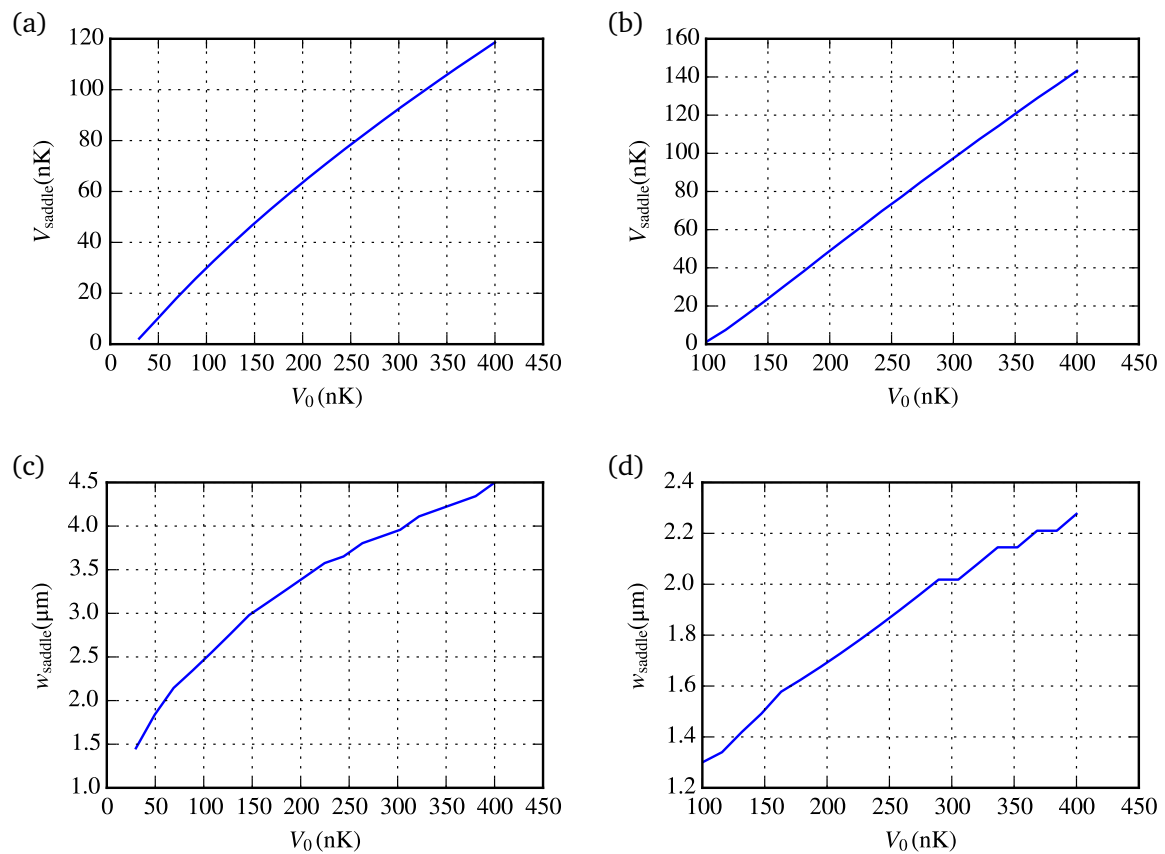


Figure 5.7: Trap depth V_{saddle} and effective barrier width w_{saddle} as a function of the barrier height V_0 . (a), (c) correspond to the weak trapping configuration and (b), (d) correspond to the tight trapping configuration.

bottom of the trap and the saddle point.

Fig 5.7 shows the trap depth V_{saddle} as a function of V_0 for both the trapping configurations. In the weak configuration, the reduction is primarily due to the saddle point being highly off-focus due to the weak transverse confinement, with a small reduction caused due to sag from the tilt. In the tight confinement, the reduction is mostly due to sag, since the tilt is quite high.

The position of the saddle point affects the effective width of the barrier region through which the atoms tunnel out. Fig. 5.7 shows the waist at the saddle point as a function of V_0 . The effective waist is higher in the weak configuration. This was a motivation to study the escape dynamics in both the trap configurations, since we could study tunneling through two different barrier widths.

It should be noted that the effective width is calculated using the intensity profile of an ideal Gaussian beam. In reality, our beam is Gaussian only close to the focus and develops complicated fringes away from the focus (see Fig. 3.15). This is a characteristic feature of residual spherical aberrations limited systems[119]. Thus the predictions in Fig. 5.7 for both the trap depth and the barrier width could be off significantly for the weak trapping configuration.

5.2.4 Tunneling rate

Let us first review the basics of single particle tunneling. Consider a particle trapped in a one-dimensional trap, similar to the one shown in Fig. 5.3(b). A semi-classical approach to calculating the tunneling rate is to assume that the particle is bouncing in the trap, and hits the barrier once every time interval τ . If the particle penetrates the barrier with a probability P , then the tunneling rate is given by $\Gamma = P/\tau$. Both τ and P depend on the shape of the trapping potential and the energy of the particle. If the trapping potential can be approximated as being harmonic, then $\tau = 2\pi/\omega$, where ω is the trapping frequency. The tunneling probability, in the WKB limit, is calculated from the action integral, and is given by $P = e^{-2S}$, where

$$S = \int_{x_1}^{x_2} \frac{\{2m(U(x) - E)\}^{1/2}}{\hbar} dx. \quad (5.33)$$

Here $U(x)$ is the trapping potential, E is the energy of the particle, and x_1, x_2 are the classical turning points.

Our experiment differs from the single particle case in two ways: the trapping potential is three dimensional and non-separable, and we have an interacting cloud of atoms. The one dimensional model can be extended to higher dimensions by calculating the action S through an optimally selected one-dimensional path[120]. Determining this optimal path is a non-trivial task; however it passes through points which minimize S , which in our case are points close to the saddle points.

The effect of the interactions can be understood as a modification of the trapping potential due to inter-atomic interactions. Since $\mu = (\partial E / \partial N)_{S,V}$, an escaping particle carries away energy equal to the chemical potential. Hence, as a first approximation, we can replace E in Eq. 5.33 with μ . This approximation would be valid on the far side of the barrier where the atomic density is low and the mean-field energy can be neglected. On the entrance face, there would be corrections over a length

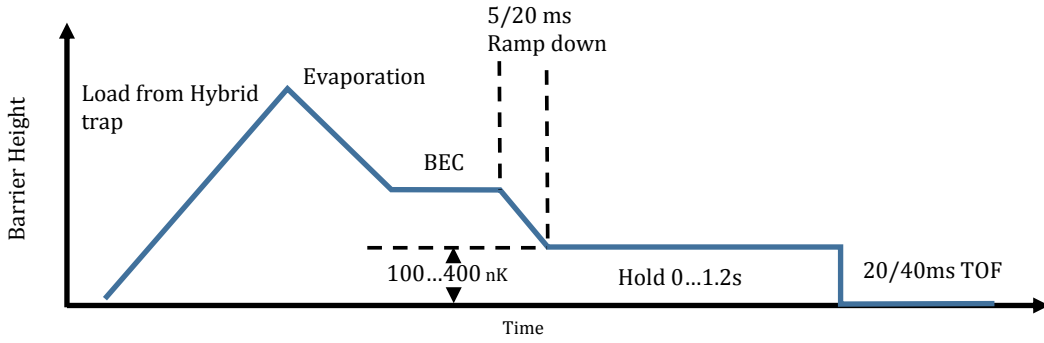


Figure 5.8: Barrier height ramp used to study tunneling out of a quasi bound state.

scale corresponding to the healing length of the condensate ξ , given by

$$\xi = \sqrt{\frac{\hbar^2}{2mg n_{\text{loc}}}}. \quad (5.34)$$

Here n_{loc} is the local condensate density near the classical turning point. While we do not calculate theoretically the expected tunneling rates, the point of this section is to illustrate that the tunneling rate has an exponential dependence on the action S as given in Eq. 5.33. In the small range of μ in which we observe tunneling, S can be assumed to vary linearly with μ . In the same range of μ , the round trip time τ does not vary significantly, justifying our claim that the tunneling rate decreases exponentially with decreasing μ .

Since Eq. 5.33 is an integral over the forbidden region, we expect the tunneling rate to be dependent exponentially on the barrier width as well. This means that for a given barrier width, the range of μ for which we see an appreciable tunneling rate is proportional to the barrier width. In the two trapping configurations considered in the experiment, the weak configuration has a factor of 2 larger effective width. Hence, we would expect to see tunneling in a smaller range of μ as compared to the tight configuration.

5.3 Experimental procedure

The experiment begins with a cloud of ^{87}Rb atoms in the $|F = 2, m_F = 2\rangle$ ground state evaporatively cooled close to degeneracy in a hybrid trap(see Sec. 3.8.4). Initially the magnetic field gradient is set to cancel gravity. The cloud is then adiabatically transferred to the REST trap by ramping up the barrier height V_0 , while ramping down the power in the hybrid trap beam in $\sim 2\text{s}$. For the weak trapping configuration, the magnetic field gradient is ramped down to 12.1 G/cm , whereas for the tight trapping configuration it is ramped up to 28.3 G/cm . Due to the small trapping volume of the REST trap, the phase space density increases during the transfer due to the dimple effect[41, 121].

We do further evaporation by lowering the barrier height to ~ 550 nK to get a pure BEC with around 500k atoms in the weak trap and 150k atoms in the tight trap. Interestingly, the initial chemical potential in both trapping configurations is similar, around 120-140 μK . The vast difference in atom number is due to the smaller trapping volume of the tight trap. Fig. 5.8 depicts the various stages during preparation.

To initiate the tunneling dynamics, the barrier height is then non-adiabatically ramped down in 20 ms for the weak trap and 5 ms for the tight trap. The condensate is held in the trap for a variable time from 0.1 ms to 1.2 s. The trapping potentials are then abruptly turned off and the cloud is imaged after time-of-flight(TOF) expansion. The two trapping configurations are imaged in slightly different ways, as described in detail in Sec. 5.2.2. Briefly, all trapping potentials are turned off for the tight trapping configuration and the cloud is imaged after 20 ms TOF. For the weak configuration, the magnetic waveguide is kept on, to increase the total time of flight to 40 ms

We image on the $F = 2 \rightarrow F = 3$ cycling transition using σ^+ light propagating along z and correct for probe saturation effects[34, 35] to ensure accurate atom number calibration. The atom number calibration is verified by measuring the critical temperature in the hybrid trap which agrees within 2% with the theoretically predicted value (see Sec. 3.8.4). As additional verification, the expansion of a pure BEC in the hybrid trap is studied as a function of the number of atoms, and the observed cloud size after the expansion agrees well with the scaling solution (see Sec. 3.8.4). Ensuring absolute atom number calibration is important for quantitative comparison of the chemical potential versus atom number relationship with the prediction in Sec. 5.2.2.

Barrier alignment

Alignment of the position of the barrier focus with the center of the magnetic waveguide is another critical factor that strongly affects the escape dynamics. The barrier is aligned by optimizing the transfer efficiency from the hybrid trap to the ReST trap. The alignment procedure is repeated for progressively lower initial barrier heights to maximize the sensitivity to misalignments. We ensure the alignment is within 2 μm in z direction, i.e. the barrier beam propagation direction. In the x direction where the barrier intensity is flattened within a 100 μm range (see Sec. 3.5.3), we align the center of the flattened profile with the magnetic field center to within 5 μm . The barrier position is adjusted by moving the objective lens, which is mounted on a motorized (and computer controlled) two-axis translation stage. The alignment in the y direction affects only the initial loading efficiency, and not the escape dynamics (since the potential energy goes as $V = m a y$). We align the y position manually using a micrometer with 5 μm resolution.

Atom number stability

We study the escape dynamics by monitoring the number of atoms left in the ReST trap. Since the atom number measurement is destructive, shot to shot stability of the number of atoms at the beginning of the ramp is critical to the experiment. Data runs take up to two days and it is important

to keep track of drifts in the experiment. A number of parameters have to be actively monitored while data taking. These include the spectroscopy lock points, strength of the injection lock, power in the beams, and MOT fluorescence at the end of MOT loading. Small adjustments are done after each data set to correct for drifts. Additionally, calibration shots measuring the number of atoms at zero hold time are taken after every 20-30 runs. Within a data set, the hold times are randomized so that systematic slow drifts in the initial atom number turn to random errors. Within a 4 hour data set, the initial atom number N_0 is stable to 10%, i.e. $\Delta N_0/N_0 = 10\%$, where ΔN_0 is the standard deviation of all the calibration shots.

Barrier height stability

The tunneling rate depends exponentially on the trap depth V_0 , which is proportional to the power of the barrier beam. To stabilize the barrier power, we use active feedback by monitoring a small fraction of the beam power picked off at a dichroic mirror (servo PD in Fig. 3.14). A second photodiode picks off the power transmitted through the vacuum chamber (monitor PD in Fig. 3.14) and is monitored on an oscilloscope, which saves traces for each shot. Drifts in the barrier power within a data set is less than 2%.

Barrier height calibration

The barrier height V_0 is proportional to the intensity of the barrier beam. The intensity is calculated from careful power measurements, and measuring losses through all the optics. To determine the intensity from the power, the barrier beam beam is assumed to be Gaussian in y direction. Since it is being scanned in the x direction, we use the imaging system to determine the intensity profile of the barrier in the x direction.

An initial concern was a slight polarization dependent transmission through a dichroic mirror. To correct for that, the servo PD was installed *after* the dichroic mirror(see Fig. 3.5.3).

The AC Stark shift, and hence the barrier height V_0 is calculated from the intensity by considering the $5P$ and $6P$ excited states and includes the counter rotating term. The AC Stark shift is independent of the polarization, since the barrier beam is propagating in the z direction, whereas the quantization axis set by the magnetic field is along y . Thus, the electric field projection along σ^+ and σ^- directions is equal, canceling the already small polarization dependence of the Stark shift for large detunings[105].

5.4 Results

The experimental quantities measured are the number of atoms left in the ReST trap and the width of the cloud after TOF as a function of the hold time. This is done for different barrier heights in both the weak and the tight trap configurations. The chemical potential μ and the decay rate Γ are extracted from these measurements.

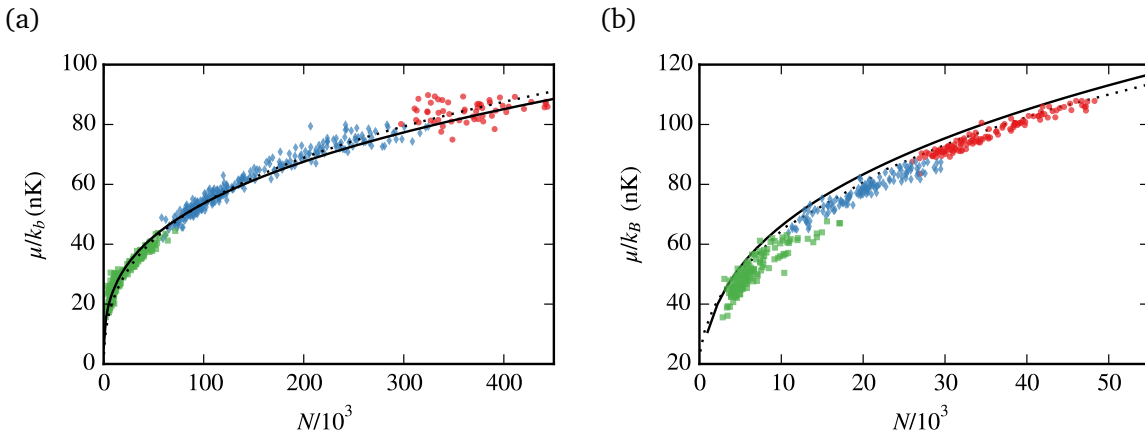


Figure 5.9: Chemical potential μ of the condensate as a function of the number of atoms N for the two trapping configurations. (a) Chemical potential in the weak configuration for barrier heights $V_0 = 460(30)$ nK (red circles), $V_0 = 260(20)$ nK (blue triangles) and $V_0 = 170(11)$ nK (green squares). Black solid line is an estimate using Eq. 5.32 and the dotted line is the chemical potential calculated using the full 3D potential for a barrier height of 350 nK. (b) Chemical potential in the tight configuration for barrier heights $V_0 = 330(35)$ nK (red circles), $V_0 = 290(30)$ nK (blue triangles) and $V_0 = 250(25)$ nK (green squares). Black solid line is an estimate using Eq. 5.32 and the dotted line is a numerical solution of the 3D Gross-Pitaevskii Equation for a barrier height of 300nK.

5.4.1 Chemical Potential

Fig. 5.9 shows the chemical potential of the condensate for three different barrier heights in both the weak and tight trapping configuration. The method for extracting the chemical potential from the width of the condensate is outlined in Sec. 5.2.2. We see that in both cases the data shows good agreement with the full 3D GPE calculations. In the weak trapping configuration, the simple hard wall approximation (Eq. 5.32) correctly predicts the chemical potential. In the tight configuration, the data deviates from the prediction of Eq. 5.32, since the approximations involved in the derivation (ignoring kinetic energy, approximating the trap by a V-shaped potential) break down.

It should be emphasized that the solid and dashed lines in Fig. 5.9 are not fits, but predictions based on measured trap parameters.

5.4.2 Background decay rate

To characterize loss processes other than escape through the barrier, we study the decay from a trap with a high barrier height of 460 nK (see Fig. 5.10). At this barrier height, escape due to classical spilling and tunneling is negligible. We find that in the 1.5 s observation time, the decay is exponential with a decay rate of $\Gamma_{bg} = 0.31(2) \text{ s}^{-1}$, which we take as our background decay rate.

This rate is consistent with three-body recombination rate, given by $\Gamma_{3b} = L\langle n^2 \rangle$, where L is the three-body decay constant. For the REST trap in the Thomas-Fermi limit, we can show that $\langle n^2 \rangle = 3n_0^2/10 = (3/10)(\mu/g)^2$, where n_0 is the peak density. Using the value for L from Ref. [52]

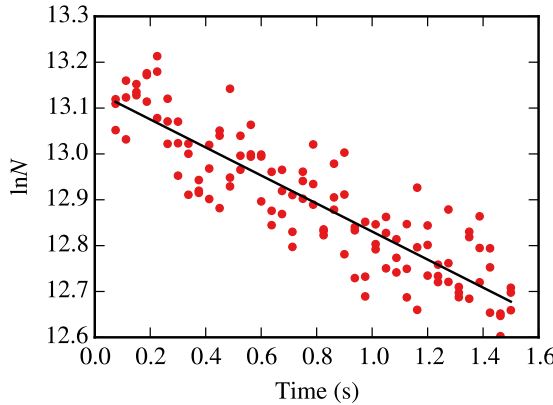


Figure 5.10: Natural logarithm of the number of atoms left in the trap as a function of the hold time in the trap for a high barrier height of 460 nK. A fit to a straight line gives a background decay rate of $\Gamma_{\text{bg}} = 0.31(2) \text{s}^{-1}$.

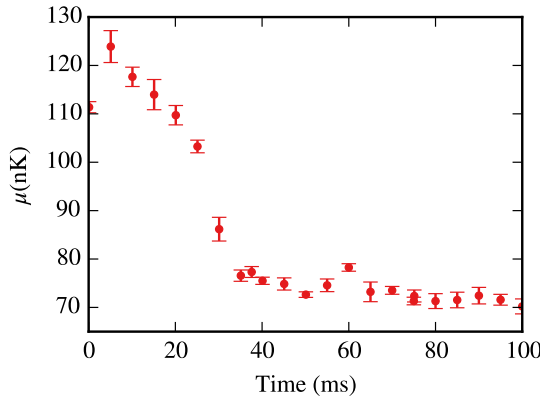


Figure 5.11: Transition from spill to tunneling indicated by the kink at ~ 30 ms.

and the measured chemical potential $\mu = 92$ nK, we find that $\Gamma_{3b} = 0.34(9) \text{s}^{-1}$. We do not find any discernible thermal component emerge during the hold, which means that any thermal atoms created escaped. The background loss rate also sets an upper bound on the loss rate due to heating.

5.4.3 Classical spill

After preparing a condensate in the ReST trap, the escape dynamics are initiated by non-adiabatically lowering the barrier height. This is done in 20 ms for the weak trapping configuration and 5 ms in the tight trapping configuration. The initial non-adiabatic lowering of the barrier height causes the condensate to rapidly expand and spill over the two saddle points of the trap, as depicted in Fig. 5.1b. The expansion, which is driven by the interaction energy of the condensate, occurs over a time scale $\tau = 1/\omega$, where ω is the transverse trapping frequency. The ramp-down time is chosen to be comparable to $1/\omega$, so that it is slow enough to cause minimal sloshing in the trap after the

ramp down, but fast enough so that we can still observe tunneling after the ramp down.

Fig. 5.11 shows the chemical potential μ at early times. The spill out causes μ to rapidly drop in the first 30 ms, after which it stabilizes. A sharp kink in the chemical potential vs time data signifies the transition from classical spill to tunneling. We expect the chemical potential at the transition point, μ_{trans} to be equal to V_{saddle} . V_{saddle} is the trap depth estimated from the barrier power and the trap geometry. We will see in the next section that $\mu_{\text{trans}} \sim V_{\text{saddle}}$ in the tight configuration. In the weak configuration μ_{trans} is 15-20% less than V_{saddle} , which indicates a systematic overestimation of V_{saddle} in the weak configuration. Indeed the tunneling dynamics also agree with simulations with a lower barrier height. Possible sources of the error are discussed.

5.4.4 Tunneling

Next we turn our attention to the tunneling dynamics. Fig. 5.12(a) and Fig. 5.14(a) plot the number of atoms left in the trap as a function of the hold time in the weak and tight configurations respectively. Each data point is the average of 5 shots and the error bars indicate the statistical error. $t = 0$ on the plots corresponds to the end of the barrier ramp down. Three data sets corresponding to different barrier heights V_0 are shown. Overlaid with the data are results of full 3D GPE simulations that match most closely with the data. Only the barrier height is varied in the simulations, all the other parameters are obtained from experiment and are fixed. Details about the simulations can be found in Sec. 5.4.5.

The atom number is plotted on a semi-log plot. An exponential process, characterized by a constant decay rate, would appear as a straight line on a semi-log plot, whereas here we see a dramatic decrease of the decay rate with time. The decay rate, defined as

$$\Gamma = -\frac{1}{N} \frac{dN}{dt} = -\frac{d \log N}{dt}, \quad (5.35)$$

is calculated by numerically differentiating the data. To avoid high frequency noise being amplified by the differentiation, we fit sets of 5 consecutive points to a parabola and evaluate the slope at the middle point. This is equivalent to low pass filtering the data before taking the derivative[122]. The decay rate is plotted as a function of the chemical potential in Fig. 5.12(b) and Fig. 5.14(b) for the weak and tight trapping configurations respectively. Error bars on the decay rate are obtained from the fit and the error bar in the chemical potential is statistical. Fig. 5.13 and Fig. 5.15 compare the decay rates obtained from the data with 3D GPE simulations.

A number of interesting trends are seen in the data. The N versus t plots show a highly non-exponential decay, with the decay rate mostly decreasing with time. Fig. 5.12(a) and Fig. 5.14(a) compare the N versus t data with 3D GPE simulations. We see that in the tight configuration, simulations with barrier heights in a 10 nK range around the expected barrier height V_0 match reasonably well with the data. The agreement in the weak configuration, on the other hand is poor. Simulations that show the same trend as the data have consistently lower barrier heights as compared to the estimated height V_0 by about 30-40 nK.

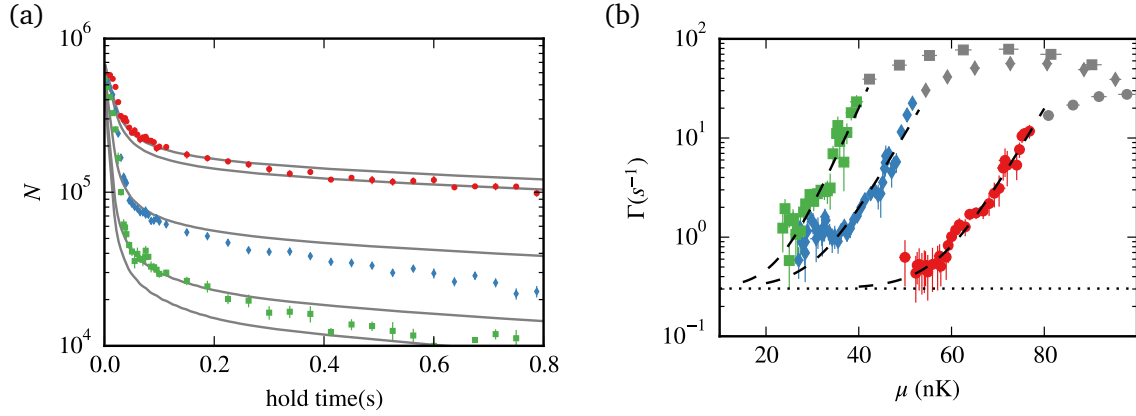


Figure 5.12: Escape dynamics in the weak trapping configuration. (a) Number of atoms N left in the trap after a hold time t for barrier heights of $V_0 = 260(20)$ nK (red circles), $V_0 = 190(13)$ nK (blue diamonds) and $V_0 = 170(11)$ nK(green squares). Solid gray lines are results of 3D GPE simulations for a barrier height of 120, 130, 140, 210, and 220 nK from bottom to top. Only the first 0.8s are shown here since the decay rate is close to the background decay rate afterwards. (b) Decay rate Γ as a function of the chemical potential μ . Color codings are the same as in (a) Horizontal dotted line indicates the background decay rate. The dashed line is a fit to the function $\Gamma = \Gamma_{\text{bg}} + \exp(\alpha + \beta\mu)$. Data points shown in gray are not used for fitting, and correspond to classical spilling. Refer to Fig. 5.13 for a comparison of the decay rates with simulations.

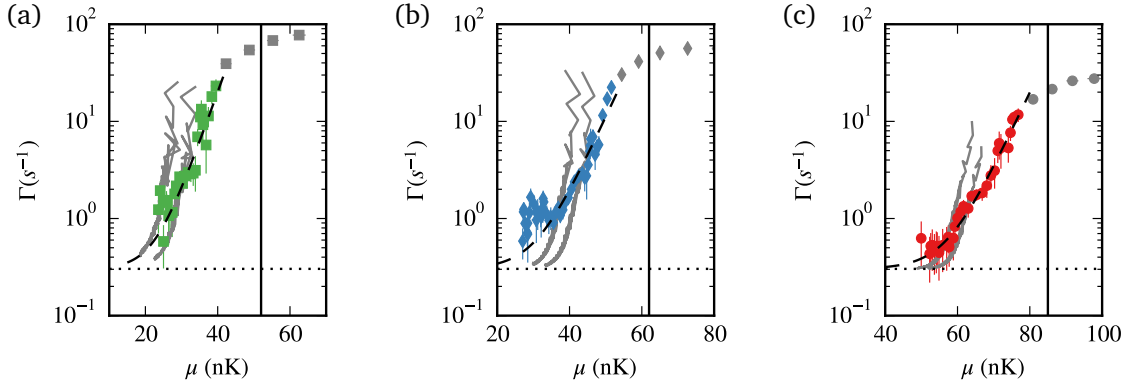


Figure 5.13: Decay rate Γ as a function of the chemical potential μ in the weak trapping configuration. Gray lines are results of 3D GPE simulations. Horizontal dotted line indicates the background decay rate. Vertical solid line indicates the point when μ is equal to the estimated trap depth V_{saddle} . (a) $V_0 = 170(11)$ nK(green squares), simulations are shown for barrier heights of 120 and 130 nK, (b) $V_0 = 190(11)$ nK, simulations are shown for barrier heights of 140 and 150 nK (c) $V_0 = 260(20)$ nK, simulations are shown for barrier heights of 210 and 220 nK.

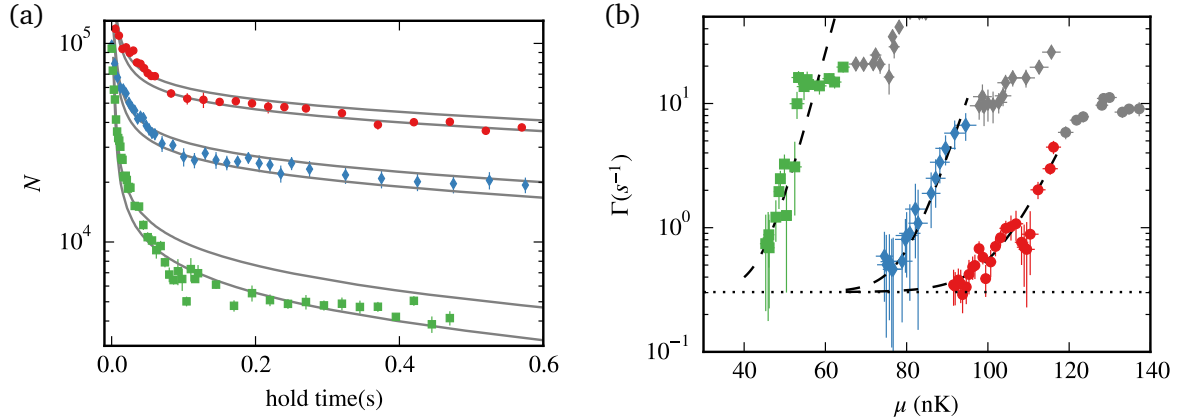


Figure 5.14: Escape dynamics in the tight trapping configuration. (a) Number of atoms N left in the trap after a hold time t for barrier heights of $V_0 = 330(35)$ nK (red circles), $V_0 = 290(30)$ nK (blue diamonds) and $V_0 = 240(25)$ nK(green squares). Solid gray lines are results of 3D GPE simulations for a barrier height of 230, 240, 290, 300, 340 and 350 nK from bottom to top. Only the first 0.6s are shown here since the decay rate is close to the background decay rate afterwards. (b) Decay rate Γ as a function of the chemical potential μ . Color codings are the same as in (a) Horizontal dotted line indicates the background decay rate. The dashed line is a fit to the function $\Gamma = \Gamma_{\text{bg}} + \exp(\alpha + \beta\mu)$. Data points shown in gray are not used for fitting, and correspond to classical spilling. Refer to Fig. 5.15 for a comparison of the decay rates with simulations.

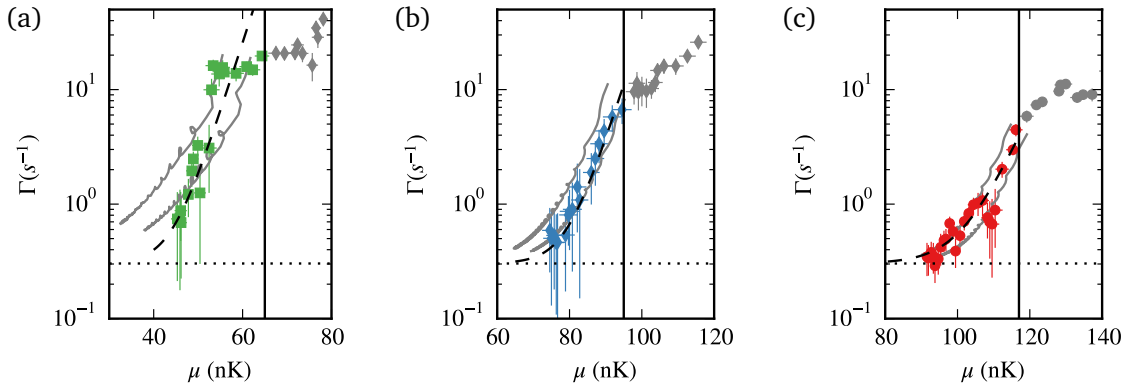


Figure 5.15: Decay rate Γ as a function of the chemical potential μ in the tight trapping configuration. Gray lines are results of 3D GPE simulations. Horizontal dotted line indicates the background decay rate. Vertical solid line indicates the point when μ is equal to the estimated trap depth V_{saddle} . (a) $V_0 = 240(25)$ nK(green squares), simulations are shown for barrier heights of 230 and 240 nK, (b) $V_0 = 290(30)$ nK, simulations are shown for barrier heights of 290 and 300 nK (c) $V_0 = 330(35)$ nK, simulations are shown for barrier heights of 340 and 350 nK.

Based on the kink in the chemical potential versus time data (see Fig. 5.11, we identify the first ~ 35 ms to be dominated by classical spill. In addition to the μ vs t data, the transition between classical spill and tunneling can be readily seen when the decay rate Γ is plotted against μ . As seen in Fig. 5.13 and Fig. 5.15, the decay rate versus chemical potential curve shows a distinct kink. The chemical potential μ_{trans} that marks the transition between classical spill and tunneling is identified by eye and all points where $\mu > \mu_{\text{trans}}$ are showed in gray. Additionally, a solid vertical line marks the position of V_{saddle} , which is the expected trap depth. As discussed in Sec. 5.4.3, the position of μ_{trans} matches reasonable well with V_{saddle} for the tight configuration (Fig. 5.13), whereas μ_{trans} is less than V_{saddle} in the weak configuration.

As μ drops below μ_{trans} , the decay rate drops exponentially, which is a distinct signature of tunneling. In general, the relationship between Γ and μ is not a simple exponential relationship (see Sec. 5.2.4). However, in the small range of μ over which we see appreciable tunneling, the relationship can be approximated to be linear. Note that in Figs. 5.13 and 5.15, Γ vs t plotted on a log scale does have a curvature, but this is a result of the constant background decay rate added on top of the exponential dependence. To illustrate this, the data is fitted to the function

$$\Gamma(\mu) = \Gamma_{\text{bg}} + \exp(\beta + \alpha\mu) \quad (5.36)$$

and the fitted function is shown in dashed black lines.

Results of GPE simulations are overlaid with the data in Figs. 5.13 and 5.15. We see that the simulations show good agreement with data in the tight configuration. In the weak configuration, Γ drops with decreasing μ faster in the simulations than the data. This indicates that the effective width of the tunneling region in the weak configuration is smaller than in the simulations. While we do not know the reason for this anomaly, we suspect that it is due to fringes developed in the barrier beam off-focus, which would decrease the width of the tunneling region.

5.4.5 3D GPE Simulations

The escape dynamics are compared against full 3D GPE simulations, as the complicated trap geometry makes constructing effective lower dimensional theories difficult. The GPE equation is numerically solved using the split-step operator method, following the algorithm in Ref. [123]. Computations were performed on the gpc supercomputer at the SciNet HPC Consortium[124]. To speed up the computation, the solver was parallelized using MPI, with each run typically using 2 nodes (16 processes) and lasting 15 hours. The code for the solver is freely available on GitHub².

The simulations were carried out an a $128 \times 256 \times 128$ grid, with grid spacings of $(l/8, l/16, l/4)$, where $l = \sqrt{\hbar/m\omega_z}$ is the harmonic oscillator length in the z direction. $l = 2.7 \mu\text{m}$ for the weak trapping configuration and $1.6 \mu\text{m}$ for the tight trapping configuration. The time stepping was chosen to be $10 \mu\text{s}$ for the weak configuration and $3.5 \mu\text{s}$ for the tight configuration (in both cases corresponding to $10^{-3}/\omega_z$).

²https://github.com/shreyaspotnis/gpe3d_mpi_nlt

Measured trap parameters and initial atom number were used for in the simulations. The ground state was first found by imaginary time propagation in a trap with a high barrier height. Mimicking the experiment, the barrier height was then lowered using a linear ramp to a final value. Absorbing boundary conditions were added to avoid reflections of the escaped atoms from the edge of the grid. The strength of the absorber smoothly increases with distance from the barrier to avoid reflections from the absorber.

5.5 Summary and Future Directions

This chapter describes our work studying the role of inter-atomic interactions in the tunneling of a condensate out of a quasi-bound state. A novel Repulsive Sheet Trap (ReST) with a thin tunnel barrier and a controllable trap depth was developed. The ground state properties of a condensate in this trap show excellent agreement with theory. The escape dynamics of the condensate were studied in two configurations, corresponding to different effective barrier widths. In both configurations we see an exponential dependence of the decay rate with the chemical potential, which is characteristic of tunneling. The tight configuration shows good agreement with 3D GPE simulations, whereas in the weak configuration, tunneling seems to be occurring through a barrier with a width smaller than the expected value. The disagreement could be attributed to fringes developed in the barrier beam when it is off focus, which would decrease the effective barrier width. To our knowledge, this work is the first observation of tunneling of ultra-cold atoms out of a single trap well.

The development of the ReST trap raises the possibility of observing tunneling of more exotic states. The aspect ratio in the ReST trap is atom number dependent (see Eq. 5.19). For low N of around 100-1000, $\mu \sim E_0$ (see Eq. 5.4), which freezes out all the dynamics in the vertical (y) direction, making the condensate two dimensional. By scanning the barrier beam in both the x and y directions in a U shaped pattern, we could even create one-dimensional condensates. Tunneling dynamics of 1D or 2D condensates, where phase fluctuations and defects are seen[125, 126] would be an interesting direction of research. Finally, due to the trapping geometry of the REST trap, the atoms tunneling out of the two saddle points (see Fig. 5.1) recombine at a time $\pi/2\omega_z$. The contrast of the resulting interference pattern could be used as a probe of the coherence of tunneled atoms.

Chapter 6

Summary and Future Directions

The rapid progress in the field of ultra-cold atoms has opened new avenues to study quantum phenomenon. Ultra-cold atoms can be prepared in the quantum ground state of a trap and the motional and internal degrees of freedom of these atoms can be manipulated with an extraordinary degree of control. This thesis explores the tunneling properties of quantum particles using ultra-cold atoms as an ideal experimental platform, taking advantage of the flexibility offered by this system.

Two projects are described in this thesis. The first project considers tunneling of atoms in a scattering configuration, with the aim to eventually measure the tunneling time. In such a configuration, a wavepacket incident on the tunnel barrier has only one chance to tunnel through, and the question of how long a tunneling event takes does not have a simple and unambiguous answer. This project aims to measure the tunneling time by localizing a “clock” inside the barrier region, so that it ticks only when particles spend time in the forbidden region. While the tunneling time is yet to be measured, a number of experimental objectives were met. Firstly, a thin $1.3\text{ }\mu\text{m}$ tunnel barrier generated optically by focusing 405 nm light was developed, bringing us in a regime with an experimentally measurable tunneling probability (1 – 5%). To confine the atoms transversely and keep the tunneling dynamics one-dimensional, a tight atomic waveguide using broadband superluminescent diode light was developed. The broadband incoherent light creates a smooth waveguide, free of corrugations caused by interference from stray light. Raman beams operating at the 790.03 nm magic-zero wavelength which induce two photon transitions between Zeeman sublevels of ^{87}Rb atoms were developed. In a proof-of-principle experiment, the effect of tightly focused Raman beams on the spin of a condensate as it traverses through the beams was measured. Finally, delta-kick cooling was used to reduce the velocity spread of the condensate so that a larger fraction of the condensate lies within the small velocity window that has an appreciable tunneling probability.

The second project explores the role of inter-atomic interactions in the tunneling of a condensate out of a quasi-bound state. A unique trapping potential, with the thin optical barrier forming one of the walls of the trap, was developed to study this. The escape dynamics of the condensate were studied in two different trapping configurations, which correspond to different effective widths of the tunnel barrier. In both cases, the chemical potential of the condensate shows excellent agreement with theory. The decay rate of the condensate was measured by observing the number of

particles left in the trap as a function of the hold time and is strongly dependent on the chemical potential of the cloud relative to the trap depth. The decay initially is due to classical spilling over the barrier, and then transitions to quantum tunneling, with a decreasing tunneling rate with time, until finally the tunneling rate is so low that the decay is dominated by background losses. The transition from classical spill to quantum tunneling is indicated by an abrupt change in the decay rate. The results of the experiment agree reasonably well with the 3D Gross-Pitaevskii equation, which indicates that a mean-field treatment is sufficient to describe the dynamics of the system.

The experimental techniques developed during the course of this work open up new research avenues. The tightly focused Raman beams can be used to rotate the spin of only a small part of the condensate. Combined with the ability to impart a relative momentum between different spin components using magnetic field gradients, this can be used to study a variety of spin-wave phenomenon. A particularly interesting example is the case of a small spin excitation created in the bulk of the condensate. If the interactions strengths between the spin states of a condensate are approximately equal, it can be shown that within the bulk, this excitation propagates like a free particle (see Appendix C). Global rotations of the spin can be used to do a homodyne measurement by interfering the rotated component with the bulk, allowing for a direct measurement of the wavefunction. Such a technique might provide an alternate route to studying tunneling, probing the tunneling of spin waves instead of the condensate.

A second possible line of research could be to study decay due to tunneling of quasi 1D or 2D condensates. This should be possible by doing straightforward modifications to the ReST trap and a reduction in the number of atoms, as mentioned in Sec. 5.5. Finally, the existence of two tunneling points in the ReST trap raises the interesting possibility of observing interference of the tunneled atoms, which could be used to probe the coherence of tunneled atoms.

Appendices

Appendix A

Replacing the Rubidium ampoule

When replacing the Rubidium ampoule, use the following checklist to ensure all the required equipment is available:

1. Powder free Gloves. Keep a few pairs handy.
2. Torque wrench. The recommended torque maximum torque for 2-3/4" CF flanges is 144 in-lbs. We borrow a torque wrench from the mechanical workshop.
3. Nitrogen cylinder.
4. Pressure regulator. We have been borrowing one from Prof. Thywissen's lab.
5. 1 CF Flange copper gasket, 2-3/4". Ensure that the gasket is thoroughly cleaned with methanol.
6. Rubidium ampoule.
7. Bottle of old engine oil to drop the old depleted ampoule.
8. Roughing pump.
9. T-connector.
10. Balloon to monitor Nitrogen pressure.
11. Rubber tubes.
12. Quick flanges.
13. Tongs to break the head of the ampoule.

The following procedure was used to replace the Rubidium ampoule:

- Turn off the Rubidium heater and strip off the heating tape.
- Set up the nitrogen tank and the pressure regulator as shown in Fig.[A.1](#).

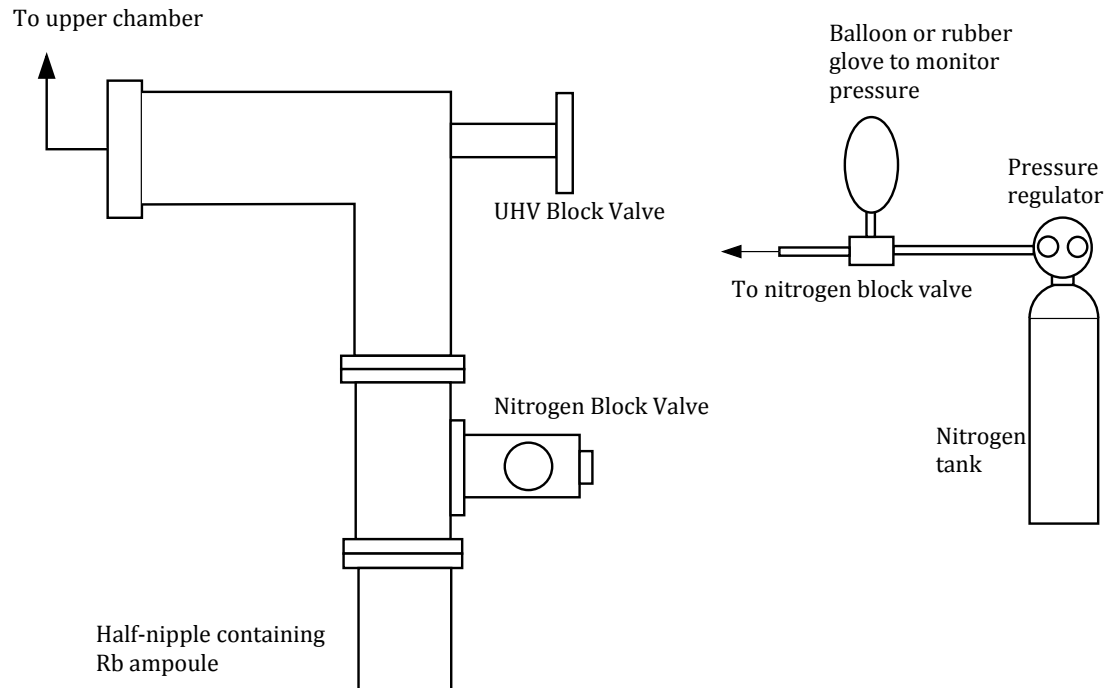


Figure A.1: Schematic of the Rubidium arm of the vacuum chamber and the nitrogen tank setup used while replacing the Rubidium ampoule.

- Close off the block valve connecting the Rubidium arm to the upper chamber.
- Hook up the nitrogen outlet via a quick flange to the nitrogen block valve. Ensure that a small amount of dry nitrogen is constantly flowing through the tube by monitoring the balloon.
- Open the nitrogen block valve to flood the Rubidium arm with dry Nitrogen. At this point the pressure in the upper chamber (monitored on the ion gauge) will rise since the UHV block valve is leaky. This is not a cause of concern.
- Open the CF flange on the half-nipple, while ensuring a constant out-flow of nitrogen.
- Optionally, insert an additional line of nitrogen close to the opened CF flange to ensure that no air enters the half-nipple.
- Remove the depleted Rubidium ampoule and drop it in a bottle of engine oil.
- Grab the narrow portion of the new ampoule with the tongs and insert it in the half-nipple, breaking the head off as you insert it. There is need to score the ampoule beforehand.
- Insert the new CF gasket, and close off the CF flange. Use the torque wrench to tighten the bolts to 144 in-lbs. Tighten the bolts incrementally in a circular pattern.
- Close off the nitrogen block valve, remove the nitrogen line and connect a roughing pump to the nitrogen block valve.
- Turn the roughing pump on and wait for a few seconds for the air in the tubes to be pumped out. Then open the nitrogen block valve, and let the roughing pump pump out Nitrogen from the rubidium arm. Pump only for a few seconds as we do not want oil from the roughing pump entering the rubidium arm.
- Close the nitrogen block valve and remove the roughing pump.
- Ensure that the ion gauge is switched off before slowly starting to open the UHV block valve. The UHV chamber will suddenly be flooded with nitrogen, which might cause the Turbo pump controller to reduce the rotation speed. This depends on how much nitrogen was pumped out by the roughing pump.
- The pressure at the backing line, monitored by TC1 and TC2 thermocouples, will also rise. This might cause the safety set-point to trigger and the gate valve connecting the roughing pump to the turbo to close. If this happens, increase the set-point so that the valve is open again.
- Slowly open the UHV block valve completely.
- Wrap the heating tape back on the half-nipple. If the set-point on the multi-gauge controller was changed, set it back to the original value.

Appendix B

Quadratic Zeeman Shift

The interaction of a magnetic dipole μ with an external magnetic field \mathbf{B} is described by the Hamiltonian $H_Z = -\mu \cdot \mathbf{B}$. The magnetic dipole moment of an atom has contributions due to the orbital angular momentum of the electron \mathbf{L} , the electronic spin \mathbf{S} and the nuclear spin \mathbf{I} , such that

$$\mu = \frac{\mu_B}{\hbar} (g_l \mathbf{L} + g_s \mathbf{S} + g_i \mathbf{I}), \quad (\text{B.1})$$

and the Hamiltonian is

$$H_Z = -\frac{\mu_B B_z}{\hbar} (g_l L_z + g_s S_z + g_i I_z). \quad (\text{B.2})$$

Here, g_l , g_s and g_i are the g-factors for the the electron orbital, spin and nuclear spin angular momentum respectively. The g-factor for the nuclear spin, g_i is typically smaller than the orbital g-factor g_l by the ratio of the nuclear mass to the electronic mass and thus can be ignored. The nuclear g-factor g_i accounts for the complex internal structure of nucleus, and for ^{87}Rb , $g_i = -9.95 \times 10^{-4}$ [33, 127]. The quadratic Zeeman shift arises due to the three g-factors being unequal and due to the hyperfine splitting

$$H_{hfs} = A_{hfs} \mathbf{I} \cdot \mathbf{J},$$

where $\mathbf{J} = \mathbf{L} + \mathbf{S}$ is the total electron angular momentum. In the absence of an external magnetic field, the total angular momentum is conserved and the Hamiltonian commutes with the total angular momentum $\mathbf{F} = \mathbf{J} + \mathbf{I}$. This can be readily seen by writing H_{hfs} as

$$H_{hfs} = \frac{A_{hfs}}{2} (\mathbf{F}^2 - \mathbf{I}^2 - \mathbf{J}^2) = \frac{A_{hfs}}{2} (F(F+1) - I(I+1) - J(J+1)). \quad (\text{B.3})$$

Additionally, the Hamiltonian is diagonal in the $|F, m_F\rangle$ basis. This is no longer the case when an external magnetic is applied. Due to $g_l \neq g_s \neq g_i$, the magnetic dipole moment μ is not parallel to \mathbf{F} and H_Z is not diagonal in the $|F, m_F\rangle$ basis. Thus, in general, one has to re-diagonalize the Hamiltonian. However, for small magnetic field strengths where the Zeeman splitting is much smaller than the hyperfine splitting, the corrections can be calculated perturbatively. To lowest order, the

correction is

$$\Delta E_{|F,m_F\rangle} = \langle F, m_F | H_Z | F, m_F \rangle. \quad (\text{B.4})$$

For the $5S$ ground state of ^{87}Rb , $L = 0$, $S = 1/2$, $I = 3/2$ and $J = 1/2$. To evaluate the first order correction, we use

$$\langle F, m_F | J_z | F, m_F \rangle = \langle F, m_F | \frac{(\mathbf{F} \cdot \mathbf{J})}{\mathbf{F}^2} F_z | F, m_F \rangle \quad (\text{B.5})$$

and get

$$\Delta E_{|F,m_F\rangle} = \mu_B g_F m_F B_z, \quad (\text{B.6})$$

where the g -factor is given by

$$g_F = g_i + (g_s - g_i) \frac{F(F+1) + S(S+1) - I(I+1)}{2F(F+1)} \approx (-1)^F / 2. \quad (\text{B.7})$$

To first order, all the m_F states are split equally. However, even for small magnetic fields on the order of 1G, second order effects are visible in Rabi oscillation data and have to be accounted for to get good agreement between theory and experiment. At higher magnetic field strengths, the quadratic Zeeman shift can be exploited to prepare the spins in a specific m_F state or to restrict Rabi oscillations to only two Zeeman levels. The second order correction to the energy is given by

$$\Delta E_{|F,m_F\rangle}^2 = \sum \frac{|\langle F' m'_F | H_z | F m_F \rangle|^2}{E' - E}. \quad (\text{B.8})$$

To evaluate this correction, we employ a few tricks specifically for ^{87}Rb . Firstly, we note that the stretched states $|F = 2, m_F = 2\rangle$ and $|F = 2, m_F = -2\rangle$ are eigenstates of the interaction Hamiltonian H_Z and thus have no quadratic (or any higher order) correction. Secondly, since the shift is quadratic in the magnetic field, flipping the quantization axis does not change the energy levels. Thus the shift for $|F, m_F\rangle$ and $|F, -m_F\rangle$ is the same. Thirdly, H_Z does not change the magnetic quantum numbers m_s or m_i . Hence, only two terms with the same m_F but different F contribute to the summation in eq.(B.8). Finally, since only two terms contribute to the summation, the shift for $F = 1$ and $F = 2$ states with the same magnetic quantum number m_F are equal and opposite, with the shift being positive for the $F = 2$ states.

With this in mind, let us evaluate the quadratic shift for the $|F = 2, m = 1\rangle$ state. The stretched state $|F = 2, m = 2\rangle$ can be written in the S_z and I_z basis as

$$|F = 2, m = 1\rangle = |m_s = 1/2, m_i = 3/2\rangle \quad (\text{B.9})$$

Applying the lowering operator $F_- = S_- + I_-$ on both sides we get

$$F_- |F = 2, m = 1\rangle = S_- |m_s = 1/2, m_i = 3/2\rangle + I_- |m_s = 1/2, m_i = 3/2\rangle.$$

Using $J_- | j, m \rangle = \sqrt{j(j+1) - m(m-1)} | j, m-1 \rangle$, we get

$$| F=2, m_F=1 \rangle = \sqrt{3}/2 | 1/2, 1/2 \rangle + 1/2 | -1/2, 3/2 \rangle. \quad (\text{B.10})$$

Since the state $| 1, 1 \rangle$ is orthogonal to $| 2, 1 \rangle$ and has the same S_z and I_z components,

$$| F=1, m_F=1 \rangle = 1/2 | 1/2, 1/2 \rangle - \sqrt{3}/2 | -1/2, 3/2 \rangle. \quad (\text{B.11})$$

Evaluating the quadratic shift for $| F=2, m_F=1 \rangle$ using Eq. (B.8), we get,

$$\Delta E_{|2,1\rangle}^2 = \frac{g_s^2 \mu_B^2 B_Z^2}{\hbar^2 \Delta E_{hfs}} |\langle 2, 1 | S_z | 1, 1 \rangle|^2 \quad (\text{B.12})$$

where ΔE_{hfs} is the hyperfine splitting. Plugging Eq. (B.10) and Eq. (B.11) in Eq. (B.12),

$$\Delta E_{|2,1\rangle}^2 = \frac{g_s^2 \mu_B^2 B_Z^2}{4 \Delta E_{hfs}} \left(\frac{3}{4} \right) \quad (\text{B.13})$$

A similar analysis for the $| F=2, m_F=0 \rangle$ state gives,

$$\Delta E_{|2,0\rangle}^2 = \frac{g_s^2 \mu_B^2 B_Z^2}{4 \Delta E_{hfs}}. \quad (\text{B.14})$$

Generalizing this for the entire ground state hyperfine manifold, we get

$$\Delta E_{|F,m_F\rangle}^2 = (-1)^F \frac{g_s^2 \mu_B^2 B_Z^2}{4 \Delta E_{hfs}} (1 - m_F^2/4) \quad (\text{B.15})$$

Plugging in the numbers for ^{87}Rb , we get

$$\Delta E_{|F,m_F\rangle}^2 = h \times (-1)^F (1 - m_F^2/4) (287.6 \text{ Hz/G}^2) \times B [\text{G}]^2 \quad (\text{B.16})$$

We have derived a formula for the quadratic Zeeman shift and seen that it arises due to a mixing of states with the same m_F but different F quantum numbers. This can be thought of intuitively as follows: applying an external magnetic field creates an induced magnetic moment $\mu_i \approx \mu_B^2 B_z / \Delta E_{hfs}$ which interacts with the magnetic field and shifts the energy levels by an amount $\mu_i B_z$, analogous to the AC Stark Shift.

The full Hamiltonian can be diagonalized in cases (including this one) where either $J = 1/2$ or $I = 1/2$. The eigen-energies can be calculated analytically using the Breit-Rabi formula [128] (see [129] for an accessible derivation). The perturbation calculation gives a slightly more intuitive picture of the origin of the quadratic Zeeman shift.

Appendix C

Two component BEC

Consider a two component BEC, with the wavefunction

$$\psi = \begin{pmatrix} \psi_a \\ \psi_b \end{pmatrix} \quad (\text{C.1})$$

The dynamics of an interacting two-component spinor can be described by extending the GPE equation to multi-component wavefunctions:

$$i\hbar \frac{\partial \psi_a}{\partial t} = \left(-\frac{\hbar^2}{2m} \nabla^2 + V + g_a |\psi_a|^2 + g_{ab} |\psi_b|^2 \right) \psi_a \quad (\text{C.2})$$

$$i\hbar \frac{\partial \psi_b}{\partial t} = \left(-\frac{\hbar^2}{2m} \nabla^2 + V + g_b |\psi_b|^2 + g_{ab} |\psi_a|^2 \right) \psi_b \quad (\text{C.3})$$

The condensate is initially entirely in the state a . The ground state ψ_a^0 is given by

$$\left(-\frac{\hbar^2}{2m} \nabla^2 + V + g_a |\psi_a|^2 \right) \psi_a^0 = \mu \psi_a^0. \quad (\text{C.4})$$

The time dependent ground state wavefunction is

$$\psi_a^0(t) = \psi_a^0 \exp(-i\mu t/\hbar) \quad (\text{C.5})$$

Now consider a small rotation of the spin, such that there is now some population in state b :

$$\psi_a(t) = \psi_a^0(t) + \epsilon(t), \quad (\text{C.6})$$

$$\psi_b(t) = \delta(t). \quad (\text{C.7})$$

Here, $\delta, \epsilon \ll \psi_0^0$. Plugging Eqs. C.6 and C.7 in Eqs. C.2 and Eqs. C.3 and ignoring second order terms in δ and ϵ , we get

$$i\hbar \frac{\partial \epsilon(t)}{\partial t} = -\frac{\hbar^2}{2m} \nabla^2 \epsilon(t) + V \epsilon(t) + g_a (2 |\psi_a^0(t)|^2 \epsilon(t) + \psi_a^0(t)^2 \epsilon^*), \quad (\text{C.8})$$

$$i\hbar \frac{\partial \delta}{\partial t} = -\frac{\hbar^2}{2m} \nabla^2 \delta + V \delta + g_{ab} |\psi_a^0|^2 \delta. \quad (\text{C.9})$$

In the case when $g_{ab} \sim g_a$, and the Thomas-Fermi approximation is valid,

$$g_{ab} |\psi_a^0|^2 = g_a |\psi_a^0|^2 = (\mu - V) \mathcal{H}(\mu - V). \quad (\text{C.10})$$

Here, \mathcal{H} is the Heaviside function (step function). Eq. C.9 transforms to

$$i\hbar \frac{\partial \delta}{\partial t} = -\frac{\hbar^2}{2m} \nabla^2 \delta + V \mathcal{H}(V - \mu) \delta. \quad (\text{C.11})$$

Thus, in the bulk of the condensate, where $\mu > V$, Eq. C.11 looks like the free particle Schrödinger equation. The potential energy V is exactly cancelled by the interaction energy of the condensate in state a . The equation for ϵ (Eq. C.8) does not depend on δ and looks like the standard Bogoliubov equations.

Bibliography

- [1] Rockson Chang, Shreyas Potnis, Christopher W Ellenor, Mirco Siercke, Alex Hayat, and Aephraim M Steinberg. “[Observation of transient momentum-space interference during scattering of a condensate from an optical barrier](#)”. *Phys. Rev. A* 88.5 (Nov. 2013), p. 53634 (cit. on p. iv).
- [2] Rockson Chang, Shreyas Potnis, Ramon Ramos, Chao Zhuang, Matin Hallaji, Alex Hayat, Federico Duque-Gomez, J.E. Sipe, and Aephraim M Steinberg. “[Observing the Onset of Effective Mass](#)”. *Phys. Rev. Lett.* 112.17 (May 2014), p. 170404 (cit. on p. iv).
- [3] Alex Hayat et al. “[Enhanced coherence between condensates formed resonantly at different times](#).” *Optics express* 22.25 (Dec. 2014), pp. 30559–70 (cit. on p. iv).
- [4] M H Anderson, J R Ensher, M R Matthews, C E Wieman, and E A Cornell. “[Observation of bose-einstein condensation in a dilute atomic vapor](#).” *Science (New York, N.Y.)* 269.5221 (July 1995), pp. 198–201 (cit. on p. 1).
- [5] K. Davis, M. Mewes, M. Andrews, N. van Druten, D. Durfee, D. Kurn, and W. Ketterle. “[Bose-Einstein Condensation in a Gas of Sodium Atoms](#)”. *Physical Review Letters* 75.22 (Nov. 1995), pp. 3969–3973 (cit. on p. 1).
- [6] Maxime Ben Dahan, Ekkehard Peik, Jakob Reichel, Yvan Castin, and Christophe Salomon. “[Bloch Oscillations of Atoms in an Optical Potential](#)”. *Physical Review Letters* 76.24 (June 1996), pp. 4508–4511 (cit. on p. 1).
- [7] B. P. Anderson. “[Macroscopic Quantum Interference from Atomic Tunnel Arrays](#)”. *Science* 282.5394 (Nov. 1998), pp. 1686–1689 (cit. on pp. 1, 81).
- [8] Giacomo Roati, Chiara D’Errico, Leonardo Fallani, Marco Fattori, Chiara Fort, Matteo Zaccanti, Giovanni Modugno, Michele Modugno, and Massimo Inguscio. “[Anderson localization of a non-interacting Bose-Einstein condensate](#).” *Nature* 453.7197 (June 2008), pp. 895–8 (cit. on p. 1).
- [9] Immanuel Bloch and Wilhelm Zwerger. “[Many-body physics with ultracold gases](#)”. *Reviews of Modern Physics* 80.3 (July 2008), pp. 885–964 (cit. on pp. 1, 81).
- [10] Markus Greiner, Olaf Mandel, Tilman Esslinger, Theodor W. Hänsch, and Immanuel Bloch. “[Quantum phase transition from a superfluid to a Mott insulator in a gas of ultracold atoms](#)”. *Nature* 415.6867 (Jan. 2002), pp. 39–44 (cit. on pp. 1, 81).

- [11] Robert Jördens, Niels Strohmaier, Kenneth Günter, Henning Moritz, and Tilman Esslinger. “A Mott insulator of fermionic atoms in an optical lattice.” *Nature* 455.7210 (Sept. 2008), pp. 204–7 (cit. on pp. 1, 81).
- [12] M. Greiner, C. A. Regal, and D. S. Jin. “Probing the Excitation Spectrum of a Fermi Gas in the BCS-BEC Crossover Regime”. *Physical Review Letters* 94.7 (Feb. 2005), p. 070403 (cit. on p. 1).
- [13] Mingwu Lu, Nathaniel Q. Burdick, Seo Ho Youn, and Benjamin L. Lev. “Strongly Dipolar Bose-Einstein Condensate of Dysprosium”. *Physical Review Letters* 107.19 (Oct. 2011), p. 190401 (cit. on p. 1).
- [14] K-K Ni, S Ospelkaus, M H G de Miranda, A Pe’er, B Neyenhuis, J J Zirbel, S Kotochigova, P S Julienne, D S Jin, and J Ye. “A high phase-space-density gas of polar molecules.” *Science (New York, N.Y.)* 322.5899 (Oct. 2008), pp. 231–5 (cit. on p. 1).
- [15] Holger Kadau, Matthias Schmitt, Matthias Wenzel, Clarissa Wink, Thomas Maier, Igor Ferrier-Barbut, and Tilman Pfau. “Observing the Rosensweig instability of a quantum ferrofluid” (Aug. 2015). arXiv: [1508.05007](https://arxiv.org/abs/1508.05007) (cit. on p. 1).
- [16] Y.-J. Lin, K. Jiménez-García, and I. B. Spielman. “Spin-orbit-coupled Bose-Einstein condensates”. *Nature* 471.7336 (Mar. 2011), pp. 83–86 (cit. on p. 1).
- [17] Y.J. Lin, R. L. Compton, K. Jiménez-García, W. D. Phillips, J. V. Porto, and I. B. Spielman. “A synthetic electric force acting on neutral atoms”. *Nature Physics* 7.7 (Mar. 2011), pp. 531–534 (cit. on p. 1).
- [18] Richard P. Feynman. “Simulating physics with computers”. *International Journal of Theoretical Physics* 21.6-7 (June 1982), pp. 467–488 (cit. on p. 1).
- [19] K Henderson, C Ryu, C MacCormick, and M G Boshier. “Experimental demonstration of painting arbitrary and dynamic potentials for Bose-Einstein condensates”. en. *New Journal of Physics* 11.4 (Apr. 2009), p. 043030 (cit. on p. 2).
- [20] E H Hauge and J A St\ovneng. “Tunneling times: a critical review”. *Rev. Mod. Phys.* 61.4 (Oct. 1989), pp. 917–936 (cit. on pp. 2, 52).
- [21] Aephraim M Steinberg. “Conditional probabilities in quantum theory and the tunneling-time controversy”. *Phys. Rev. A* 52.1 (July 1995), pp. 32–42 (cit. on pp. 2, 55).
- [22] Franco Dalfovo, Stefano Giorgini, Lev P. Pitaevskii, and Sandro Stringari. “Theory of Bose-Einstein condensation in trapped gases”. *Reviews of Modern Physics* 71.3 (Apr. 1999), pp. 463–512 (cit. on p. 4).
- [23] C. J. Pethick and Smith J. *Bose-Einstein Condensation in Dilute Gases*. Cambridge University Press (cit. on p. 4).
- [24] Gordon Baym and C. J. Pethick. “Ground-State Properties of Magnetically Trapped Bose-Condensed Rubidium Gas”. *Physical Review Letters* 76.1 (Jan. 1996), pp. 6–9 (cit. on pp. 5, 86, 92).

- [25] Y Castin and R Dum. “[Bose-Einstein Condensates in Time Dependent Traps](#)”. *Phys. Rev. Lett.* 77.27 (Dec. 1996), pp. 5315–5319 (cit. on pp. [5](#), [6](#), [49](#), [66](#), [88](#)).
- [26] Ana Jofre. “The Design and Construction of a Bose-Einstein Condensation Apparatus”. PhD thesis. Department of Physics, University of Toronto, 2003 (cit. on pp. [7](#), [9](#)).
- [27] Mirco Siercke. “Realization of Bose-Einstein Condensation of ^{87}Rb in a Time-Orbiting Potential trap”. PhD thesis. Department of Physics, University of Toronto, 2010 (cit. on pp. [7](#), [14](#)).
- [28] Chris Ellenor. “Bose-Einstein Condensate Wavefunction Reconstruction Through Collisions with Optical Potentials”. PhD thesis. Department of Physics, University of Toronto, 2011 (cit. on pp. [7](#), [9](#), [10](#), [12](#), [18](#), [20](#)).
- [29] Rockson Chang. “Exploring matter-wave dynamics with a Bose-Einstein condensate”. PhD thesis. Department of Physics, University of Toronto, 2012 (cit. on pp. [7](#), [9–12](#), [18](#), [20](#), [21](#), [27](#), [29](#), [61](#)).
- [30] Wolfgang Ketterle and N J Van Druten. “[Evaporative Cooling of Trapped Atoms](#)”. Advances In Atomic, Molecular, and Optical Physics 37 (1996). Ed. by Benjamin Bederson and Herbert Walther, pp. 181–236 (cit. on p. [8](#)).
- [31] C P Pearman, C S Adams, S G Cox, P F Griffin, D A Smith, and I G Hughes. “[Polarization spectroscopy of a closed atomic transition: applications to laser frequency locking](#)”. *Journal of Physics B: Atomic, Molecular and Optical Physics* 35.24 (Dec. 2002), pp. 5141–5151 (cit. on pp. [14](#), [17](#)).
- [32] E. A. Donley, T. P. Heavner, F. Levi, M. O. Tataw, and S. R. Jefferts. “[Double-pass acousto-optic modulator system](#)”. *Review of Scientific Instruments* 76.6 (June 2005), p. 063112 (cit. on p. [16](#)).
- [33] Daniel A Steck. “Rubidium 87 D Line Data”. revision 2 () (cit. on pp. [18](#), [112](#)).
- [34] G. Reinaudi, T. Lahaye, Z. Wang, and D. Guéry-Odelin. “[Strong saturation absorption imaging of dense clouds of ultracold atoms](#)”. *EN. Optics Letters* 32.21 (Nov. 2007), p. 3143 (cit. on pp. [25](#), [97](#)).
- [35] Mikhail Egorov. “Coherence and collective oscillations of a two-component Bose-Einstein condensate”. PhD thesis. Centre for Atom Optics and Ultrafast Spectroscopy Swinburne University of Technology, Melbourne, Australia., 2012 (cit. on pp. [25](#), [97](#)).
- [36] Michael Erhard. “Experimente mit mehrkomponentigen Bose-Einstein-Kondensaten”. PhD thesis. 2004 (cit. on p. [27](#)).
- [37] Jochen Kronjäger. “Coherent Dynamics of Spinor Bose-Einstein Condensates”. PhD thesis. 2007 (cit. on p. [27](#)).
- [38] Xiaolin Li, Min Ke, Bo Yan, and Yuzhu Wang. “Reduction of interference fringes in absorption imaging of cold atom cloud using eigenface method”. *Chinese Optics Letters* 05.03 (), p. 128 (cit. on p. [27](#)).

- [39] C. F. Ockeloen, A. F. Tauschinsky, R. J. C. Spreeuw, and S. Whitlock. “[Detection of small atom numbers through image processing](#)”. *Physical Review A* 82.6 (Dec. 2010), p. 061606 (cit. on p. 27).
- [40] Waseem S Bakr, Jonathon I Gillen, Amy Peng, Simon Fölling, and Markus Greiner. “[A quantum gas microscope for detecting single atoms in a Hubbard-regime optical lattice.](#)” en. *Nature* 462.7269 (Nov. 2009), pp. 74–7 (cit. on p. 30).
- [41] D. M. Stamper-Kurn, H.-J. Miesner, A. P. Chikkatur, S. Inouye, J. Stenger, and W. Ketterle. “[Reversible Formation of a Bose-Einstein Condensate](#)”. *Physical Review Letters* 81.11 (Sept. 1998), pp. 2194–2197 (cit. on pp. 32, 96).
- [42] Wolfgang Alt. “[An objective lens for efficient fluorescence detection of single atoms](#)”. *Optik - International Journal for Light and Electron Optics* 113.3 (2002), pp. 142–144 (cit. on p. 35).
- [43] L. J. LeBlanc and J. H. Thywissen. “[Species-specific optical lattices](#)”. *Physical Review A* 75.5 (May 2007), p. 053612 (cit. on pp. 39, 75).
- [44] Bindya Arora, M. S. Safronova, and Charles W. Clark. “[Tune-out wavelengths of alkali-metal atoms and their applications](#)”. *Physical Review A* 84.4 (Oct. 2011), p. 043401 (cit. on pp. 39, 61, 75).
- [45] R. H. Leonard, A. J. Fallon, C. A. Sackett, and M. S. Safronova. “[High precision measurement of the 87Rb D-line tune-out wavelength](#)” (July 2015), p. 7. arXiv: [1507 . 07898](https://arxiv.org/abs/1507.07898) (cit. on pp. 39, 75).
- [46] K. C. Wright, L. S. Leslie, and N. P. Bigelow. “[Raman coupling of Zeeman sublevels in an alkali-metal Bose-Einstein condensate](#)”. *Physical Review A* 78.5 (Nov. 2008), p. 053412 (cit. on pp. 40, 77).
- [47] W. Rohringer, R. Bücker, S. Manz, T. Betz, Ch. Koller, M. Göbel, A. Perrin, J. Schmiedmayer, and T. Schumm. “[Stochastic optimization of a cold atom experiment using a genetic algorithm](#)”. *Applied Physics Letters* 93.26 (Dec. 2008), p. 264101 (cit. on p. 43).
- [48] Aviv Keshet and Wolfgang Ketterle. “[A distributed, graphical user interface based, computer control system for atomic physics experiments.](#)” *The Review of scientific instruments* 84.1 (Jan. 2013), p. 015105 (cit. on p. 45).
- [49] Peter E Gaskell, Jeremy J Thorn, Sequoia Alba, and Daniel A Steck. “[An open-source, extensible system for laboratory timing and control.](#)” *The Review of scientific instruments* 80.11 (Nov. 2009), p. 115103 (cit. on p. 45).
- [50] G L Gattobigio, T Pohl, G Labeyrie, and R Kaiser. “[Scaling laws for large magneto-optical traps](#)”. en. *Physica Scripta* 81.2 (Feb. 2010), p. 025301 (cit. on p. 46).
- [51] Wolfgang Ketterle and N. J. van Druten. “[Bose-Einstein condensation of a finite number of particles trapped in one or three dimensions](#)”. *Physical Review A* 54.1 (July 1996), pp. 656–660 (cit. on p. 48).

- [52] J. Söding, D. Guéry-Odelin, P. Desbiolles, F. Chevy, H. Inamori, and J. Dalibard. “Three-body decay of a rubidium Bose–Einstein condensate”. *Applied Physics B* 69.4 (Feb. 2014), pp. 257–261 (cit. on pp. 48, 99).
- [53] J Szczepkowski, R Gartman, M Witkowski, L Tracewski, M Zawada, and W Gawlik. “Analysis and calibration of absorptive images of Bose-Einstein condensate at nonzero temperatures.” *The Review of scientific instruments* 80.5 (May 2009), p. 053103 (cit. on p. 49).
- [54] S. Giorgini, L. P. Pitaevskii, and S. Stringari. “Condensate fraction and critical temperature of a trapped interacting Bose gas”. *Physical Review A* 54.6 (Dec. 1996), R4633–R4636 (cit. on p. 49).
- [55] M. Naraschewski and D. M. Stamper-Kurn. “Analytical description of a trapped semi-ideal Bose gas at finite temperature”. *Physical Review A* 58.3 (Sept. 1998), pp. 2423–2426 (cit. on p. 49).
- [56] Aephraim M Steinberg. “How Much Time Does a Tunneling Particle Spend in the Barrier Region?” *Phys. Rev. Lett.* 74.13 (Mar. 1995), pp. 2405–2409 (cit. on pp. 52, 54, 55).
- [57] R Landauer and Th. Martin. “Barrier interaction time in tunneling”. *Rev. Mod. Phys.* 66.1 (Jan. 1994), pp. 217–228 (cit. on pp. 52, 53).
- [58] Raymond Y. Chiao. “Tunneling times and superluminality: a tutorial”. *Mysteries, puzzles, and paradoxes in quantum mechanics*. Vol. 461. ASCE, 1999, pp. 3–13 (cit. on p. 52).
- [59] Eugene P Wigner. “Lower Limit for the Energy Derivative of the Scattering Phase Shift”. *Physical Review* 98.1 (Apr. 1955), pp. 145–147 (cit. on p. 52).
- [60] Thomas E. Hartman. “Tunneling of a Wave Packet”. *Journal of Applied Physics* 33.12 (June 1962), p. 3427 (cit. on p. 52).
- [61] A. M. Steinberg, P. G. Kwiat, and R. Y. Chiao. “Measurement of the single-photon tunneling time”. *Physical Review Letters* 71.5 (Aug. 1993), pp. 708–711 (cit. on p. 53).
- [62] Ch. Spielmann, R. Szipöcs, A. Stingl, and F. Krausz. “Tunneling of Optical Pulses through Photonic Band Gaps”. *Physical Review Letters* 73.17 (Oct. 1994), pp. 2308–2311 (cit. on p. 53).
- [63] D. Mugnai, A. Ranfagni, and L. S. Schulman. “Delay time measurements in a diffraction experiment: A case of optical tunneling”. *Physical Review E* 55.3 (Mar. 1997), pp. 3593–3597 (cit. on p. 53).
- [64] P Eckle, A N Pfeiffer, C Cirelli, A Staudte, R Dörner, H G Muller, M Büttiker, and U Keller. “Attosecond ionization and tunneling delay time measurements in helium.” *Science (New York, N.Y.)* 322.5907 (Dec. 2008), pp. 1525–9 (cit. on p. 53).
- [65] Lisa Torlina et al. “Interpreting attoclock measurements of tunnelling times”. *Nature Physics* 11.6 (May 2015), pp. 503–508 (cit. on p. 53).

- [66] M. Büttiker and R. Landauer. “Traversing Time for Tunneling”. *Physical Review Letters* 49.23 (Dec. 1982), pp. 1739–1742 (cit. on p. 53).
- [67] M Büttiker. “Larmor precession and the traversal time for tunneling”. *Phys. Rev. B* 27.10 (May 1983), pp. 6178–6188 (cit. on p. 53).
- [68] A. I Baz'. *Sov. J. Nucl. Phys.* 4 (1967), p. 182 (cit. on p. 53).
- [69] V. F Rybachenko. *Sov. J. Nucl. Phys.* 5 (1967), p. 635 (cit. on p. 53).
- [70] Felix T. Smith. “Lifetime Matrix in Collision Theory”. *Physical Review* 118.1 (Apr. 1960), pp. 349–356 (cit. on p. 54).
- [71] Yakir Aharonov, Noam Erez, and Benni Reznik. “Superoscillations and tunneling times”. *Physical Review A* 65.5 (May 2002), p. 052124 (cit. on p. 54).
- [72] Yakir Aharonov and Lev Vaidman. “Properties of a quantum system during the time interval between two measurements”. *Physical Review A* 41.1 (Jan. 1990), pp. 11–20 (cit. on p. 55).
- [73] A.M. Steinberg. “Time and history in quantum tunneling”. *Superlattices and Microstructures* 23.3-4 (Mar. 1998), pp. 823–832 (cit. on p. 56).
- [74] A. M. Steinberg, S. Myrskog, Han Seb Moon, Hyun Ah Kim, Jalani Fox, and Jung Bog Kim. “The non-paradox of superluminal tunneling, and a planned experiment to study the real mystery”. *Mysteries, puzzles, and paradoxes in quantum mechanics*. Vol. 461. 1. ASCE, Mar. 1999, pp. 36–46 (cit. on p. 56).
- [75] R. Shankar. *Principles of Quantum Mechanics*. Springer (cit. on p. 58).
- [76] Ying Wu. “Effective Raman theory for a three-level atom in the Λ configuration”. *Physical Review A* 54.2 (Aug. 1996), pp. 1586–1592 (cit. on p. 63).
- [77] Hubert Ammann and Nelson Christensen. “Delta Kick Cooling: A New Method for Cooling Atoms”. *Phys. Rev. Lett.* 78.11 (Mar. 1997), pp. 2088–2091 (cit. on p. 64).
- [78] S H Myrskog, J K Fox, H S Moon, J B Kim, and A M Steinberg. “Modified “ $\delta\{\}$ -kick cooling” using magnetic field gradients”. *Phys. Rev. A* 61.5 (Apr. 2000), p. 53412 (cit. on p. 64).
- [79] E. Maréchal, S. Guibal, J.-L. Bossennec, R. Barbé, J.-C. Keller, and O. Gorceix. “Longitudinal focusing of an atomic cloud using pulsed magnetic forces”. *Physical Review A* 59.6 (June 1999), pp. 4636–4640 (cit. on p. 64).
- [80] F Jendrzejewski, K Müller, J Richard, A Date, T Plisson, P Bouyer, A Aspect, and V Josse. “Coherent Backscattering of Ultracold Atoms”. *Phys. Rev. Lett.* 109.19 (Nov. 2012), p. 195302 (cit. on p. 64).
- [81] G D McDonald, C C N Kuhn, S Bennetts, J E Debs, K S Hardman, M Johnsson, J D Close, and N P Robins. “ $80\hbar k$ momentum separation with Bloch oscillations in an optically guided atom interferometer”. *Phys. Rev. A* 88.5 (Nov. 2013), p. 53620 (cit. on p. 64).
- [82] H. Müntinga et al. “Interferometry with Bose-Einstein Condensates in Microgravity”. *Physical Review Letters* 110.9 (Feb. 2013), p. 093602 (cit. on p. 64).

- [83] Tim Kovachy, Jason M. Hogan, Alex Sugarbaker, Susannah M. Dickerson, Christine A. Donnelly, Chris Overstreet, and Mark A. Kasevich. “[Matter Wave Lensing to Picokelvin Temperatures](#)”. *Physical Review Letters* 114.14 (Apr. 2015), p. 143004 (cit. on pp. 64, 67).
- [84] Pascal Böhi, Max F. Riedel, Johannes Hoffrogge, Jakob Reichel, Theodor W. Hänsch, and Philipp Treutlein. “[Coherent manipulation of Bose–Einstein condensates with state-dependent microwave potentials on an atom chip](#)”. *Nature Physics* 5.8 (July 2009), pp. 592–597 (cit. on p. 68).
- [85] A Smith, B E Anderson, S Chaudhury, and P S Jessen. “[Three-axis measurement and cancellation of background magnetic fields to less than 50 μG in a cold atom experiment](#)”. en. *Journal of Physics B: Atomic, Molecular and Optical Physics* 44.20 (Oct. 2011), p. 205002 (cit. on p. 68).
- [86] M. R. Matthews, B. P. Anderson, P. C. Haljan, D. S. Hall, C. E. Wieman, and E. A. Cornell. “[Vortices in a Bose-Einstein Condensate](#)”. *Physical Review Letters* 83.13 (Sept. 1999), pp. 2498–2501 (cit. on p. 80).
- [87] K. W. Madison, F. Chevy, W. Wohlleben, and J. Dalibard. “[Vortex Formation in a Stirred Bose-Einstein Condensate](#)”. *Physical Review Letters* 84.5 (Jan. 2000), pp. 806–809 (cit. on p. 80).
- [88] J. R. Abo-Shaeer, C. Raman, J. M. Vogels, and W. Ketterle. “[Observation of Vortex Lattices in Bose-Einstein Condensates](#)”. *Science* 292.5516 (Apr. 2001), pp. 476–479 (cit. on p. 80).
- [89] M. R. Andrews. “[Observation of Interference Between Two Bose Condensates](#)”. *Science* 275.5300 (Jan. 1997), pp. 637–641 (cit. on p. 80).
- [90] Tilman Esslinger, Immanuel Bloch, and Theodor W. Hänsch. “[Probing first-order spatial coherence of a Bose-Einstein condensate](#)”. en. *Journal of Modern Optics* (July 2009) (cit. on p. 80).
- [91] S S Hodgman, R G Dall, A G Manning, K G H Baldwin, and A G Truscott. “[Direct measurement of long-range third-order coherence in Bose-Einstein condensates.](#)” *Science (New York, N.Y.)* 331.6020 (Feb. 2011), pp. 1046–9 (cit. on p. 80).
- [92] R. W. Gurney and E. U. Condon. “[Quantum Mechanics and Radioactive Disintegration](#)”. *Physical Review* 33.2 (Feb. 1929), pp. 127–140 (cit. on p. 80).
- [93] Anthony J. Leggett. “[Macroscopic Quantum Systems and the Quantum Theory of Measurement](#)”. *Progress of Theoretical Physics Supplement* 69 (1980), pp. 80–100 (cit. on p. 81).
- [94] Michael Albiez, Rudolf Gati, Jonas Fölling, Stefan Hunsmann, Matteo Cristiani, and Markus K Oberthaler. “[Direct Observation of Tunneling and Nonlinear Self-Trapping in a Single Bosonic Josephson Junction](#)”. *Phys. Rev. Lett.* 95.1 (June 2005), p. 10402 (cit. on p. 81).
- [95] S Levy, E Lahoud, I Shomroni, and J Steinhauer. “[The a.c. and d.c. Josephson effects in a Bose-Einstein condensate.](#)” *Nature* 449.7162 (Oct. 2007), pp. 579–83 (cit. on p. 81).

- [96] L. J. LeBlanc, A. B. Bardon, J. McKeever, M. H. T. Extavour, D. Jervis, J. H. Thywissen, F. Piazza, and A. Smerzi. “[Dynamics of a Tunable Superfluid Junction](#)”. *Physical Review Letters* 106.2 (Jan. 2011), p. 025302 (cit. on p. 81).
- [97] O. Morsch, J. H. Müller, M. Cristiani, D. Ciampini, and E. Arimondo. “[Bloch Oscillations and Mean-Field Effects of Bose-Einstein Condensates in 1D Optical Lattices](#)”. *Physical Review Letters* 87.14 (Sept. 2001), p. 140402 (cit. on p. 81).
- [98] M Cristiani, O Morsch, J H Müller, D Ciampini, and E Arimondo. “[Experimental properties of Bose-Einstein condensates in one-dimensional optical lattices: Bloch oscillations, Landau-Zener tunneling, and mean-field effects](#)”. *Phys. Rev. A* 65.6 (June 2002), p. 63612 (cit. on p. 81).
- [99] L D Carr, M J Holland, and B A Malomed. “[Macroscopic quantum tunnelling of Bose–Einstein condensates in a finite potential well](#)”. *Journal of Physics B: Atomic, Molecular and Optical Physics* 38.17 (2005), p. 3217 (cit. on p. 81).
- [100] G. Dekel, V. Fleurov, A. Soffer, and C. Stucchio. “[Temporal dynamics of tunneling: Hydrodynamic approach](#)”. *Physical Review A* 75.4 (Apr. 2007), p. 043617 (cit. on p. 81).
- [101] G. Dekel, V. Farberovich, V. Fleurov, and A. Soffer. “[Dynamics of macroscopic tunneling in elongated Bose-Einstein condensates](#)”. *Physical Review A* 81.6 (June 2010), p. 063638 (cit. on p. 81).
- [102] L Salasnich, A Parola, and L Reatto. “[Pulsed macroscopic quantum tunneling of falling Bose-Einstein condensates](#)”. *Phys. Rev. A* 64.2 (June 2001), p. 23601 (cit. on p. 81).
- [103] A. del Campo, F. Delgado, G. García-Calderón, J. G. Muga, and M. G. Raizen. “[Decay by tunneling of bosonic and fermionic Tonks-Girardeau gases](#)”. *Physical Review A* 74.1 (July 2006), p. 013605 (cit. on p. 81).
- [104] Axel U J Lode, Alexej I Streltsov, Kaspar Sakmann, Ofir E Alon, and Lorenz S Cederbaum. “[How an interacting many-body system tunnels through a potential barrier to open space.](#)” *Proceedings of the National Academy of Sciences of the United States of America* 109.34 (Aug. 2012), pp. 13521–5 (cit. on p. 81).
- [105] Rudolf Grimm, Matthias Weidemüller, and Yurii B Ovchinnikov. “[Optical dipole traps for neutral atoms](#)”. *Advances in atomic, molecular, and optical physics* 42 (2000), pp. 95–170 (cit. on pp. 82, 98).
- [106] Nir Friedman, Ariel Kaplan, and Nir Davidson. “[Dark optical traps for cold atoms](#)”. *Advances in Atomic Molecular and Optical Physics* 48 (2002), pp. 99–152 (cit. on p. 82).
- [107] A Hemmerich, M Weidemüller, T Esslinger, C Zimmermann, and T Hänsch. “[Trapping atoms in a dark optical lattice](#)”. *Physical review letters* 75.1 (1995), p. 37 (cit. on p. 82).
- [108] BP Anderson, TL Gustavson, and MA Kasevich. “[Atom trapping in nondissipative optical lattices](#)”. *Physical Review A* 53.6 (1996), R3727 (cit. on p. 82).

- [109] T. P. Meyrath, F. Schreck, J. L. Hanssen, C. -S. Chuu, and M. G. Raizen. “A high frequency optical trap for atoms using Hermite-Gaussian beams”. EN. *Optics Express* 13.8 (Apr. 2005), p. 2843 (cit. on p. 82).
- [110] C.-S. Chuu, F Schreck, T P Meyrath, J L Hanssen, G N Price, and M G Raizen. “Direct Observation of Sub-Poissonian Number Statistics in a Degenerate Bose Gas”. *Phys. Rev. Lett.* 95.26 (Dec. 2005), p. 260403 (cit. on p. 82).
- [111] Alexander L. Gaunt, Tobias F. Schmidutz, Igor Gotlibovych, Robert P. Smith, and Zoran Hadzibabic. “Bose-Einstein Condensation of Atoms in a Uniform Potential”. *Physical Review Letters* 110.20 (May 2013), p. 200406 (cit. on p. 82).
- [112] Yu. B. Ovchinnikov, I. Manek, and R. Grimm. “Surface Trap for Cs atoms based on Evanescent-Wave Cooling”. *Physical Review Letters* 79.12 (Sept. 1997), pp. 2225–2228 (cit. on p. 82).
- [113] Emil Lundh, C. J. Pethick, and H. Smith. “Zero-temperature properties of a trapped Bose-condensed gas: Beyond the Thomas-Fermi approximation”. *Physical Review A* 55.3 (Mar. 1997), pp. 2126–2131 (cit. on pp. 85, 92).
- [114] Yu. Kagan, E. L. Surkov, and G. V. Shlyapnikov. “Evolution of a Bose-condensed gas under variations of the confining potential”. *Physical Review A* 54.3 (Sept. 1996), R1753–R1756 (cit. on p. 88).
- [115] D. M. Stamper-Kurn, M. R. Andrews, A. P. Chikkatur, S. Inouye, H.-J. Miesner, J. Stenger, and W. Ketterle. “Optical Confinement of a Bose-Einstein Condensate”. *Physical Review Letters* 80.10 (Mar. 1998), pp. 2027–2030 (cit. on p. 88).
- [116] Kunal K. Das. “Highly anisotropic Bose-Einstein condensates: Crossover to lower dimensionality”. *Physical Review A* 66.5 (Nov. 2002), p. 053612 (cit. on p. 92).
- [117] A. Muñoz Mateo and V. Delgado. “Extension of the Thomas-Fermi approximation for trapped Bose-Einstein condensates with an arbitrary number of atoms”. *Physical Review A* 74.6 (Dec. 2006), p. 065602 (cit. on p. 92).
- [118] A. Muñoz Mateo and V. Delgado. “Ground-state properties of trapped Bose-Einstein condensates: Extension of the Thomas-Fermi approximation”. *Physical Review A* 75.6 (June 2007), p. 063610 (cit. on p. 92).
- [119] D. Malacara. *Optical Shop Testing, 3rd Edition*. Wiley (cit. on p. 95).
- [120] Nancy Makri and William H. Miller. “A semiclassical tunneling model for use in classical trajectory simulations”. *The Journal of Chemical Physics* 91.7 (Oct. 1989), p. 4026 (cit. on p. 95).
- [121] Y.-J. Lin, A R Perry, R L Compton, I B Spielman, and J V Porto. “Rapid production of ${}^87\text{Rb}$ Bose-Einstein condensates in a combined magnetic and optical potential”. *Phys. Rev. A* 79.6 (June 2009), p. 63631 (cit. on p. 96).

- [122] Peter A. Gorry. “General least-squares smoothing and differentiation by the convolution (Savitzky-Golay) method”. *Analytical Chemistry* 62.6 (Mar. 1990), pp. 570–573 (cit. on p. 101).
- [123] Weizhu Bao, Dieter Jaksch, and Peter A Markowich. “Numerical solution of the Gross-Pitaevskii equation for Bose-Einstein condensation”. *Journal of Computational Physics* 187.1 (2003), pp. 318–342 (cit. on p. 104).
- [124] Chris Loken et al. “SciNet: Lessons Learned from Building a Power-efficient Top-20 System and Data Centre”. en. *Journal of Physics: Conference Series* 256.1 (Nov. 2010), p. 012026 (cit. on p. 104).
- [125] S. Richard, F. Gerbier, J. H. Thywissen, M. Hugbart, P. Bouyer, and A. Aspect. “Momentum Spectroscopy of 1D Phase Fluctuations in Bose-Einstein Condensates”. *Physical Review Letters* 91.1 (July 2003), p. 010405 (cit. on p. 105).
- [126] Sabine Stock, Zoran Hadzibabic, Baptiste Battelier, Marc Cheneau, and Jean Dalibard. “Observation of Phase Defects in Quasi-Two-Dimensional Bose-Einstein Condensates”. *Physical Review Letters* 95.19 (Nov. 2005), p. 190403 (cit. on p. 105).
- [127] Run-Bing Li, Lin Zhou, Jin Wang, and Ming-Sheng Zhan. “Measurement of the quadratic Zeeman shift of 85Rb hyperfine sublevels using stimulated Raman transitions”. *Optics Communications* 282.7 (Apr. 2009), pp. 1340–1344 (cit. on p. 112).
- [128] G. Breit and I. I. Rabi. “Measurement of Nuclear Spin”. *Physical Review* 38.11 (Dec. 1931), pp. 2082–2083 (cit. on p. 114).
- [129] Daniel A Steck. “Quantum and Atom Optics”. revision 0.8.3, 25 May 2012 () (cit. on p. 114).